Development of the "Stix" Code, a Radio Frequency (RF) Wave Solver, to Investigate RF-Sheath Behavior in Realistic Tokamak Geometry

by

Christina P. Migliore

B.S. Physics and Mathematics, Northeastern University, 2018

Submitted to the Department of Nuclear Science and Engineering
in partial fulfillment of the requirements for the degree of

DOCTOR OF PHILOSOPHY IN NUCLEAR SCIENCE AND ENGINEERING

at the

MASSACHUSETTS INSTITUTE OF TECHNOLOGY

May 2024

Authored by:	Christina P. Migliore Department of Nuclear Science and Engineering March 20, 2024
Certified by:	John C. Wright Principle Research Scientist, Thesis Supervisor
Certified by:	Paul T. Bonoli Senior Research Scientist, Thesis Supervisor
Accepted by:	Ju Li Battelle Energy Alliance Professor of Nuclear Science and Engineering Chairman, Department Committee on Graduate Theses

Development of the "Stix" Code, a Radio Frequency (RF) Wave Solver, to Investigate RF-Sheath Behavior in Realistic Tokamak Geometry

by

Christina P. Migliore

Submitted to the Department of Nuclear Science and Engineering
on March 20, 2024 in partial fulfillment of the requirements for the degree of

DOCTOR OF PHILOSOPHY IN NUCLEAR SCIENCE AND ENGINEERING

ABSTRACT

A favorable method to heat plasmas to fusion relevant temperatures is to use radio frequency (RF) waves in the ion cyclotron range of frequencies (ICRF). However, experiments have shown that this technique produces RF rectified sheaths known to form on both the ICRF antenna as near-field sheaths and farther away from the antenna in the torus as far-field sheaths. These RF sheaths can result in large DC voltages on plasma facing components (PCFs) causing adverse effects such as impurity generation from sputtering of high-Z metallic coatings, edge power dissipation, and hot-spot formation. With many current and upcoming tokamaks relying on ICRF for heating, it is becoming increasingly critical to numerically model RF sheaths for advancing mitigation methods. Due to the size of the RF sheath in comparison to the launched RF wavelength, the RF sheath can be reduced to a boundary condition (BC) on the computational domain boundaries. Traditionally, many electromagnetic (EM) RF solvers use conducting wall BCs that do not include the effects of sheaths while other codes use overly simplified models that do not capture accurate rectification. Recently, J. Myra et. al 2015 models the RF sheath as a non-linear BC using a characteristic sheath impedance allowing for a more representative calculation of DC enhanced potentials on PFCs.

In this thesis, the novel finite-element plasma RF wave solver called "Stix" that includes the full non-linear RF sheath BC is introduced with the goal of investigating RF sheath behavior in realistic tokamak geometry. First, it is demonstrated that Stix can replicate previous analytical and numerical RF sheath cases as verification of the solve. Next, focusing on near-field sheaths, the experimental antenna power phasing study done on Alcator C-Mod is chosen to be simulated with Stix. Using a magnetic field aligned two-dimensional (2D) slice along the 4 straps of the C-Mod ICRF antenna, it is seen that Stix can reproduce the experimental minimization trend in the enhanced potentials found when varying the strength of the power ratio between the 2 inner straps versus the total 4 straps. Similarly, Stix confirms that the monopole phasing of the 4 straps produces significantly higher potentials as found in experiment. For the various antenna phasing schemes, an estimate of erosion rate from the DC voltages shows that even in the lowest voltages cases the sputtering is notable. To examine the behavior of far-field sheaths, a predictive study is chosen for the upcoming SPARC tokamak. Using a 2D simulation in the poloidal cross-section of SPARC, the effect of

varying the strength of wave-particle absorption on the enhanced potentials is investigated. It is found that even with the lowest absorption scenario, the calculated voltages along the vacuum vessel are negligible. This result is discovered to be due to the small magnetic field angles, b_n, into the walls as direct consequence of the poloidal cross-section reference frame. Further investigation through the addition of limiter-like bumps shows that far-field rectification is dominated by the strength of b_n. The findings from both the comparison and predictive modeling of RF sheaths done in Stix show the effectiveness such a numerical tool has for furthering the optimization of ICRF heating.

Thesis supervisor: John C. Wright
Title: Principle Research Scientist

Thesis supervisor: Paul T. Bonoli
Title: Senior Research Scientist

Acknowledgments

There are so many pivotal people without whose support I would not be here today. I would first like to thank my advisors: Dr. John Wright and Dr. Paul Bonoli. Over the course of this thesis, they have provided me with invaluable mentorship, feedback, and expertise of wave physics. I am extremely grateful to have such supportive advisors. I would also like to thank Mark Stowell at Lawrence Livermore National Laboratory for all the various MFEM code development help and finite-element mastery without whom the Stix code could not be possible.

I would also like to thank Dr. Dennis Whyte for providing critical feedback and guidance on this thesis as well as serving as the thesis reader. I am extremely appreciative of Professor Ian Hutchinson and Professor Anne White for their critical help, knowledge, and discussions at the beginning stages of the thesis. I would additionally like to thank Professor Jack Hare and Professor Nuno Loureiro for serving as my thesis defense committee.

I am deeply grateful for the RF-SciDac collaboration, especially the RF-SciDac weekly meetings that provided a crucial role in the progress of the RF sheath edge interaction within Stix. I would like to thank in particular Dr. Jim Myra, Dr. Syun'ichi Shiraiwai, Dr. Nicola Bertelli, Dr. Tom Jenkins, Dr. David Smithe, Professor Davide Curreli, Andrea Gonzalez Golvan, Dr. Atul Kumar, Dr. Rhea Barnett, and Dr. Matt Poulos for all the collaborative discussions through the years. I would additionally like to thank Dr. Greg Wallace and Dr. Steve Wukitch for their limitless knowledge of wave physics that helped strengthen my investigations.

I would like to thank the whole PSFC community and in particular the graduate students, past and current, whose friendship and comradely has made my time as a graduate student special. I would like to thank Dr. Rachel Bielajew, Evan Leppink, Richard Ibekwe, Dr. Sam Frank, Dr. Pablo Rodriguez-Fernandez, Dr. Will McCarthy, Conor Perks, Raymond Diab, Christian Yoo, Dr. Muni Zhou, Dr. Lucio Milanese, Dr. Abhi Mathews, Dr. Sean Ballinger, Dr. Thanh Nguyen, Dr. Bodhi Biswas and Dr. Alex Tingley.

I am extremely grateful for my support system outside of MIT, my family: Paul, Irina, Timothy, Jasmine, Karin, Mary-Jane, Jess, and Michael, whose unlimited support has helped me in the hardest of times. Last but certainly not least, I would like to thank my husband Brian (and our dog Archie) for the endless encouragement and cheering on over the entirety of my PhD. I am greatly appreciative to Brian for absolutely everything but I must give him a special shout out for always happily listening to my practice presentations, regardless of how many times he has heard that same talk.

Copyright Acknowledgement

The following thesis uses content from two peer-reviewed papers authored by the author of this thesis:

†C. Migliore, M. Stowell, J. Wright, P. Bonoli; Development of impedance sheath boundary condition in Stix finite element RF code. AIP Conf. Proc. 18 August 2023; 2984 (1): 060004. https://doi.org/10.1063/5.0162402

‡C. Migliore, J. Wright, M. Stowell, P. Bonoli; Using the Stix finite element RF code to investigate operation optimization of the ICRF antenna on Alcator C-Mod. Nucl. Fusion. 24 August 2023; 63 106006. https://doi.org/10.1088/1741-4326/acee11

The references are [1] and [2] respectively for the these papers. Quotations are used for text that is taken directly out of the papers followed by the symbol † or ‡ to indicate which paper it corresponds to. Any images or equations published within these papers are marked with the same method.

Contents

List of Figures

List of Tables

Chapter 1

Introduction

With rising temperatures due to climate change, there is a sense of urgency and demand to have reliable sustainable energy production. Green energy sources, such as wind and solar, are vital to relying less on coal and natural gas but aren't enough to key up with the demand of the world's electrical grid [3]. A favorable method of energy manufacturing that is able to yield significant dispatch-able electricity comes in the form of nuclear energy, either through fission or fusion. Fission power plants have long been a staple of many electrical grids but they possess issues pertaining to the byproducts produced from the fission reaction and are a widely politicised form of energy production [4]. In contrast, fusion is revered for being clean, safe, and having sufficient fuel availability whilst providing a high energy output [5].

Fusion is the nuclear reaction in which two light nuclei combine together to form a heavier nucleus that is more energetically favorable thereby releasing energy. In order for two nuclei to fuse together, they must have enough energy, on the order 10's of keV ($\sim 10^8$ °C), to overcome the repulsive Coulomb force and reach the region where the attractive nuclear force is stronger. At such high energies, the atomic nuclei are fully ionized forming a quasi-neutral gas mixture of positive ions and negative electrons known as a plasma. The two most relevant fusion reactions for generating electricity come from fusing isotopes of hydrogen, specifically deuterium (D) with atomic mass of 2 amu and tritium (T) with an atomic mass of 3 amu shown in Eqs. 1.1 and 1.2. It should be noted that for the D-D reaction in Eq. 1.1, there are two possible fusion outcomes each occurring at a 50% chance.

$$D + D \rightarrow \begin{cases} {}^4He + n + 3.27 \text{ MeV} \\ T + H + 4.03 \text{ MeV} \end{cases} \tag{1.1}$$

$$D + T \rightarrow {}^3He + n + 17.6 \text{ MeV} \tag{1.2}$$

The D-T reaction is more favorable for fusion power plants due to its large net energy

gain as a result of its high peak in fusion cross-section versus needed plasma temperature. To reach the regime in which fusion reaction rates are maximized, the plasma needs to attain the extremely hot 10's of keV temperature range. There are two approaches used to achieve this goal: inertial confinement fusion (ICF) and magnetic confinement fusion (MCF). ICF uses the idea of compressing a small target comprised of isotopes of hydrogen, like deuterium and tritium, using a pulsed high power laser to achieve fusion relevant temperatures. Although there have been experimental shots observed at the National Ignition Facility at Lawrence Livermore National Laboratory that achieve net energy gain of Q $\sim$ 1.5 [6], there are still many unknowns of how this method can be adapted to be a power plant given its pulsed nature. Alternatively, the MCF method uses magnetic fields to confine the plasma's charged particles in order to maximize confinement times. The focus of this thesis will be on a particular MCF device configuration called the tokamak that is introduced in the next section.

1.1 Nuclear Fusion using the Tokamak

One of the most promising magnetic confinement configurations for achieving and sustaining net energy gain as a power plant reactor is the tokamak. The tokamak consists of taking a cylindrical metallic vacuum vessel that has surrounding polodial magnets and bending it so that both open ends meet each other giving rise to a torus (donut) shape. The magnets around the torus create a toroidal magnetic field that closes magnetic field lines to confine the plasma using the Lorentz force. A solenoid is placed in the center of the torus to act as a transformer and creates a toroidal plasma current which induces a poloidal magnetic field. This poloidal field keeps particles from drifting out while the toroidal current provides Ohmic heating to the plasma. Lastly, coils are placed poloidally to create a vertical magnetic field that stabilizes the plasma. A schematic of the tokamak device is shown in Fig. 1.1.

Tokamaks originated in the late 1950s in the Soviet Union [8]. Since then, the evolution and performance to reach the regime in which there is more power output than input (Q $>$ 1) has made substantial progress but has yet to achieve this goal. The conventional approach forward is to build larger tokamak devices to maximize the fusion power. While this is predicted to increase Q significantly from current experiments, there are a wide variety of issues in regards to how expensive and practical these tokamaks are as power plants. However in the last decade, fusion research has lead to an entirely different approach that was previously inaccessible: increasing the toroidal magnetic field strength. The development of the high temperature superconducting (HTS) material called "ReBCO" (Rare-earth Barium Copper Oxide) has allowed toroidal magnets, which were limited to $\sim$ 9 T on axis, to reach

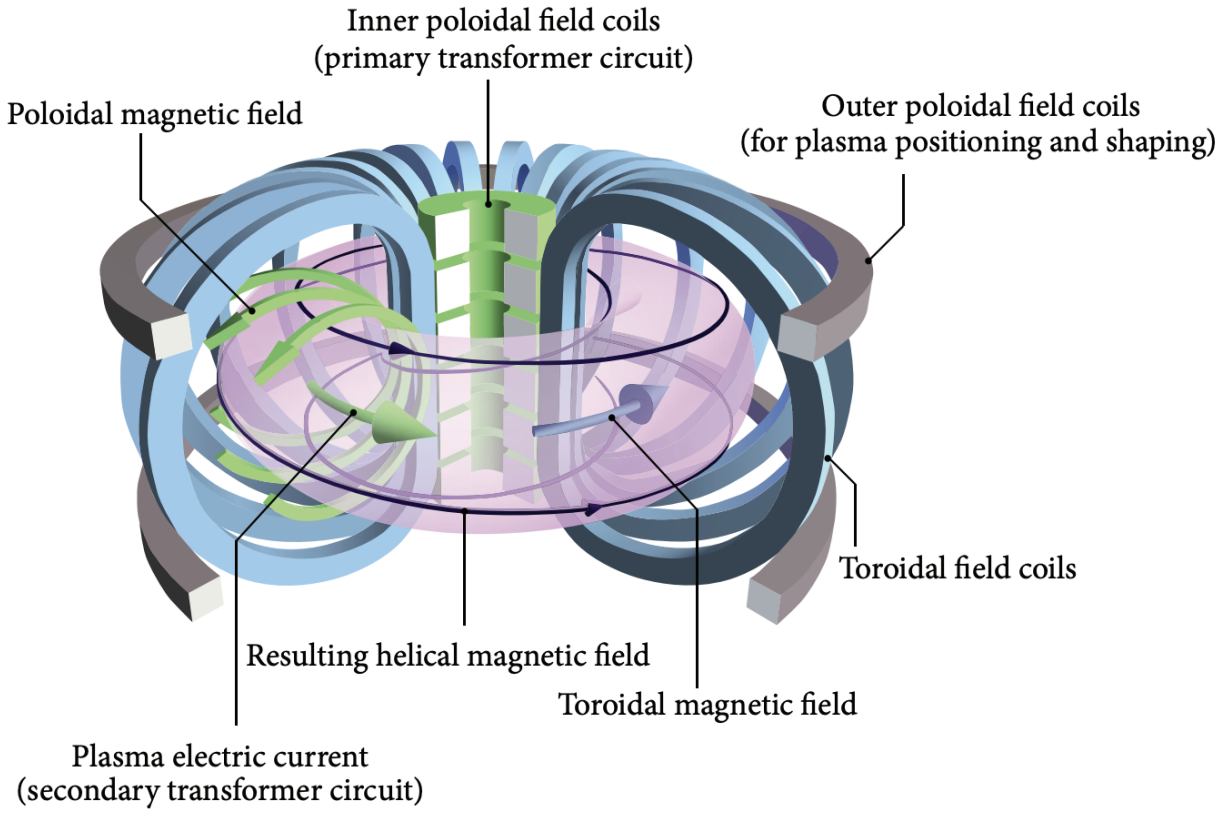

Figure 1.1: Diagram of the tokamak device consisting of a combination of toroidal, poloidal, and solenoid coils with the black lines representing the total magnetic field produced. Copyright © 2014 S. Li et. al [7].

20 T on axis [9]. ReBCO has opened up the avenue to pursue smaller tokamak devices with larger magnetic fields to reach greater Q values due to the fact that fusion power scales with the magnetic field to the fourth power, as shown in Eq. 1.3.

$$P_{fus,DT} = \frac{\beta_{max}^2 B^4}{64\mu_0^2} \frac{\langle \sigma v \rangle_{DT}}{T^2} E_{DT} \tag{1.3}$$

The development of HTS magnets has given rise to a rapidly expanding high-field fusion sector aimed to reach net energy gain faster than expected with conventional approaches.

1.2 Ion Cyclotron Radio Frequency Heating

Although the toroidal plasma current provides resistive Ohmic heat to the plasma, this is limited to a couple of keV due to plasma resistivity decreasing with increasing temperature, i.e. $\eta \propto T^{-3/2}$. Tokamaks therefore need to use external heating sources to reach the 10's of keV temperatures needed for fusion. The most common method to do this is by either using radio frequency (RF) waves or neutral beam injection (NBI). NBI, as the name implies, injects high-energy neutral particles into the plasma that then become ionized and transfer their energy to the bulk population via collisions. Although NBI has been established as a good heating source for current experiments, able to reach ∼100 keV beam energies, there is some uncertainty on how effective this method is in large fusion reactors. The main issue with larger or higher density devices is that the energy required for neutrals to penetrate into the core is much higher, on the order of ~ 1 MeV. Such NBI can be built using negative-ions but the technology is much more expensive, complicated, and requires a large physical space around the device that reduces the tritium breeding ratio of reactor blanket [10].

A favorable alternative to NBI is using radio frequency waves. This method relies on a launched wave to impart its energy to the plasma in a process known as wave-particle resonance through either cyclotron or Landau damping. From the viewpoint of heating, RF waves are typically divided into three categories based on the wave's launched frequency: ion-cyclotron (ICRF), lower hybrid (LH), and electron-cyclotron (ECRF). While the LH regime can be used for heating, these waves cannot penetrate to the core of a fusion reactor and instead damp in the outer half of the plasma where they can be used for current profile control [11]. In contrast, ICRF and ECRF provide an effective localised absorption due to the wave-particle resonance occurring at the harmonics of either the ion (Ω_i) or electron (Ω_e) cyclotron frequencies respectively where $\Omega_j = q_j|B|/m_j$. Electron cyclotron waves have the advantage of a remote launcher as opposed to ICRF but are costly to build. More problematic for ECRF is that due to launching at the electron cyclotron frequency, high

magnetic field devices require such high frequencies, upwards to $\sim$ 300 GHz, that current gyrotrons are not able to achieve in steady state.

ICRF on the other hand, uses frequencies much lower than ECRF, around $\sim$ 100 MHz, relies on well established RF antenna technology, and heat ions directly. Although ICRF is the preferred choice, there is a notable detrimental plasma-material interaction effect known as RF sheath rectification. Sheath formation is a natural consequence of confining a plasma to a vacuum vessel due to quasi-neutrality. When a plasma touches a metal wall, a negative electric charge is built up due to electrons moving faster than ions which in turn attracts ions to shield out the negative charge. This result forms a thin ($\sim$ mms) non-neutral layer on the wall called a sheath that has an electric potential drop of around 30 V depending on the electron temperature. This sheath potential is important because it is the mechanism that accelerates ions into the material surface. Although 30 V isn't enough to cause any significant sputtering of neutrals from a heavy metal wall, this potential can get appreciably higher through the non-linear rectification response when ICRF is introduced. This enhancement of potential from ICRF, described in detail in Chapter 2, has been experimentally measured to be hundreds of volts [12], [13]. With such large voltages, ions are easily able to exceed the energy threshold needed to sputter heavy material walls such as molybdenum (Mo) and tungsten (W) [14], [15]. This inflow of neutrals is harmful given that they are unaffected by both electric and magnetic fields and therefore are easily able to travel into the center of the plasma where they ionize along the way. The high Z species pollute the plasma and pose a threat by increasing the radiative power losses that scale with Z_{eff} leading to radiative collapse. As such, understanding and mitigating impurity generation through RF sheaths has been a major focus of RF fusion community.

A different consequence of RF sheath rectification is the formation of localized hot-spots and the overall decline in heating efficiency. RF sheaths can be thought of as circuits with a corresponding current, voltage, complex resistance, and a characteristic frequency of the launched ICRF wave [16]. As such, regions where the enhanced potential and resistance are large result in power dissipation in the sheath and the creation of high temperature hot spots that damage the plasma facing components. This phenomenon has been seen experimentally in various device's ICRF antennas, most notably in Tore Supra [17], Alcator C-Mod [18], and JET [19].

Lastly, it is worth mentioning the secondary effect of modifying the scrape-off layer (SOL) density due to RF sheaths. Along with the voltages on the antenna, the corresponding electric fields gives rise to convective E $\times$ B drift flows. These are known to move particles, including impurities, in the SOL causing a decline in coupling power of the antenna and altering the heat flux in the area [20], [21]. These convective cells and the associated changes to the

density have been widely observed in devices including Tore Supra [22], LAPD [23], and ASDEX-Upgrade (AUG) [24] and are an important effect to account for in ICRF heating.

RF sheaths can be separated into two different types depending on where and how they form. The first category is the "near-field" sheath that forms on the ICRF antenna and nearby plasma limiters. ICRF antennas are designed to launch a wave with $E_{\|} \approx 0$, known as a fast wave (FW), where || represents being parallel to the background magnetic field. However, in reality ICRF antennas may not be perfectly aligned to be perpendicular to the background magnetic field which results in the launch of a parasitic wave with $E_{\|} \neq 0$ known as a slow wave (SW). This SW accelerates electrons into plasma material surfaces that intersect field lines in front of the antenna. As a result of quasi-neutrality, ions are then attracted to the surface resulting in enhanced DC near-field sheath potentials.

The second type of RF sheath is known as "far-field" and can be further divided into being magnetically and not magnetically connected to the antenna. Non-magnetically connected far-field sheaths are a direct consequence of when a launched FW wave is not fully absorbed in core in a single pass. The unabsorbed FW propagates around the poloidal cross section until it eventually encounters a wall or is reflected and absorbed [25]. When FW hits a material surface which is usually not parallel with the local magnetic field, coupling to a SW occurs to satisfy a conducting wall boundary condition of $E_t = 0$ where t represents the tangential direction to the wall [16]. The other possible origin of a non-magnetically connected sheath comes from a surface wave that propagates in the SOL edge region encountering a plasma-material surface [20]. In contrast, magnetically connected far-field sheaths form in regions where the material surface intersects a magnetic field line connected to the antenna. A SW can propagate along these linked field lines far from the antenna to cause enhanced potentials farther along the torus [16].

There have been a wide variety of experimental studies aimed to reduce the formation of these parasitic RF sheaths on the ICRF antennas themselves in the near-field regime. These have led to introducing numerous optimization designs of the antenna, most notably using field-aligned Faraday screens (FS) to shield out $E_{\|}$ associated with RF rectification [26], [27], low Z coating on the FS [28] and using electrically insulating enclosures on antennas [29]. Similarity, using a parallel wavenumber $|k_{||}| < k_0 = c/\omega$ was found to reduce propagating coaxial modes and surface waves for further optimization [30], [31]. Other studies done on AUG and C-Mod have resulted in the discovery of using an ideal ratio of power between antenna straps to enhance RF image current cancellation on the antenna box [32]–[34]. This method to reduce the $E_{||}$ on the antenna surface has been so successful that it is now the concentrated focus for designing the ICRF antennas on future devices such as ITER and DEMO [35], [36]. Although much of the focus of RF sheath studies have been near

or at the antenna, experiments have shown that RF sheaths can form farther away in the torus at surfaces both magnetically and not-magnetically connected to the antenna [37]–[39]. Methods to reduce these types of RF sheaths is still an active area of research but there is experimental evidence to suggest coating wall tiles that intersect a terminating magnetic field connected to the antenna in boron leads to a decrease in measured impurities [40].

Even with the mitigation methods described above, many open questions still persist with regards to RF sheath behavior. While the mechanism of their formation is well understood, the role of other physics processes like transport effects and impurity generation in combination with RF sheaths is less known. Other questions like the contribution of far-field sheaths to global power dissipation and where in the torus they form isn't known either. A particularly challenging aspect of answering these questions is the need to perform this analysis accounting for the realistic geometry of the RF launching structures and vacuum vessel. To explore these various unresolved topics, numerical modeling is an advantageous tool to use. An efficient method to simulate an ICRF wave in the edge scrape-off layer region is to use full-wave solvers, described in detail in Chapters 2 and 3. With the introduction of a concise non-linear RF sheath boundary condition by J. Myra and D. A. D'Ippolito in 2015 [16], described in Chapter 2, there is now means to simulate RF sheaths in more realistic geometries.

1.3 Overview

This thesis aims to understand the behavior of the deleterious byproduct from ion cyclotron radio frequency (ICRF) heating in tokamak devices known as RF sheath rectification. The main focus is centered around the creation of a novel finite element cold plasma RF solver called "Stix" which is used for simulating various RF sheath formations in realistic geometries both in a comparison and predictive manner for past and future tokamak experiments respectively. In addition to its stand alone capabilities, the Stix code is mindfully designed to be part of a larger physics framework aimed to investigate RF sheaths with the inclusion of transport effects and impurity generation as growing experimental evidence suggests that these effects can no longer be ignored.

The following chapters follow evolution of the Stix code starting from its creation, onto its validation, and to lastly its prediction of future experiments. First, the fundamental physics principles of electromagnetic (EM) wave propagation and RF sheaths are introduced in Chapter 2 to provide context for discussing Stix's simulations. Here the underlying equation Stix solves, the plasma wave equation with a cold plasma dielectric, is derived and terminology commonly used in the ICRF community is reviewed. The latter half of the

chapter focuses on how a sheath forms, how a RF wave influences it, and the method to represent it in a global framework as a boundary condition.

Chapter 3 describes the main finite element framework of Stix along with the various benchmarking and validation efforts. This chapter aims to answer how successful the results from Stix are and how they compare against analytic solutions as well as other RF codes. First, the main differences between Stix and other RF sheath codes are discussed in addition to the novel approach Stix takes to bypass the issues with current approaches of other codes. For verifying the global electromagnetic wave solve, a 1D case with no RF sheaths is used to compare Stix's computed electric field to the true solution and is shown to agree. For validating the implementation of RF boundary condition in Stix, introduced in Chapter 2, an analytic case along with two different numerical 2D geometry cases are chosen and good agreement is demonstrated.

With confidence in RF sheath and electric field solve, Chapter 4 addresses the question of how well can Stix perform in reproducing experimental trends in a realistic geometry. Here, the antenna power phasing study done on the Alcator C-Mod tokamak is chosen in which the ratio of power in the two inner straps versus total power of the four straps was varied. This case corresponds to the near-field sheath regime in which the main focus is on various antenna optimization methods. Along with replicating the experiment in Stix, different phasing schemes were simulated to study the effect on enhanced potentials along with how much associated impurity production is generated with the resulting voltages. It is found that Stix is able to replicate the minimization trend found in the measurements of the enhanced potentials. Additionally, using a dipole phasing of $0/\pi/0/\pi$ resulted in a minimization skewed to the larger fraction of power on the two inner straps versus the two outer straps. Here the direction the antenna strap current for each of the 4 straps is represented as either 0 or π where 0 and π are 180° out of phase from one another. It was also seen that using either the phasing $0/\pi/\pi/0$ or a monopole phasing of $0/0/0/0$ resulted in significantly larger potentials on the antenna surfaces consistent with previous ICRF experiments on C-Mod. This simulation study additionally emphasized the importance of 3D geometric effects and physics that is neglected in full-wave electromagnetic RF solves such as RF-induced transport. Lastly, it was found that enhanced potentials for the $0/\pi/0/\pi$ phasing along with the other two antenna phasing schemes can create ions with enough energy that impact the wall surface to sputter out Boron and produce impurities in the plasma.

In Chapter 5, Stix is extended to a poloidal cross section in which non-magnetically connected far-field sheaths are investigated predictively for the upcoming SPARC tokamak. The primary focus of these simulations was to observe the effect of varying the strength of single pass wave absorption and its influence on the resulting RF potentials. It was found

that for the baseline flattop H-mode scenario using a minority ion concentration of 5% He^3 resulted in a strong single pass absorption regime and small far-field sheaths. As the helium concentration decreases the absorption becomes multi-pass, in which the wave is reflected multiple times in the cross-section before it is fully absorbed. It is predicated that in this multi-pass regime the strength of RF far-field sheaths increases, a result that is confirmed in the Stix simulations. Even in the lowest absorption cases however, the calculated voltages are not enough to cause any real sputtering of the tungsten wall. These small voltages were found to be a direct cause of the small normal component of the magnetic field, b_n, into the wall. This effect is further corroborated through the incorporation of limiter bumps along the domain walls producing regions of increased b_n that coincided with peaks in enhanced voltages.

Lastly, Chapter 6 concludes with a summary of the results found in this thesis work and its implications to extending it further. Future work discussed includes extending the Stix code to 3D to look more at operation optimization of the ICRF antenna to minimize near-field effects. Other future work discussed is investigating far-field sheaths in a different reference frame, in particular interest is including the toroidal direction which is not included explicitly in the SPARC simulations described in Chapter 5.

Chapter 2

RF Wave and Sheath Physics

This chapter describes the fundamental equations and physics involved in numerically modeling RF sheath rectification through the methods described in Chapter 3. First, the behavior of electromagnetic (EM) wave propagation in a complex medium, i.e. a plasma, is introduced through the cold plasma dielectric tensor. Consequently, the general dispersion relation of the waves is derived and using the limits of the ion-cyclotron radio frequency range, the fast wave (FW) and slow wave (SW) are established. Next, the discussion of how to resolve wave-particle resonances through the introduction of kinetic effects into the cold plasma dielectric is described. Lastly, the behavior of the RF sheath rectification is discussed through both the macroscopic and microscopic view that ultimately leads to a concise non-linear RF sheath boundary condition that is able to be used in an EM wave code.

2.1 EM Wave Propagation in a Medium

The propagation of an electromagnetic (EM) wave through a medium can be described by Maxwell's equations,

$$\vec{\nabla} \times \vec{E} = -\frac{\partial \vec{B}}{\partial t} \tag{2.1}$$

$$\vec{\nabla} \times \vec{B} = \mu_0 \vec{J} + \mu_0 \varepsilon_0 \frac{\partial \vec{E}}{\partial t} \tag{2.2}$$

If the medium is linear, then its response to the wave can be expressed through the current density, $\vec{J}$. Using Ohm's law, one can express $\vec{J}$ in terms of a conductivity tensor, $\bar{\bar{\sigma}}$, and the electric field, $\vec{E}$, through the linear relationship of

$$\vec{J} = \bar{\bar{\sigma}} \cdot \vec{E} \tag{2.3}$$

Now one can split the current density term in Eq. 2.2 into two components: the medium's response and the external current density, $\vec{J}_{ext}$, giving

$$\frac{1}{\mu_0}\vec{\nabla}\times\vec{B} = \bar{\bar{\sigma}}\cdot\vec{E} + \varepsilon_0\frac{\partial\vec{E}}{\partial t} + \vec{J}_{ext} \tag{2.4}$$

Assuming that the EM wave is a plane wave of the form $\exp(-i\omega t)$ one can now write the time derivative terms as multiples of $-i\omega$ giving,

$$\vec{\nabla}\times\vec{E} = i\omega\vec{B} \tag{2.5}$$

$$\frac{1}{\mu_0}\vec{\nabla}\times\vec{B} = -i\omega\varepsilon_0\left(\bar{\bar{\varepsilon}}\cdot\vec{E}\right) + \vec{J}_{ext} \tag{2.6}$$

where $\bar{\bar{\varepsilon}} = \bar{\bar{I}} + \frac{\bar{\bar{\sigma}}}{-i\omega\varepsilon_0}$ is known as the dielectric tensor. Combining Eq. 2.5 and Eq. 2.6 leads to the equation commonly known as the plasma wave equation given as

$$\frac{1}{\mu_0}\vec{\nabla}\times\vec{\nabla}\times\vec{E} - \omega^2\varepsilon_0\bar{\bar{\varepsilon}}\cdot\vec{E} = -i\omega\vec{J}_{ext} \tag{2.7}$$

2.1.1 The Cold Plasma Dielectric Tensor

In order to find the propagation behavior of a wave in a plasma one needs to know the plasma dielectric tensor, $\bar{\bar{\varepsilon}}$. This dielectric can be found by calculating the motion of the plasma particle species when perturbed by the EM wave. In this analysis Newton's second law of motion, $\vec{F} = m\vec{a}$, is used and is rewritten as

$$m_j\left(\frac{\partial\vec{v}}{\partial t} + \left(\vec{v}\cdot\vec{\nabla}\vec{v}\right)\right) = q_j\vec{E} + q_j\left(\vec{v}\times\vec{B}\right) \tag{2.8}$$

where j represents either the ions or electrons. Here it is assumed that the plasma is cold therefore there is no pressure force ($\nabla p = 0$) and that the force from collisions is ignored due to $\omega >> \bar{\nu}_{ei}$.

Assuming that the plasma particle's speed is small, one can solve Eq. 2.8 through linearization. Linearizing allows to solve for the response of the particle to a perturbation, in this case the EM wave. Now $\vec{v} = \vec{v}_0 + \vec{v}_1$, $\vec{E} = \vec{E}_0 + \vec{E}_1$, and $\vec{B} = \vec{B}_0 + \vec{B}_1$ where the 0 subscript refers to the equilibrium and the subscript 1 refers to the perturbation where the perturbation is assumed to be small. For simplicity assume that the plasma equilibrium is stationary, $\vec{v}_0 = 0$, and that there is no background electric field, $\vec{E}_0 = 0$. Plugging in the non-zero equilibrium and perturbed variables back into Eq. 2.8 produces 1^{st} and 2^{nd} order terms. Throwing away the 2^{nd} order terms because they are much smaller than the 1^{st} order

terms gives

$$m_j \left(\frac{\partial \vec{v}_1}{\partial t} \right) = q_j \vec{E}_1 + q_j \left(\vec{v}_1 \times \vec{B}_0 \right) \tag{2.9}$$

Assuming that the perturbed quantities of $\vec{v}_1$ and $\vec{E}_1$ behave like a wave, i.e. $\exp(-i\omega t)$, one can write $\partial/\partial t$ as $-i\omega$. For simplicity assume that the background magnetic field, $\vec{B}_0$ is only in the $\hat{z}$. Solving Eq. 2.9 under the above assumptions leads to

$$v_{x,j} = \frac{q_j}{m_j} \left(\frac{i\omega E_x - \Omega_j E_y}{\omega^2 - \Omega_j^2} \right) \tag{2.10}$$

$$v_{y,j} = \frac{q_j}{m_j} \left(\frac{\Omega_j E_x + i\omega E_y}{\omega^2 - \Omega_j^2} \right) \tag{2.11}$$

$$v_{z,j} = \frac{q_j}{m_j} \frac{i}{\omega} E_z \tag{2.12}$$

where $\Omega_j = q_j |B_0|/m_j$ represents the cyclotron frequency of the particle j. One can now relate the velocity of the particles with the conductivity tensor through

$$\vec{J}_j = q_j \vec{v}_j n_j = \bar{\bar{\sigma}}_j \cdot \vec{E} \tag{2.13}$$

Adding up all the particle species in the plasma gives the total conductivity of the plasma. Solving for $\bar{\bar{\sigma}}_j$ in Eq. 2.13 gives

$$\bar{\bar{\sigma}}_j = \frac{q_j^2 n_j}{m_j} \begin{bmatrix} \frac{i\omega}{\omega^2 - \Omega_j^2} & -\frac{\Omega_j^2}{\omega^2 - \Omega_j^2} & 0 \\ \frac{\Omega_j^2}{\omega^2 - \Omega_j^2} & \frac{i\omega}{\omega^2 - \Omega_j^2} & 0 \\ 0 & 0 & \frac{i}{\omega} \end{bmatrix} \tag{2.14}$$

Using the relation of $\bar{\bar{\varepsilon}} = \bar{\bar{I}} + \frac{1}{-i\omega\varepsilon_0}\bar{\bar{\sigma}}$ and that the particle's plasma frequency is $\omega_{p,j} = \left(\frac{q_j^2 n_j}{\varepsilon_0 m_j} \right)^2$ gives the plasma dielectric as

$$\bar{\bar{\varepsilon}} = \begin{bmatrix} S & -iD & 0 \\ iD & S & 0 \\ 0 & 0 & P \end{bmatrix} = (\bar{\bar{I}} - \hat{b}\hat{b})S + \hat{b}\hat{b}P + (i\hat{b} \times \bar{\bar{I}})D \tag{2.15}$$

where $\hat{b} = \vec{B}_0/|B_0|$ and S, P, D are known as the "Stix" coefficients [41] defined as

$$S = 1 - \sum_j \frac{\omega_{pj}^2}{\omega^2 - \Omega_j^2}, P = 1 - \sum_j \frac{\omega_{pj}^2}{\omega^2}, D = \sum_j \frac{\Omega_j}{\omega} \frac{\omega_{pj}^2}{\omega^2 - \Omega_j^2} \tag{2.16}$$

2.1.2 Wave Dispersion Relations in Cold Plasma

With $\bar{\bar{\varepsilon}}$ known one can now solve for EM wave dispersion relations in a cold plasma. For this section assume that the EM wave is a plane wave of the form: $\exp\left(i\vec{k}\cdot\vec{x} - i\omega t\right)$. Now for simplicity assume that $k_y = 0$, there is no external current density ($\vec{J}_{ext} = 0$) and again that the background magnetic field, $\vec{B}_0$, is in the $\hat{z}$ direction. Under these assumptions, Eq. 2.7 becomes

$$\vec{k}\left(\vec{k}\cdot\vec{E}\right) - k^2\vec{E} + \frac{\omega^2}{c^2}\bar{\bar{\varepsilon}}\cdot\vec{E} = \bar{\bar{D}}\cdot\vec{E} = 0 \tag{2.17}$$

Using $\vec{N} = \frac{\vec{k}c}{\omega}$, $\bar{\bar{D}}$ can be defined as

$$\bar{\bar{D}} = \vec{N}\vec{N} - N^2\bar{\bar{I}} + \bar{\bar{\varepsilon}} \tag{2.18}$$

Expanding out Eq. 2.18 by defining $\vec{N} = (N\sin\theta, 0, N\cos\theta) = \left(N_\perp, 0, N_\parallel\right)$, where θ is the angle of propagation of the EM with respect to B_0, gives

$$\bar{\bar{D}} = \begin{bmatrix} -N^2\cos^2\theta + S & -iD & N^2\sin\theta\cos\theta \\ iD & -N^2 + S & 0 \\ N^2\sin\theta\cos\theta & 0 & -N^2\sin^2\theta + P \end{bmatrix} \tag{2.19}$$

$$= \begin{bmatrix} -N_\parallel^2 + S & -iD & N_\perp N_\parallel \\ iD & -N^2 + S & 0 \\ N_\perp N_\parallel & 0 & -N_\perp^2 + P \end{bmatrix} \tag{2.20}$$

In order for $\vec{E}$ to have a non-zero solution the determinant of $\bar{\bar{D}}$ must equal zero. Solving $||\bar{\bar{D}}|| = 0$ for $N_\perp$ gives two solutions in the form of

$$N_\perp^2 = \frac{b \pm \sqrt{b^2 - 4ac}}{2a} \tag{2.21}$$

$$a = S \tag{2.22}$$

$$b = (S - N_\parallel^2)(S + P) - D^2 \tag{2.23}$$

$$c = P\left[\left(S - N_\parallel^2\right) - D^2\right] \tag{2.24}$$

Eq. 2.21 gives the relation of how the launched wave propagates through the plasma medium.

2.2 ICRF Wave Physics

2.2.1 FW and SW Dispersion Relations

Eq. 2.21 represents the two coupled solutions known as the "fast wave" (FW) and "slow wave" (SW), in which the + represents the SW while the − represents the FW. The method of decoupling these solutions leads to the commonly known dispersion relations for both the FW and SW.

Starting from Eq. 2.21, first assume that for the SW $|P| \sim N_\perp^2 >> N_\parallel^2, |D|, |S|$. Solving for $||\bar{\bar{D}}|| = 0$ under these assumptions leads to the dispersion relation of the SW given as,

$$N_\perp^2 = \frac{P}{S}\left(S - N_\parallel^2\right) \tag{2.25}$$

This dispersion relation shows that the SW has a resonance at $S = 0$, known as the "Lower Hybrid Resonance," and wave cutoffs at $P = 0$ and $N_\parallel^2 = S$ where the wave changes to and from propagating to evanescent.

Now take the other limiting case of $P \sim \frac{\omega_{pe}^2}{\omega^2}$ to be large: $|P| >> N_\perp^2, N_\parallel^2, |D|, |S|$. Applying this limit to Eq. 2.21 leads to the the following dispersion relation for the FW of,

$$N_\perp^2 = \frac{\left(N_\parallel^2 - R\right)\left(N_\parallel^2 - L\right)}{\left(S - N_\parallel^2\right)} \tag{2.26}$$

The FW's dispersion shows that there are two cutoffs at $N_\parallel^2 = R$ and $N_\parallel^2 = L$ and a wave resonance at $N_\parallel^2 = S$.

For ICRF wave physics, it is usually assumed that $N_\parallel$ is known and set by the antenna. Knowing $N_\parallel$ and the Stix coefficients values of the plasma allows one to see how the perpendicular wavelength, $\lambda_\perp$, of the wave changes with various parameters, most commonly the variable of interest is the density. Fig. 2.1 shows an example of how the FW and SW propagate in a tokamak plasma using C-Mod parameters.

2.2.2 FW and SW Polarization Relations

To find the FW and SW polarizations, one needs to solve Eq. 2.17 for the electric field. One can simplify Eq. 2.17 by using the FW and SW orderings from Section 2.2.1 when solving for the dispersion relations of the two types of waves. It should be noted that for these calculations the Stix frame of reference is chosen where $\vec{B} = B_0\hat{z}$.

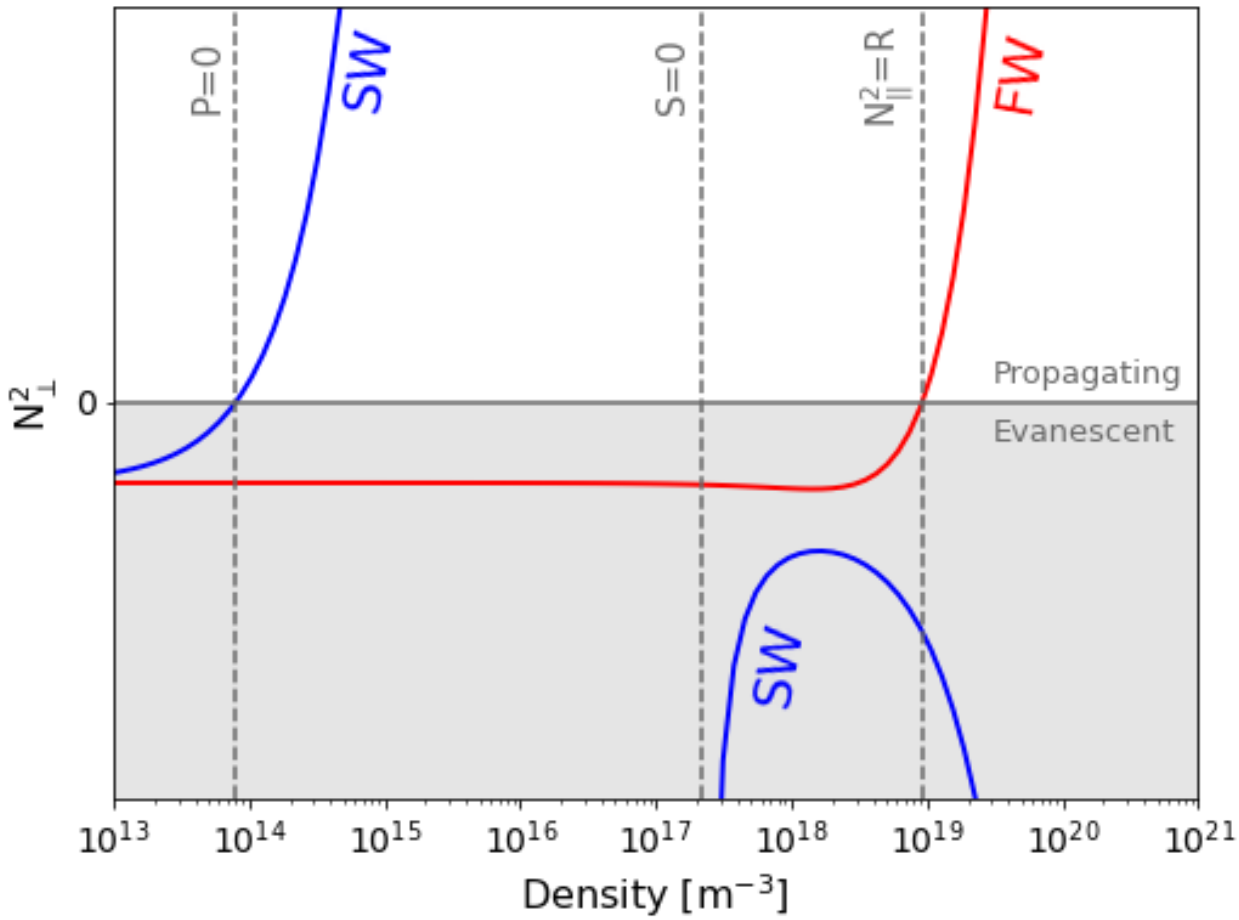

Figure 2.1: Dispersion relation plot of both the fast (FW) and slow (SW) waves using C-Mod parameters: $k_{||} = 10.8\ m^{-1}$, $|\vec{B}_0| = 5.4$ T, $f = 80$ MHz, deuterium plasma with varying density. Note that the $N_\perp^2$ for the FW branch has been scaled up by 10^3 to be visible with the SW $N_\perp^2$ values.

For the FW, $|P| >> N_\perp^2, N_\parallel^2, |D|, |S|$ therefore Eq. 2.17 is simplified to

$$\begin{bmatrix} -N_\parallel^2 + S & -iD \\ iD & -N^2 + S \end{bmatrix} \begin{bmatrix} E_x \\ E_y \end{bmatrix} = \begin{bmatrix} 0 \\ 0 \end{bmatrix} \tag{2.27}$$

Solving Eq. 2.27 gives the FW polarization as

$$\frac{E_x}{E_y} = \frac{iD}{S - N_{||}^2} \tag{2.28}$$

which shows that the FW is right-hand circularly polarized wave.

Next for the SW, the ordering of $|P| \sim N_\perp^2 >> N_\parallel^2, |D|, |S|$ therefore Eq. 2.17 is simplified to

$$\begin{bmatrix} -N_\parallel^2 + S & N_\parallel N_\perp \\ N_\parallel N_\perp & -N_\perp^2 + P \end{bmatrix} \begin{bmatrix} E_x \\ E_z \end{bmatrix} = \begin{bmatrix} 0 \\ 0 \end{bmatrix} \tag{2.29}$$

Solving Eq. 2.29 gives the SW polarization as

$$\frac{E_x}{E_z} = \frac{N_\parallel N_\perp}{N_{||}^2 - S} \tag{2.30}$$

which shows that the SW's electric field is largely parallel to the background magnetic field.

2.3 Adding Kinetic Effects to the Cold $\bar{\bar{\varepsilon}}$

In the cold plasma limit ICRF regime, a singularity arises in the S and D Stix coefficients as seen in Eq. 2.16 when $\omega = \Omega_i$ where i is the ion species that represents the wave-particle ion cyclotron resonance. One way to resolve this is to add some finite amount of imaginary collisional frequency, ν, to the ion cyclotron frequency term to represent damping. One can add some arbitrary amount on the order of $\nu/\omega \sim 1$ but a more physical way to smooth out the resonance in the cold plasma limit is to add kinetic effects back into the dielectric tensor, $\bar{\bar{\varepsilon}}$, important for simulations discussed in Chapter 5.

In this section, expressions for the S, D, and P cold plasma dielectric coefficients are replaced with lower order kinetic corrections from the hot plasma dielectric [41] given by,

$$\bar{\bar{\varepsilon}} = 1 + \sum_j \bar{\bar{\chi}}_j, \quad \bar{\bar{\chi}}_j = \left(\frac{\omega_{p,j}^2}{\omega} \sum_{n=-\infty}^{\infty} e^{-\lambda} \bar{\bar{\mathbf{Y}}}_n \right)_j \tag{2.31}$$

where

$$\bar{\bar{\boldsymbol{Y}}}_n = \begin{pmatrix} \frac{n^2 I_n}{\lambda} A_n & -in\left(I_n - I_n'\right) A_n & \frac{k_\perp}{\Omega}\frac{nI_n}{\lambda} B_n \\ in\left(I_n - I_n'\right) A_n & \left(\frac{n^2}{\lambda} I_n + 2\lambda I_n - 2\lambda I_n'\right) A_n & \frac{ik_\perp}{\Omega}\left(I_n - I_n'\right) B_n \\ \frac{k_\perp}{\Omega}\frac{nI_n}{\lambda} B_n & -\frac{ik_\perp}{\Omega}\left(I_n - I_n'\right) B_n & \frac{2(\omega - n\Omega)}{k_\parallel v_{th,\perp}^2} I_n B_n \end{pmatrix} \tag{2.32}$$

where

$$A_n = \frac{Z\left(\zeta_n\right)}{k_\parallel v_{th}}, \quad B_n = -\frac{Z'\left(\zeta_n\right)}{2k_\parallel}, \quad \lambda = \frac{k_\perp^2 v_{th}^2}{2\Omega^2}, \quad \zeta_n = \frac{\omega - n\Omega}{k_\parallel v_{th}} \tag{2.33}$$

Here $I_n = I_n(\lambda)$ is the modified Bessel function, v_{th} is the thermal speed of the particle j taken to be $\sqrt{2T_e/m_j}$, and

$$Z(\zeta_n) = \frac{1}{\sqrt{\pi}} \int_{-\infty}^{\infty} dz \frac{e^{-z^2}}{z - \zeta_n}, \quad \mathrm{Im}\,\zeta > 0 \tag{2.34}$$

For the case in which this method is used, the only expression to have a $k_\perp$ included is the second harmonic terms of S and D. To calculate this $k_\perp$ the cold plasma dispersion relation for a FW, Eq. 2.26, is used. Here only the finalized expressions are shown in Eqs. 2.35 - 2.37, the full derivation of the thermally corrected Stix coefficients can be found in Appendix B. The S and D coefficients have corrections to the ion terms to resolve the wave-particle resonances of the 1st and 2nd ion cyclotron harmonics while the P coefficient includes a correction to electron term to include electron Landau resonance.

$$\begin{aligned} S = 1 - \frac{\omega_{p,e}^2}{\omega^2 - \Omega_e^2} + \frac{\omega_{p,i}^2}{\omega}\frac{e^{-\lambda}}{2k_\parallel v_{th,i}}\left[Z\left(\zeta_1\right) + Z\left(\zeta_{-1}\right)\right] \\ + \frac{\omega_{p,i}^2}{\omega}\frac{\lambda e^{-\lambda}}{2k_\parallel v_{th,i}}\left[Z\left(\zeta_2\right) + Z\left(\zeta_{-2}\right)\right] \end{aligned} \tag{2.35}$$

$$\begin{aligned} D = \frac{\Omega_e}{\omega}\frac{\omega_{p,e}^2}{\left(\omega^2 - \Omega_e^2\right)} - \frac{\omega_{p,i}^2}{\omega}\frac{e^{-\lambda}}{2k_\parallel v_{th,i}}\left[Z\left(\zeta_1\right) - Z\left(\zeta_{-1}\right)\right] \\ - \frac{\omega_{p,i}^2}{\omega}\frac{\lambda e^{-\lambda}}{2k_\parallel v_{th,i}}\left[Z\left(\zeta_2\right) - Z\left(\zeta_{-2}\right)\right] \end{aligned} \tag{2.36}$$

$$P = 1 - \frac{\omega_{p,e}^2}{k_\parallel^2 v_{th,e}^2} Z'\left(\zeta_0\right) - \frac{\omega_{p,i}^2}{\omega^2} \tag{2.37}$$

2.4 RF Sheath Physics

2.4.1 The Bohm Sheath

When a plasma encounters a surface, a natural phenomenon called the "Bohm sheath" occurs at the plasma-material boundary. Using a Langmuir probe as an example, when a plasma device is turned on and the plasma forms, electrons due to their mass are initially attracted to the probe causing a negative charge to form at the surface. This excess negative charge leads to a potential drop which then accelerates ions and decelerates electron flow into the surface so that the current densities exactly cancel and there is no charge depletion. This potential drop is given by

$$V_{wall} = \frac{T_e}{2e} \ln \left[\frac{2\pi m_e}{m_i} \left(1 + \frac{T_i}{T_e} \right) \right] \tag{2.38}$$

which is found by equating the perpendicular ion and electron fluxes into the surface. For a hydrogen plasma when $T_e = T_i$, V_{wall} is on the order of $3T_e/e$ V $\sim$ 30 V for a 10 eV plasma. This thin region where the potential drop occurs, known as a sheath, is non-neutral in which $n_i > n_e$ and is on the order of a few millimeters.

The above description of the sheath is overly simplified, in reality they are much more complex. First, sheaths can be either magnetized or un-magnetized depending on whether a background magnetic field exists or the angle of the magnetic field into the material surface. The un-magnetized sheath, which exists when there isn't a background magnetic field or when the angle of the field lines is 90° into the wall, is broken up into two sections: pre-sheath and the Debye sheath. Fig. 2.2 illustrates the two distinct regions where the larger pre-sheath region, on the order of an ion Larmor radius, forms in between the bulk plasma and the Debye sheath/material surface. Here quasi-neutrality is still maintained but there is a potential drop of $V_{ps} = 0.7\ T_e/e$ V that exists in order to have an electric field that overcomes ion inertia and accelerates it into the Debye sheath to satisfy what is known as the Bohm-sheath criterion given as

$$v_i > c_s = \sqrt{\frac{T_e}{m_i}} \tag{2.39}$$

Figure 2.3 shows how the sheath looks when there is an oblique angle of the magnetic field with respect to the wall, ψ. Here, there is an additional region of a magnetized pre-sheath that is in between the Debye sheath and pre-sheath. This magnetized sheath will form as long as the angle of the magnetic field is larger than the minimum angle of formation given

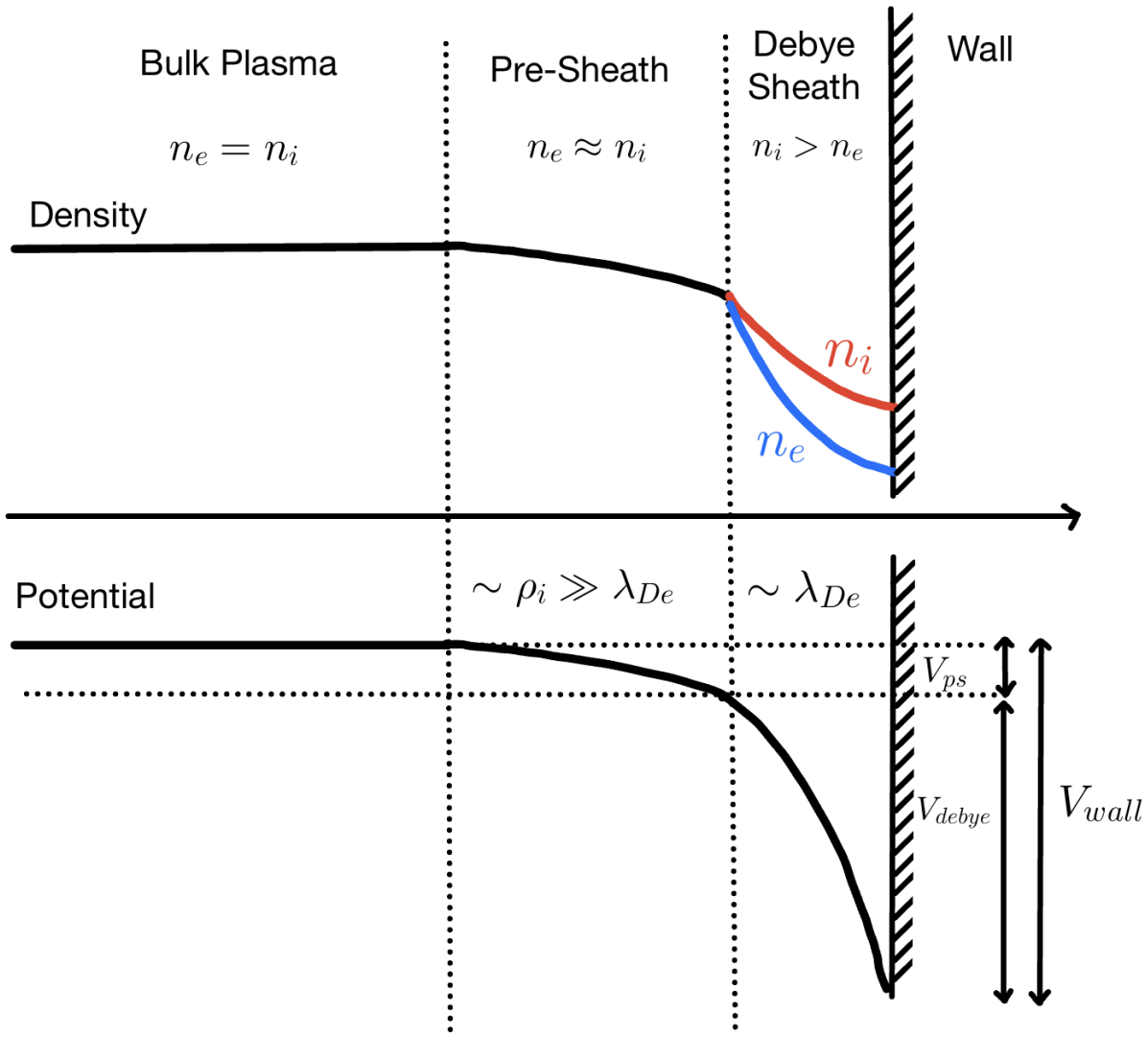

Figure 2.2: Not to scale diagram of the positional variation of both the plasma density (top) and the potential (bottom) profiles for the various regions of the sheath.

by

$$\cos\psi > \left(\frac{m_e}{2\pi m_i}\right)^{1/2} \tag{2.40}$$

Similar to the un-magnetized pre-sheath, the magnetized pre-sheath is on the order of the

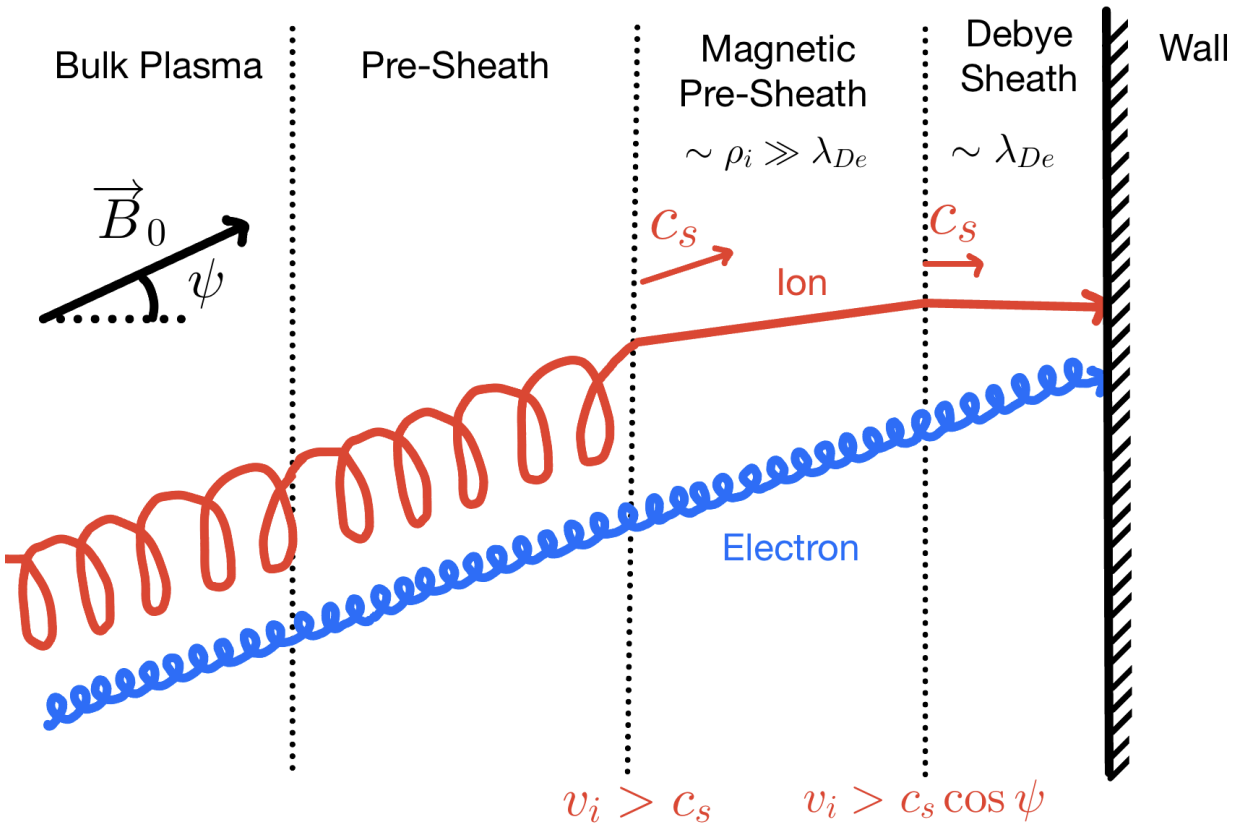

Figure 2.3: Not to scale diagram of the magnetized sheath in which the red line indicates the path of an ion while the blue line indicates the path of an electron. Here ψ is the angle of the external magnetic field, $\vec{B}_0$, and the normal direction of the wall.

ion Larmor radius in thickness. In this region, the electric field needs to overcome the ion inertia and the $qv \times B$ Lorenz force. This region exists in order to turn the sonic/supersonic ion flow from the parallel-to-B direction to the parallel-to-the-surface-normal direction, i.e.

$$v_i > c_s \;\rightarrow\; v_i \cos\psi > c_s$$

The potential drop in this region can be found by equaling the ion fluxes at the entrance to the magnetic pre-sheath and the entrance to the Debye sheath giving

$$V_{MPS} = \frac{T_e}{e} \ln\cos\psi$$

Even though V_{MPS} is dependent on the magnetic field angle, V_{wall} for the magnetized sheath is still given by Eq. 2.38. The dependence on the magnetic field angle varies the split between V_{debye} and V_{MPS} that sum up to $V_{wall} = V_{MPS} + V_{debye}$.

2.4.2 RF Sheath Rectification

Section 2.4.1 describes the thermal Bohm sheath which is a static direct current (DC) voltage on plasma facing components. For plasma devices that use ICRF power, RF waves can propagate into material wall boundaries and influence the sheath causing what is known as RF sheath rectification. It is not unusual to measure $\sim$ 200 - 400 V on PFCs due to ICRF waves that in turn produce the adverse effects as described in Chapter 1 [20].

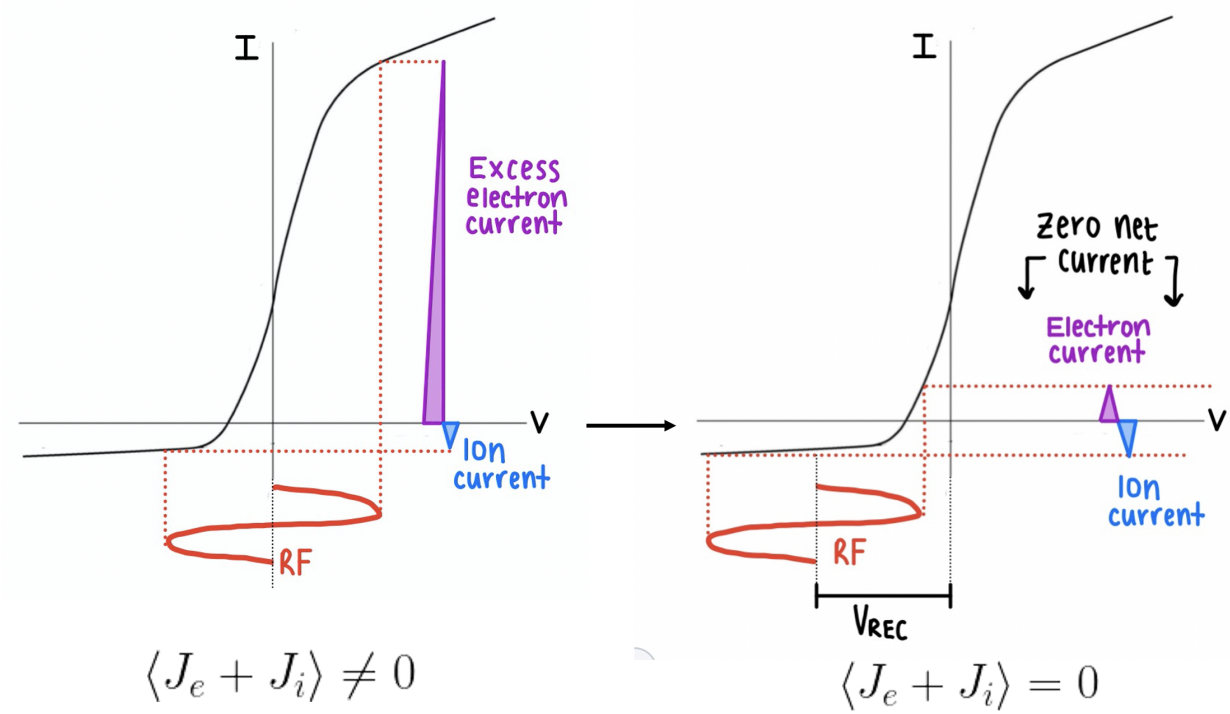

Figure 2.4: Diagram illustrating the mechanism of RF sheath rectification. It is seen that at the positive swing of the RF wave, there is an excess electron current into the wall when compared to the ion current at the negative swing of the RF wave. The plasma responds by creating a DC bias that cause the ion and electron currents to cancel when averaged over the period of the wave.

The actual process of RF sheath rectification can be visualized by looking at a voltage (V) versus the total current flowing into a material surface (I) plot shown in Fig. 2.4. The shape of the current curve lends itself to the behavior of the ions versus the electrons. When the voltage is biased positively on the material surface there is an excess of electrons flowing

known as the electron saturation current. Conversely, when there is a negative bias on the surface, there is an excess of ion current flowing known as the ion saturation current. The non-linear behavior of the total current in the middle of the two extrema arises from the exponential in the electron current due to its Boltzmann response. A RF wave can be thought of as just an oscillating voltage that swings negatively and positively. Visualizing the RF voltage on the I-V curve, seen in Fig. 2.4, shows that due to the non-linearity in the electron current, the positive swing of the RF wave's amplitude produces an excess electron current that does not cancel the ion current on the opposite swing when time averaged leading to charge depletion. The plasma in response to this adds an additional DC voltage bias, V_{REC}, that decreases the excess electron current to cancel out the ion current response as seen in the I-V curve. It is this V_{REC} that is commonly referred to as the rectified potential that can be on the order of 100's of volts.

The following two sections describe the macro and micro-scale physics of the RF sheath developed by J. Myra et. al 2015 [16] and J. Myra 2017 [42].

The Microscopic View

This section summaries the work found in J. Myra 2015 and J. Myra 2017 that lay the foundation to the RF sheath boundary condition used in this thesis work.

J. Myra et. al 2015 [16] formulated RF sheaths to be thought of as a circuit element with a complex impedance, z_{sh}, at the driving frequency of the RF wave, ω, dependent on the plasma properties, that follows the non-linear relation of

$$\frac{1}{z_{sh}} = \frac{\langle J_{x,sh} V_{sh} \rangle}{\langle V_{sh}^2 \rangle} - \frac{i\omega \left\langle J_{x,sh} \frac{dV_{sh}}{dt} \right\rangle}{\left\langle \frac{d^2 V_{sh}}{dt^2} \right\rangle} \tag{2.41}$$

where the $\langle\ \rangle$ brackets denote a time average over a wave period.

It was chosen that the complex impedance, z_{sh}, will encapsulate the micro-scale physics of the electrons and ions within the thin layer of the RF sheath. To find z_{sh}, J. Myra et. al 2015 [16] uses a model of two plasma-filled parallel plates that are driven out of phase using an oscillating voltage. To solve Eq. 2.41, one needs to use the Poisson's equation (Eq. 2.42), the Boltzmann relation (Eq. 2.43), the continuity equation (Eq. 2.44), the ion equation of motion under the Lorentz force (Eq. 2.45), and ensuring that the currently density on both ends of the plates cancel one another.

$$\frac{\partial^2 \Phi}{\partial x^2} = -\frac{e}{\varepsilon_0} \left(Z_i n_i - n_e \right) \tag{2.42}$$

$$n_e = n_0 \exp\left\{\frac{e}{T_e}\left(V_{sh} - \Phi_0\right)\right\} \tag{2.43}$$

$$\frac{\partial n_i}{\partial t} + \frac{\partial}{\partial x}\left(n_i u_x\right) = 0 \tag{2.44}$$

$$\left(\frac{\partial}{\partial t} + u_x \frac{\partial}{\partial x}\right)\vec{u} = -\nabla\Phi + \Omega_i \vec{u} \times \vec{B}_0 \tag{2.45}$$

Here, the x denotes the normal direction into the plate, Φ_0 is the upstream potential, V_{sh} is the potential at one of the plates, and Φ represents the electrostatic potential variable. Additionally, one can define the current density into one plate as,

$$J_{x,sh} = Z_i e n_{i,sh} u_{x,sh} - e n_0 \left(\frac{m_i}{2\pi m_e}\right)^{1/2} \exp\left\{\frac{e}{T_e}\left(V_{sh} - \Phi_0\right)\right\} \sin\theta - \frac{\partial}{\partial t}\left(\frac{\partial V_{sh}}{\partial x}\right) \tag{2.46}$$

Where θ is the angle of the magnetic field and the wall. Eq. 2.46 represents the total current (ion, electron, and displacement) into one of the plates. Solving Eqs. 2.42 - 2.46 to find J_{sh} and V_{sh} and plugging into Eq. 2.41 gives an expression for z_{sh}.

Solving this non-linear fluid model of J. Myra et. al 2015 [16] is not ideal for a global RF wave propagation solve. Using the basis of the model described above, J. Myra 2017 [42] introduces a parameterization code that combines numerical and analytical results to create a subroutine that only needs to know four parameters to calculate z_{sh} and the rectified potential ($V_{REC} = \langle\Phi_0\rangle$): the wave's angular frequency (ω), the ion cyclotron frequency (Ω_i), the angle of the magnetic field into the wall (b_x), and the zero-to-peak amplitude of the RF wave at the sheath (ξ). It is this parameterization code that is used to calculate z_{sh} for every reference to z_{sh} in equations following this subsection.

The Macroscopic View

A visualization of the interfaces of the plasma facing component, sheath, and plasma is seen in Fig. 2.5. Because the wavelength of the ICRF wave is much larger than the sheath thickness, i.e. λ of the ICRF $>> \Delta$, the sheath can be represented as boundary condition (BC) on the sheath-plasma interface and can be effectively thought of as 1D when looking at the global RF wave behavior.

The RF sheath BC in J. Myra et. al 2015 [16] is derived from the continuity of the normal component of $\vec{D} = \bar{\bar{\varepsilon}} \cdot \vec{E}$ across the two mediums: the plasma and sheath. D_n can be rewritten in terms of the total normal current density giving the continuity relation of: $J_{n,pl} = J_{n,sh}$ where pl denotes the plasma side and sh denotes the sheath side. Next, one can express the total normal current density in the sheath to the sheath's impedance and potential drop giving $J_{n,sh} = -V_{sh}/z_{sh}$, where the negative sign is included to account for

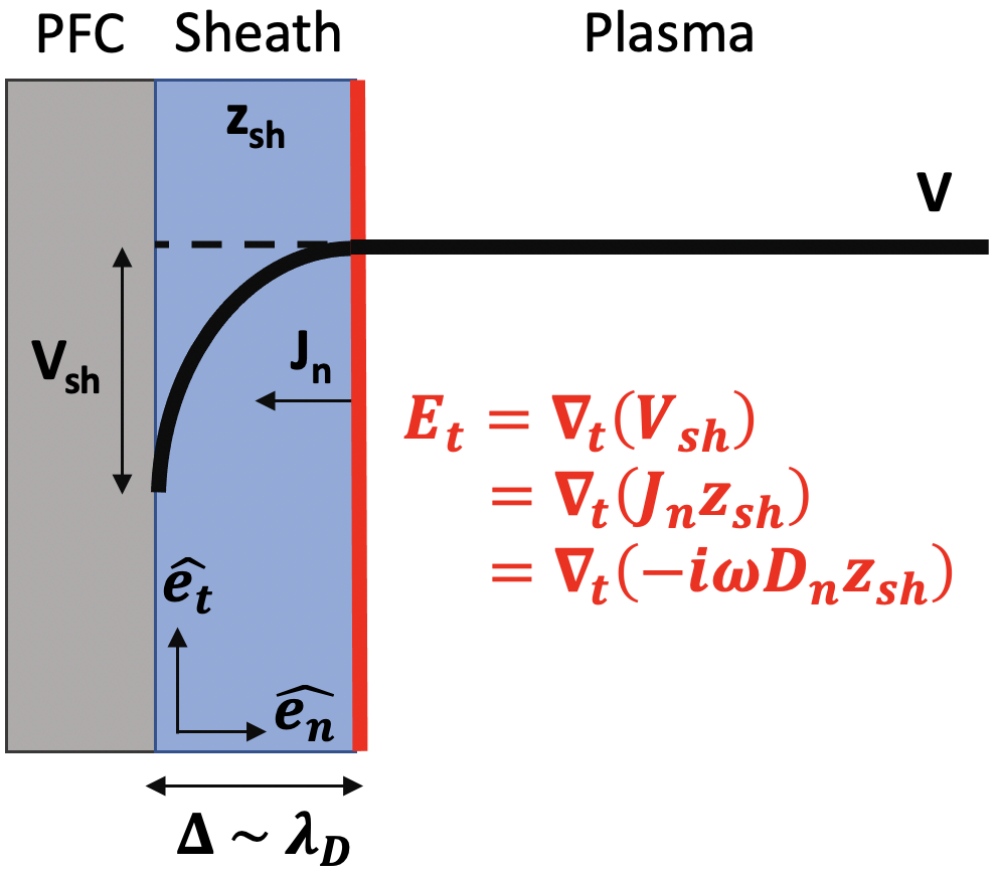

Figure 2.5: A pictorial diagram of the three regions of interest when describing RF sheaths: the plasma facing component (PFC), the sheath, and the plasma. A boundary condition on the tangential electric field encompasses the micro-scale physics of thin sheath region, denoted by the red line on the sheath-plasma interface.

the assumption that the wall is grounded. Now an expression for the sheath potential can be expressed as $-V_{sh} = J_{n,pl} z_{sh}$. To get a BC representation of the sheath potential in terms of the electric field, one can take the tangential gradient to get: $E_t = \nabla_t \left(J_n z_{sh} \right)$, where the pl subscript will be dropped henceforth. Lastly one can rewrite J_n in terms of the normal electric displacement on the plasma side using Fourier analysis giving the most common form of the sheath boundary condition of

$$E_t = \nabla_t \left(V_{sh} \right) = \nabla_t \left(-i\omega D_n z_{sh} \right) \tag{2.47}$$

Eq. 2.47 bridges together the microscopic view of the RF sheath through the complex sheath impedance, z_{sh} and the macroscopic wave propagation. This sheath BC can be thought of as being applied to the entrance of the magnetic presheath [16]. Additionally, it should be noted that the BC is electrostatic. This approximation can be used if the following condition is satisfied: $|k_t \Delta| << 1$, i.e. a thin sheath approximation allows for E_t to be electrostatic since the variation in the tangential direction is very large with respect to the thickness of the sheath.

Chapter 3

The Development of the "Stix" Code

This chapter describes the development of the code "Stix" [1]; the tool used to investigate the open questions of RF sheath outlined in the introduction. First described are the primary motivations for the creation of Stix, the underlying equations that are solved for, as well as the finite element discretization of them. As a verification of the global field solve, an analytic 1D case is used to compare the L^2 norm error in addition to the global L^2 norm error convergence behavior with increasing resolution. Next, the novel implementation of the full non-linear RF sheath boundary condition (BC) is discussed as well as four verification cases from literature are chosen. Lastly, the chapter describes a method of optimizing the fixed point iteration of the RF sheath BC called the minimal polynomial extrapolation method, MPE, along with the results using two test cases.

3.1 Overview of Stix

Stix [1] is a parallelized cold-plasma frequency domain RF wave solver that is built off of the open source scalable finite element library called MFEM (Modular Finite Element Methods) [43]. One of the key features of Stix is the incorporation of a fully non-linear RF sheath finite impedance boundary condition formulated by J. Myra et. al 2015 [16] critical for simulating both near and far-field sheath effects. A detailed description on how to setup and run Stix can be found in Appendix A.

The first step in the creation of Stix was the decision to use the finite-element method and in particular the MFEM library. The finite element method has many advantages to other numerical methods but the most prominent one is the support of using complex geometric meshes. As long as there is enough numerical resolution, the finite-element method can capture the features of ICRF antennas such as the Faraday shields important for near-field sheath formation. The finite-element method solves complex partial differential equations

(PDEs) by sub-dividing the computational domain into smaller areas called elements. In each element, the behavior of the PDEs is approximated by basis functions and interpolated using polynomials of an order specified by the user. The solution is then obtained by integrating over the entire computational domain.

For accessibility of Stix to the greater fusion community, the open source finite-element library of MFEM [43] was chosen. The MFEM library's advantages are that it is accessible and is highly scalable thus designed for high performance computing. Examples of this include GPU capability, mesh optimization, high order basis functions, arbitrary order geometry, adaptive mesh refinement, and many specialized preconditioners for iterative solvers.

Due to MFEM being inherently 3-dimensional, Stix too is 3-dimensional. However at this time Stix is only able to support 1D and 2D problems with plans to expand to 3D in the near future. Stix requires an input of a 2D mesh that is extruded into the 3rd dimension using 3 elements. To mimic either 1D or 2D problems on a 3D mesh, the other 2 or 1 dimension(s) respectively are represented using phase factors. These phase factors are incorporated into what are known as "Floquet" boundary conditions where the solution in the dimension(s) not represented is shifted by a phase, k, i.e. $\mathrm{A}(0) = \mathrm{A}(0)e^{ikL}$ where L is the end of the domain in that direction. This phase factor is typically chosen to be the $k_{||}$, a value that is set physically by the ICRF antenna in experiments. In simulations where the antenna's spectrum isn't represented in the problem, in particular for polodial cross section simulations, the phase factor is user specified to be $k_{||}$. Stix is able to support various custom parameterized density, temperature (for artificial collisionality or for thermal corrections to the Stix coefficients), and magnetic field profiles. In order to better mimic experimental runs on tokamaks, Stix also is able to use equilibrium magnetic field data from EQDSK files to setup a more realistic background magnetic field.

Stix is a cold-plasma solver meaning that there are no temperature and therefore kinetic effects included, with the exception of the lowest order thermal corrections discussed in Chapter 2. To incorporate dissipation of the wave, there are two options available in Stix: imposing artificial collisionality through an effective mass and adding lower order thermal corrections to the cold plasma dielectric. The first option is the most common way cold-plasma RF codes include damping effects. This is done by adding an imaginary component to the mass of the electrons in the cold-plasma dielectric, i.e. $m_{eff} = m_e\left(1 + i\nu/\omega\right)$, where ν is either user-specified or the true thermally distributed electron-ion collisional frequency of

$$\bar{\nu}_{ei} = \frac{2}{3(2\pi)^{\frac{1}{2}}} n_i \left(\frac{Ze^2}{4\pi\epsilon_0}\right)^2 \frac{4\pi}{m_e^{\frac{1}{2}} T_e^{\frac{3}{2}}} \ln\Lambda_e \tag{3.1}$$

While the electron-ion collision frequency ($\bar{\nu}_{ei}$) is physically present in a real plasma, in a typical tokamak plasma scenario this value tends to be much lower than the frequency of the launched wave, $\bar{\nu}_{ei} \sim 10^5 << \omega \sim 10^8$, and therefore is commonly neglected.

Having a non-zero ν value is useful for mimicking an absorbing boundary condition or resolving resonances which frequently show up in ICRF simulations. There are two types of resonances that are not able to be resolved without some imaginary contribution to the Stix coefficients: wave and wave-particle resonances. Wave resonances occur when the denominator of the dispersion relation goes to 0 in the cold-plasma formulation. Physically this means that the wave goes from propagating to evanescent or vice versa, most commonly this is the lower-hybrid resonance of the SW that occurs near the antenna at around a density of $\sim 10^{17}\ m^{-3}$. Wave-particle resonances on the other hand occur when the ICRF wave is cyclotron damping on the ions, i.e. $\omega = \Omega_i$. For poloidal cross section simulations of tokamaks, wave-particle resonances are critical for simulating the ICRF wave's behavior as it traverses the cross section. For this reason, the lower order thermal corrections on $k_{\perp,\mathrm{FW}}$ from the hot plasma dielectric are incorporated into Stix's cold plasma dielectric for the first and second cyclotron harmonics. These thermally corrected expressions for S, D, and P (for electron Landau damping) are described in Section 2.3 and derived in Appendix B.

3.2 Motivation Behind Stix's Creation

Stix is not the only cold-plasma RF code to have a RF sheath boundary condition included, other similar codes of particular interest are "COMSOL" [44], "SSWICH" [45], [46], "rfSOL" [47], and "Petra-M" [48], [49]. There are however some limitations to these codes that leave room for the novelty of Stix. The COMSOL code uses a thick dielectric layer approximation for RF sheath which is linear and overestimates sheath potentials. Additionally, this formulation ignores the minimum sheath angle formation criterion, Eq. 2.40, that is important for realistic geometry. SSWICH is a solely 2D code that currently does not have the capability of simulating the high-field side of the torus, important for not-magnetically connected far-field sheaths, and it uses the capacitive limit of J. Myra's BC that does not allow for the sheath dissipation to be calculated [46]. The rfSOL code uses a custom finite-element method framework that is not open-source, not scalable, and may also be less flexible for complex geometries that the MFEM toolkit permits, such as antennas and limiter surfaces. Lastly, Petra-M is built off the same library of MFEM as Stix but has a large code framework introducing added complexity in coupling with other codes for the purposes of integrated modeling and currently uses an asymptotic expansion of the sheath BC, i.e. $z_{sh} \to \infty$, leading to a BC with an insulating limit [49]. Stix and Petra-M RF sheath development

was done through a collaborative benchmarking exercise and the Stix code is meant to be complementary to it. Having both Stix and Petra-M has led to various insights on improving the solution method and its limitations through the validation of the RF sheath BC that would have otherwise not been identified.

Stix bridges the gap in the space of cold-plasma RF solvers that include some form of a RF sheath boundary condition by offering a relatively light weight but full featured high performance computing (HPC) capability. Stix can be used for evaluating a wide variety of RF sheath geometric and plasma scenarios and uses the complete non-linear version of the RF sheath BC which is solved concurrently with the field solve allowing for fast convergence. The simplicity but robustness of the code is intended to provide an easier platform for both coupling to other codes as an integrated model and being a testbed for various numerical methods. Moving forward, a key component of simulating plasma-wall interactions under RF will be to have an integrated model that includes various time-scale processes like E×B convective flows and the influx of impurities from the rectified surface voltages. With this goal in mind, Stix was designed to be part of a multi-physics workflow that includes the fluid transport code "MAPS" [50] that is also built off MFEM and an impurity generation code that will provide a more complete picture of the impacts of RF sheath rectification.

3.3 The Fundamental Equations of Stix

Electromagnetic plasma codes traditionally solve for the electric field in the plasma wave equation derived in Chapter 2, repeated here as

$$\frac{1}{\mu_0}\vec{\nabla}\times\vec{\nabla}\times\vec{E}-\omega^2\varepsilon_0\bar{\bar{\varepsilon}}\cdot\vec{E}=-i\omega\vec{J}_{ext} \tag{3.2}$$

For Stix, it was a deliberate choice to solve instead for the magnetic field, $\vec{H}$, in the plasma wave equation given by

$$\vec{\nabla}\times\bar{\bar{\varepsilon}}^{\,-1}\left(\vec{\nabla}\times\vec{H}\right)-\omega^2\mu_0\vec{H}=\vec{\nabla}\times\bar{\bar{\varepsilon}}^{\,-1}\vec{J}_{ext} \tag{3.3}$$

The decision to solve Eq. 3.3 instead of Eq. 3.2 was for optimizing the incorporation of the RF sheath BC, repeated here as

$$E_t=\nabla_t\left(V_{sh}\right)=\nabla_t\left(-i\omega D_n z_{sh}\right)=\nabla_t\left(\hat{n}\cdot\left(\vec{\nabla}\times\vec{H}\right)z_{sh}\right) \tag{3.4}$$

It is seen that Eq. 3.4 is dependent on the normal component of the electric displacement, D_n, along with z_{sh} being dependent on V_{sh}, as described in Section 2.4.2, thereby making

the expression non-linear. If one were to solve for the wave fields using Eq. 3.2 with Eq. 3.4, it would require a two-step iteration of:

1. Take an initial guess for $V_{sh,i}$ and find the associated $z_{sh,i}$.
2. Solve Eq. 3.2 with Eq. 3.4 using the values from step 1.
3. Find $D_{n,i+1}$ to update $V_{sh,i+1}$ as $-i\omega D_{n,i+1} z_{sh,i}$.
4. Use updated $V_{sh,i+1}$ as new guess for Eq. 3.4.
5. Repeat solve until norm of the electric field solution is no longer changing: $\left|\left|\vec{E}_{i+1}\right|\right| - \left|\left|\vec{E}_{i}\right|\right| <$ convergence criterion.

There are two fundamental issues with the method described above. First, it is not ideal for complicated geometric problems due to the computational expenses and more importantly using the finite element method makes this computation very challenging if one wants to use the full non-linear nature of the BC. To elaborate further on the latter point, one first needs to describe the various finite element basis functions used to solve these types of problems. Table 3.2 describes the four most common basis functions, each of which belong to a mathematical basis space as indicated by the second column. This mathematical space dictates the basis function and its derivative, depending on whether it is scalar or vector, associated continuity along elements. Fig. 3.1 illustrates how each of the basis space represents the solution and corresponding continuity on an element.

Name	Space	Type	Continuity	Derivative	Derivative Space
Lagrange	H^1	Scalar	Fully Continuous	Gradient	$H(curl)$
Nédélec	$H(curl)$	Vector	Tangential	Curl	$H(div)$
Raviart-Thomas	$H(div)$	Vector	Normal	Divergence	L^2
Discontinuous	L^2	Scalar	None	None	N/A

Table 3.1: Descriptions of the various types of finite element basis functions commonly used in MFEM, their continuity along elements, and which mathematical space their derivatives belong to. The Stix code uses the Nédélec basis to represent the computed $\vec{H}$ and the Raviart-Thomas to represent the computed $\vec{D}$.

Using the natural basis space of Nédélec when solving a curl curl PDE leads to a fundamental issue when representing the RF sheath BC. It is seen that Nédélec has only tangential continuity and therefore the normal component of the $\vec{E}$ field that corresponds to the degrees of freedom on the boundary surface is not known [49]. This becomes a problem since D_n needs to be a known value for the sheath BC. To find D_n one must change basis space

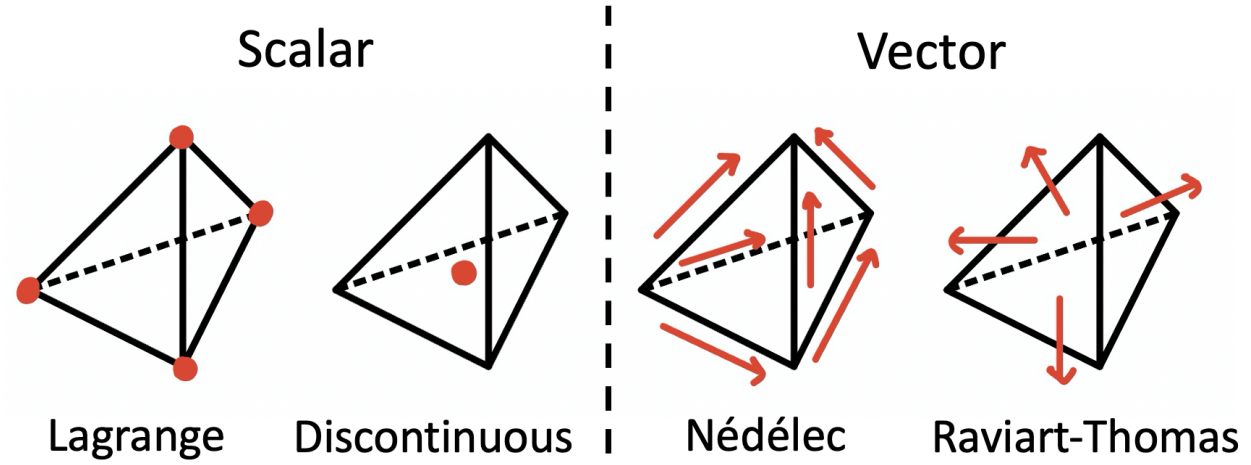

Figure 3.1: Illustration of the different types of finite-element basis space for both scalar, Lagrange and Discontinuous, and vector, Nédélec and Raviart-Thomas, solutions. The triangular prism represents an element and the red dot/vector represents the solution. Here it is seen that the vector basis spaces can only be either tangentially-continuous (Nédélec) or normally-continuous (Raviart-Thomas) while the Lagrange is fully continuous and conversely Discontinuous is as the name implies discontinuous.

to Raviart-Thomas, which loses accuracy in the solution. Another finite element issue that arises with the sheath BC is the fact that there is no continuity of the normal component of $\vec{D}$ along the boundary surface which leads to issues when taking the gradient tangentially [49].

In early stages of development Stix was written to be solved using Eq. 3.2 for $\vec{E}$ with the 2-step RF sheath iteration. Although 1D RF sheath problems were solved successfully, 2D sheath simulations lead to severe instability and noise due to the discontinuity in gradient of the sheath potential. Fig. 3.2 shows an example of this instability seen in the original electric field formulation of Stix. Here Figs. 3.2b, 3.2c, and 3.2d are the solution of the imaginary parallel electric field after 2, 4 and 6 global electric field iterations. One can see with increasing iteration, the solution grows with amplitude in particular the region between x = 1.0 and x = 1.2 m and that in the y direction there is a growing short wave oscillation in the field that does not exist in the true solution shown in Fig. 3.2a. For this reason, the novel decision to instead solve for the magnetic field, $\vec{H}$, was chosen. Rewriting Eq. 3.3 to be instead in terms of $\vec{H}$ allows for the plasma wave equation, Eq. 3.3, to be solved simultaneously with the full non-linear RF sheath BC, Eq. 3.4, thereby avoiding the need for calculating D_n explicitly.

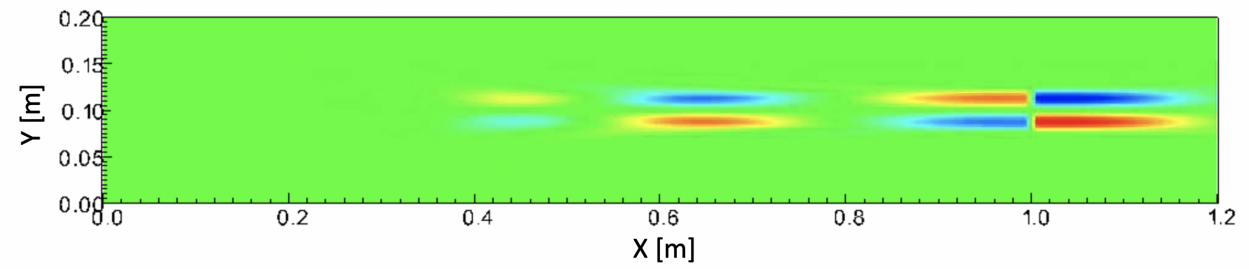

(a) True electric field solution using magnetic field formulation after 4 global magnetic field iterations.

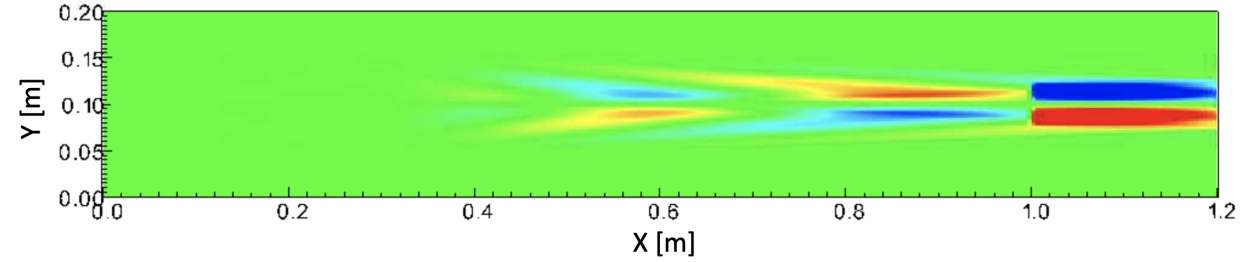

(b) Incorrect electric field solution using the electric field formulation after 2 global electric field iterations.

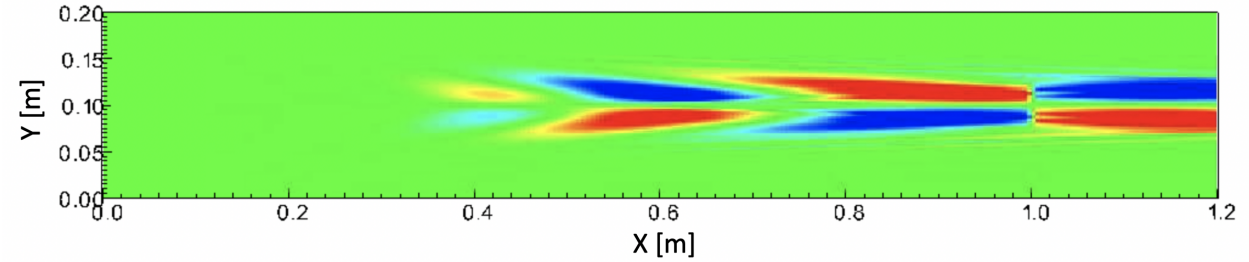

(c) Incorrect electric field solution using the electric field formulation after 4 global electric field iterations.

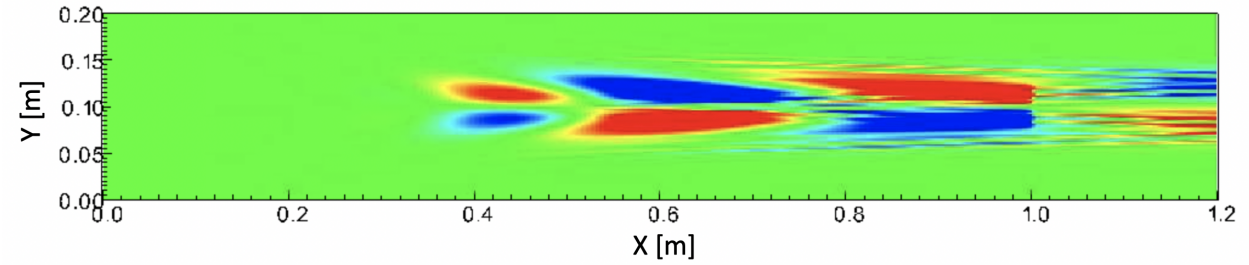

(d) Incorrect electric field solution using the electric field formulation after 6 global electric field iterations.

Figure 3.2: Normalized imaginary $E_{\|}$ for a 2D RF sheath case taken from [47]. a) shows the true solution using the $\vec{H}$ field solve, while the remaining electric fields shown are solved using Stix's original $\vec{E}$ field solve after b) 2 E-field iterations, c) 4 E-field iterations, and d) 6 E-field iterations. All plots are using the same minimum and maximum normalized $E_{\|}$ of -6.4 V/A to 6.4 V/A. It is seen that with every global electric field iteration, there is a growing instability in the solution that increases in amplitude and forms short oscillations in the y-direction for the electric field formulation of Stix.

3.4 The Finite-Element Discretization

The finite-element decomposition of Eq. 3.3, known as its weak-form, demonstrates how the RF sheath boundary condition organically fits into the H field formulation of the plasma wave equation. First one needs to decide what basis space to work with. Given that the plasma wave equation inherently has the curl operator within it, a natural choice is to use Nédélec. Using these Nédélec basis functions, here taken to be $\vec{W}_i$ and $\vec{W}_j$, the weak form of Eq. 3.3† is written as

$$\sum_j \left\{ \int_\Omega \left(\vec{\nabla} \times \vec{W}_i \right) \cdot \left(\bar{\bar{\varepsilon}}^{\,-1} \vec{\nabla} \times \vec{W}_j \right) d\Omega - \omega^2 \mu_0 \int_\Omega \vec{W}_i \cdot \vec{W}_j \, d\Omega + \int_{\partial\Omega} \vec{W}_i \cdot \left(\hat{n} \times \bar{\bar{\varepsilon}}^{\,-1} \vec{\nabla} \times \vec{W}_j \right) d\Gamma \right\} H_j = -i\omega \int_\Omega \vec{W}_i \cdot \left(\vec{\nabla} \times \bar{\bar{\varepsilon}}^{\,-1} \vec{J}_{\text{ext}} \right) d\Omega \tag{3.5}$$

"where the third term on the left-hand side is a Neumann BC on the magnetic field, $\vec{H}$. One can rewrite this boundary term using Ampere's Law to give the tangential electric field on the boundary, E_t. With a representation of E_t in the boundary term, the RF sheath BC, Eq. 3.4, is able to be directly incorporated into the plasma wave equation after V_{sh} is explicitly differentiated,"†. Additionally, since this boundary term represents E_t, ignoring this term would lead to what is known as natural BC which for this formulation equates to a conducting wall BC, i.e. $E_t = 0$.

Stix uses the MFEM library to construct the matrices needed to represent the terms in Eq. 3.5. Once this is finished, a global direct solve that integrates over the entire domain, Ω, using either SuperLU or MUMPS is completed. After $\vec{H}$ is obtained, to get the final electric field, Stix first needs to find the electric displacement, $\vec{D}$, using Ampere's Law: $-(\vec{\nabla} \times \vec{H} - \vec{J})/i\omega = \vec{D}$. From Table 3.2, it is seen that the curl of $\vec{H}$, where $\vec{H}$ is defined in Nédélec, is in the Raviart-Thomas (RT) basis space. Since $\vec{J}$ too is in RT, there is no basis transformation needed or global integration therefore $\vec{D}$ is easily calculated. The electric field is found as a last step by multiplying the electric displacement with the inverse dielectric using a basis transformation back to Nédélec basis functions following Eq. 3.6 using the iterative solver MINRES with a diagonal preconditioner.

$$\sum_j \left(\int_\Omega \bar{\bar{\varepsilon}}^{\,-1} \vec{F}_j \cdot \vec{W}_i \, d\Omega \right) \vec{D}_j = \sum_k \int_\Omega \left(\vec{W}_i \cdot \vec{W}_k \right) \vec{E}_k \, d\Omega \tag{3.6}$$

3.5 Verification of Cold Plasma Solve

As a first step of utilizing Stix for real physics problems, the verification of the global field solution using conducting wall boundary conditions was needed. A simple 1D test case of a propagating FW with an antenna placed in the middle of the domain and two conducting wall BCs on both ends, shown in Fig. 3.3, was chosen due to the existence of an analytic solution. The two measures of the code's success were chosen to be the value of the L^2 error of the total electric field versus the analytic solution and whether the L^2 error scaled with element refinement following the known convergence behavior of the finite-element method.

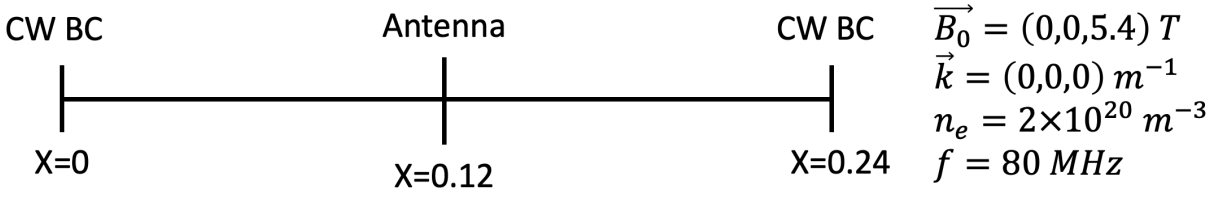

Figure 3.3: Schematic of the 1D domain of the propagating fast wave used for validating the global propagation solve of Stix. CW BC stands for a conducting wall boundary condition of $E_t = 0$.

The 1D analytic electric field solution for a launched fast wave is given by the polarization relation from Chapter 2, repeated here for reference as

$$\frac{E_x}{E_y} = \frac{iD}{S - N_{||}^2} \tag{3.7}$$

For simplicity $k_{||}$ is chosen to be 0 thereby making the polarization relation reduce to $E_x/E_y = iD/S$. This expression can be further collapsed by separating out the real and imaginary components of the electric field leaving the non-zero terms as: $ReE_x/ImE_y = -D/S$. Since Stix is a 3D code, a mesh with a domain following x $\gg$ y,z is used, where x spans from 0 to 0.24 m while y and z span from 0 to 0.01 m. Fig. 3.3 describes the setup of the problem along with the plasma parameters. The surface current on the antenna is arbitrarily chosen to be 1 A/m. There is no artificial collisionality in the plasma and therefore no damping of the wave.

Figure 3.4 shows that the electric field solution results in a standing wave. It is seen from Fig. 3.4 that the imaginary E_x and real E_y follow the exact same wave pattern but are scaled by a factor of $-D/S = 1.947$ and are 90° out of phase as predicted by the analytic polarization relation. To get a better reference of how close the computed electric field is to

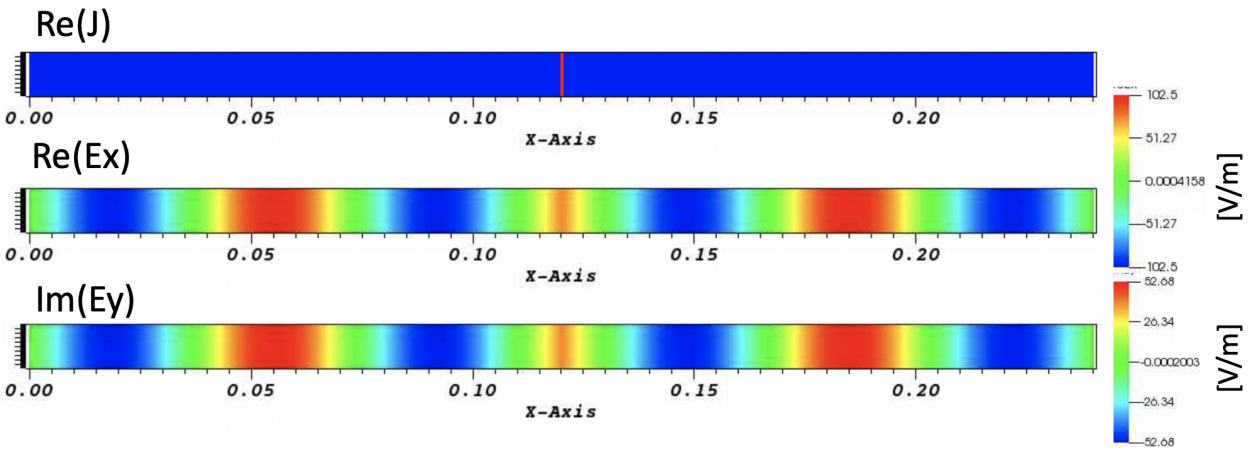

Figure 3.4: Pseudo-color plots of the real antenna current amplitude (top), the real x-component of the electric field (middle), and the imaginary y-component electric field (bottom) from the 1D FW global field verification case taken from Stix. It is seen that computed ReEx and ImEy are scaled by -D/S = 1.947 as predicted from the analytic polarization relation.

the true solution, the L^2 norm is chosen as an indicator of the global error defined as

$$\|\hat{x} - x\|_2 = \sqrt{\int_{-\infty}^{\infty} |\hat{x} - x|^2} \tag{3.8}$$

where $\hat{x}$ is the true solution and x is the computed solution of length k. For this case the L^2 error was 5×10^{-8} using order 2 polynomials giving good agreement between Stix and the analytic electric field solutions.

A more detailed indicator for the success of Stix's field solve involves looking at the L^2 norm convergence behavior. For the finite-element method the L^2 norm follows

$$p_U = \frac{\log\left(h_{n+1} - h_n\right) / \left(h_{n+2} - h_{n+1}\right)}{\log h_n / h_{n+1}} \tag{3.9}$$

where h is the the refinement level of the elements, i.e. 1/(number of elements) assuming uniform spacing, n indicates the number of refinements, and p_U is the order of the polynomial used [51].

Using the 1D test case of Fig. 3.3, the convergence behavior of Stix's L^2 norm with increasing number of elements for both order 1 and order 2 polynomials using the direct solver of MUMPS is shown in Fig. 3.5. Eq. 3.9 dictates that the scaling on a log-log plot, indicated by the b parameter, should follow the order of the polynomials used in the solve. Both Fig. 3.5a and 3.5b show that the measured scaling follows closely with the order of the

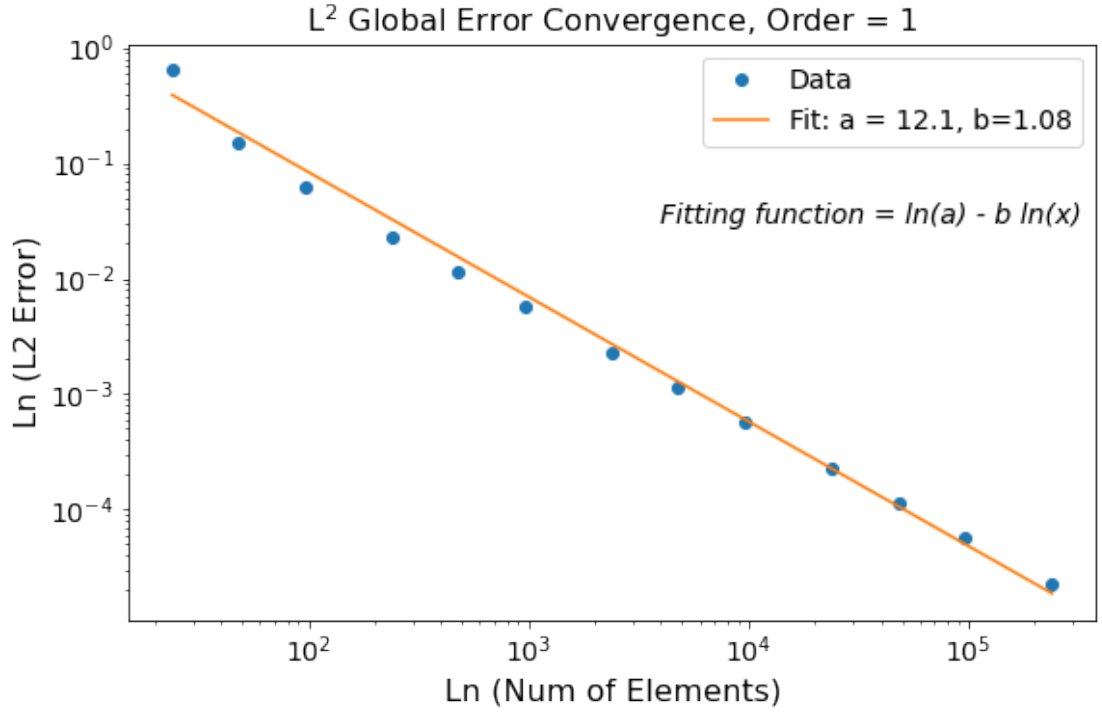

(a) L^2 norm scaling with more resolution using order 1 polynomial basis functions.

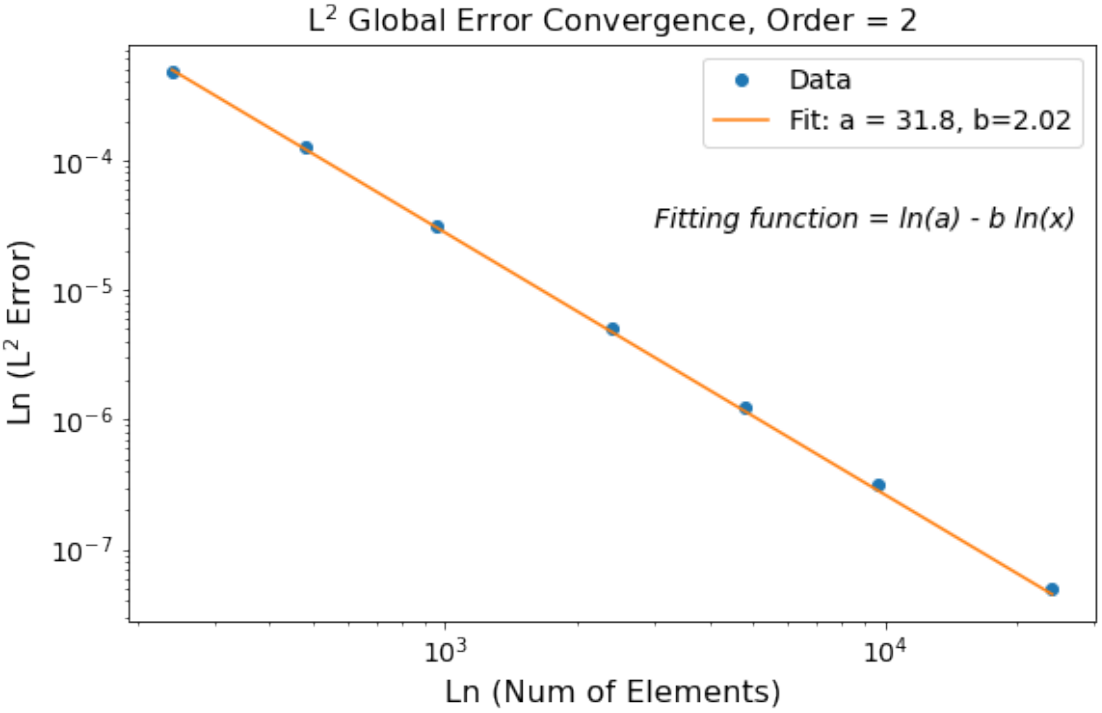

(b) L^2 norm scaling with more resolution using order 2 polynomial basis functions.

Figure 3.5: Convergence behavior of Stix for the 1D global propagation solve using a) order 1 and b) order 2 polynomials. With more element refinement, the scaling follows the order of the polynomial as indicated by the fitted b parameter.

polynomial giving confidence that Stix is behaving as expected numerically.

3.6 Development and Verification of RF Sheath BC

With confidence in the global wave solve using conducting wall boundary conditions, the next phase in development in Stix was the implementation of the full non-linear RF sheath BC given by Eq. 3.4.

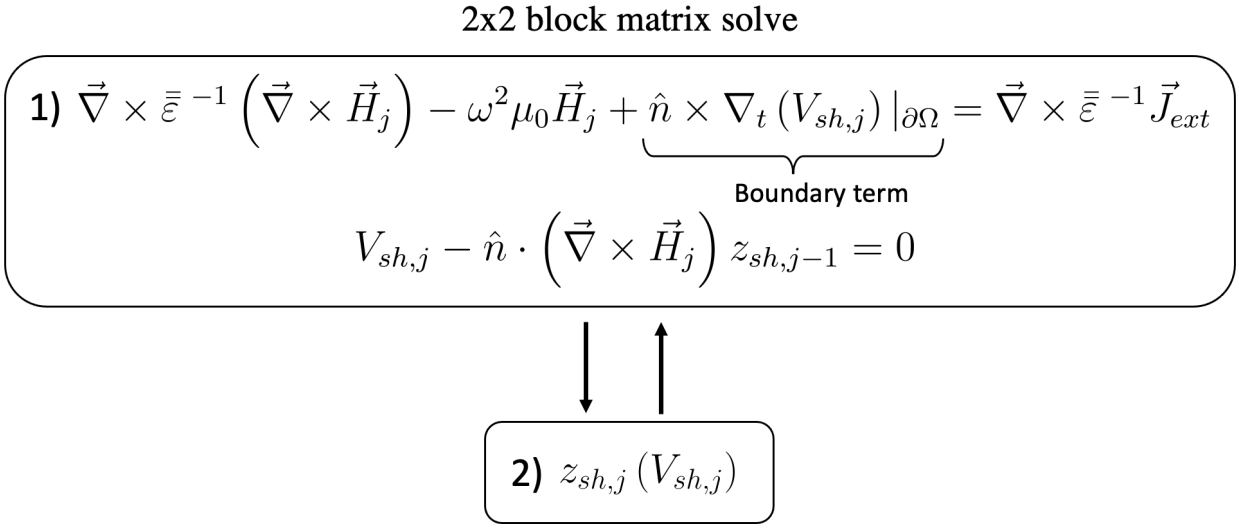

Figure 3.6: Workflow diagram of the Stix code describing the logic of the non-linear RF sheath solve. Here $j-1$ and j denote the iteration step. Step 1 solves for the plasma wave equation and the RF sheath BC concurrently for both $\vec{H}_j$ and $V_{sh,j}$. Step 2 updates the sheath impedance using J. Myra 2017 parameterization code [42] using the calculated $V_{sh,j}$. This new sheath impedance is updated on the boundary term of the plasma wave equation and the whole process repeats until the convergence criterion is satisfied.

As described in Section 3.4, Stix uses the novel method of solving for the $\vec{H}$ in both the H field plasma wave and the RF sheath BC equations. "This is done by using a 2×2 block matrix solve consisting of the wave equation block, the RF sheath potential block, and the off diagonal coupling blocks. The iterative solver GMRES calculates the Schur complement of the entire 2×2 system matrix in which the direct solver MUMPS (or SuperLU) is used to factor and solve the wave equation block. Once the $\vec{H}$ and the corresponding RF sheath potential, V_{sh}, are found, V_{sh} is passed into the parameterization code given by J. Myra 2017 [42] that in return gives a new sheath impedance value, z_{sh}. This new z_{sh} then updates the next iteration's V_{sh} which is differentiated and is used as the new boundary term in Eq. 3.4. With the new boundary term value, the whole $\vec{H}$ field is solved again over the entire domain reusing the MUMPS (or SuperLU) factorization of the wave equation block for efficiency.

The code does a fixed point iteration on V_{sh} until the desired convergence criterion of the errors between solves is met, usually taken to be $|V_{sh,j+1} - V_{sh,j}| \sim 10^{-5}$,"† [1]. Fig. 3.6 visualizes this solve in terms of its workflow.

Once the block matrix solve was implemented to include the full non-linear RF sheath BC, numerous sheath cases were tested to give confidence in the sheath solve. The most notable test cases, described in the next subsections, included a 1D case in which the plasma parameters and antenna current created a multiple root solution, a 2D propagating SW case, and a 2D case in which there was curvature on the sheath boundary wall where there was a rapid change in magnetic field angle.

3.6.1 1D - Multiple Roots Case

For a particular parameter space in antenna current amplitude and wave number, there can exist multiple root solutions for the RF sheath voltage as reported fully in [52] and earlier in [20], [25], [53], [54]. This process occurs when the RF wave's impedance matches the sheath's impedance known as sheath-plasma resonance [20], [25]. It can be thought of as the particular parameter space that allows for a LC circuit resonance in which the plasma's current is inductive into the sheath while the sheath's current response is capacitive [25]. Multiple root cases provide a good test of how RF sheath codes like Stix arrive at the possible stable/unstable solutions. As such, for testing Stix's non-linear iteration two 1D multi-root analytic cases were chosen from M. Poulos 2022 [52] that consisted of a bounded and unbounded case.

Unbounded Case

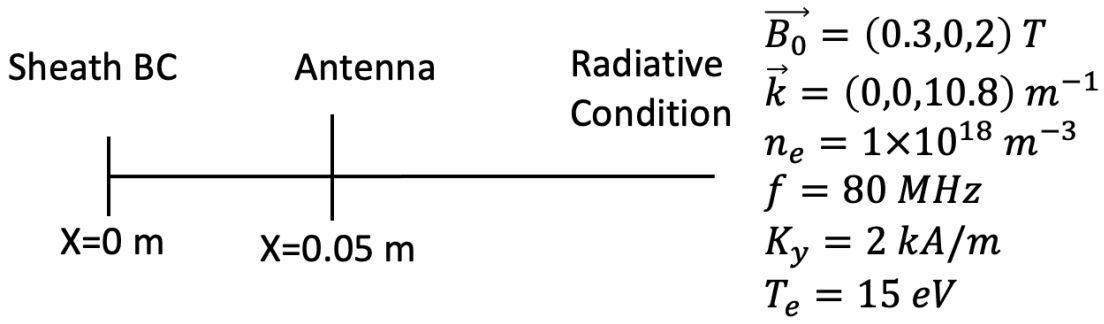

Figure 3.7: Diagram of the 1D unbounded sheath plasma wave case along with the plasma parameters described in [52].

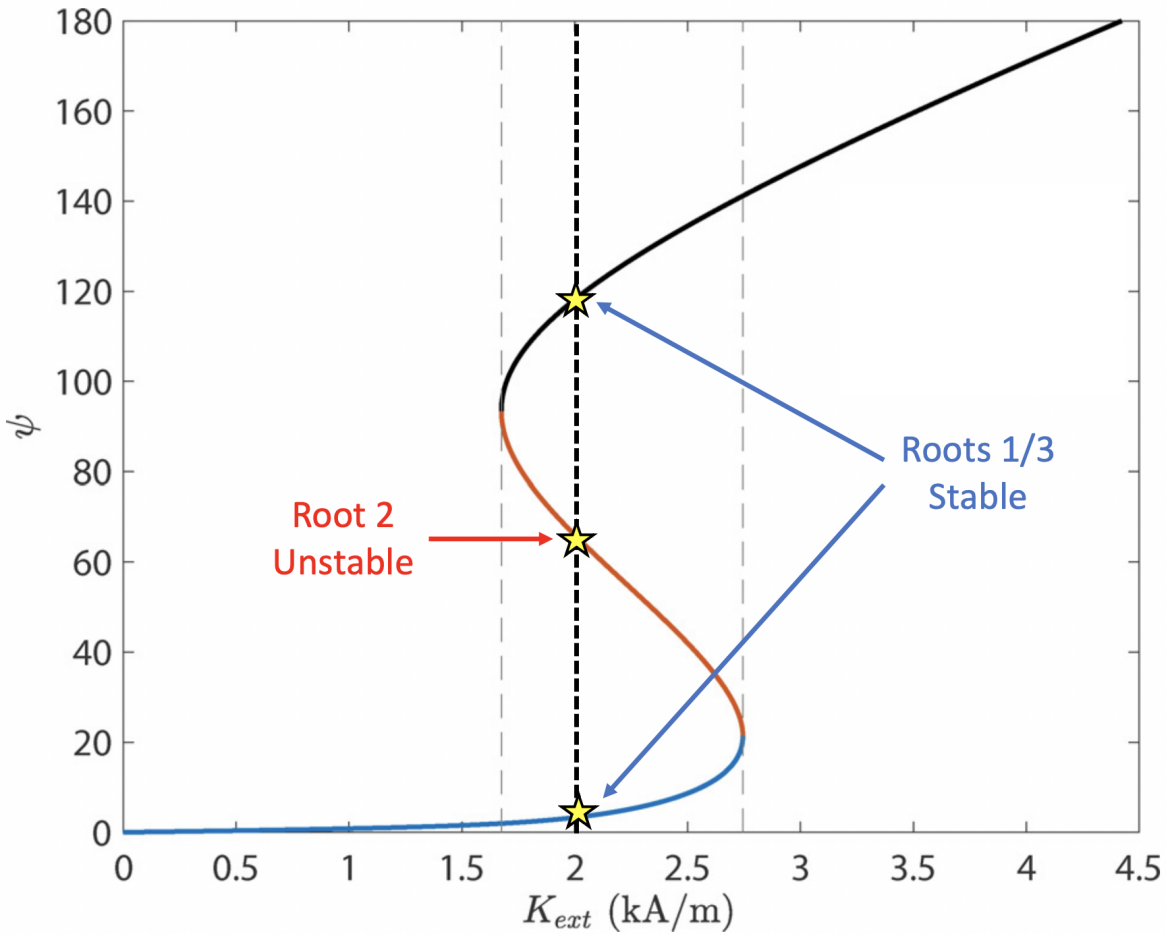

Figure 3.8: Figure taken with permission from [52] and adapted to display the multiple root solution for the unbounded case for varying antenna current amplitude. ψ is normalized to the electron temperature and is therefore unitless. Using 2 kA/m antenna current, indicated by the black dashed line, produces 3 RF potential solutions of which 1 is unstable as indicated by the red line.

Figure 3.7 describes the 1D setup of the unbounded case. The sheath BC is placed on the left at x = 0 m with an antenna current source 0.05 m away and the right hand side of the domain is set as a radiative condition meaning there is no reflections of the outgoing wave. For this case the wave is evanescent in the $\hat{x}$ direction and therefore the wave damps out completely before reaching the right hand side as long as the computational domain is long enough in the $\hat{x}$ direction. The plasma parameters can be found in Fig. 3.7.

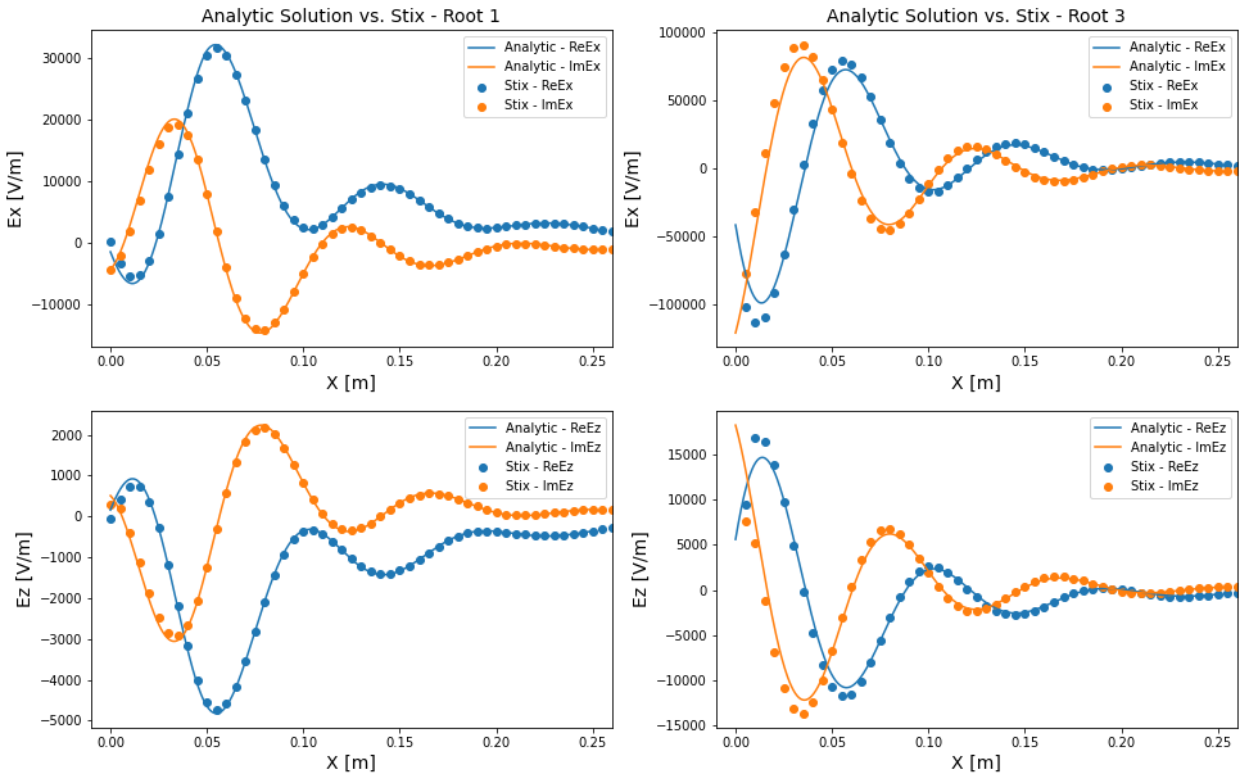

Figure 3.9: The comparison of the real (blue) and imaginary (orange) x and z components of the electric field for the unbounded multiple roots case from [52]. Left column shows the solution for the stable root 1 while the right column shows the solution for the stable root 3. The solid plotted lines are the analytic solution courtesy of M. Poulos. The over-plotted dots are taken from the Stix code showing good agreement with the analytic solution.

Solution	Stix $[e\,\lvert V_{sh}(0)\rvert\,/T_e]$	Analytic $[e\,\lvert V_{sh}(0)\rvert\,/T_e]$
1	3.25	3.3
3	118.0	118.1

Table 3.2: The comparison of the stable multiple root normalized RF sheath potentials for the 1D unbounded case of Stix vs the true analytic solutions taken from [52].

Shown in Fig. 3.8 is the analytic solution for this set of plasma parameters for varying antenna current amplitude. The derivation of the solution isn't included here but can be

found in M. Poulos 2022 [52]. For 2 kA/m, one can see there exist three RF sheath potential analytic solutions: 3.3, 66.1, 118.1 $e\left|V_{sh}\right|/T_e$. The red branch of Fig. 3.8 corresponds to the region that is unstable meaning that at least one eigenvalue in the matrix has a positive real component [52].

Using the 2 kA/m antenna current, Stix is able to successfully solve for solutions 1 and 3 using an appropriate corresponding initial guess. To get solution 1, an initial guess of a conducting wall BC is sufficient. For solution 3, an initial guess on the order of 10^2 $e\left|V_{sh}\right|/T_e$ input is needed, otherwise the code iterates to solution 1. The comparison of the computed normalized sheath voltages versus the analytic results can be found in Table 3.2. Additionally, the comparison of the real and imaginary E_x and E_z of Stix, shown by the points, versus the analytic solution, shown by the line, for both roots 1 and 3 is plotted in Fig. 3.9 and shows consistent agreement with one another.

Bounded Case

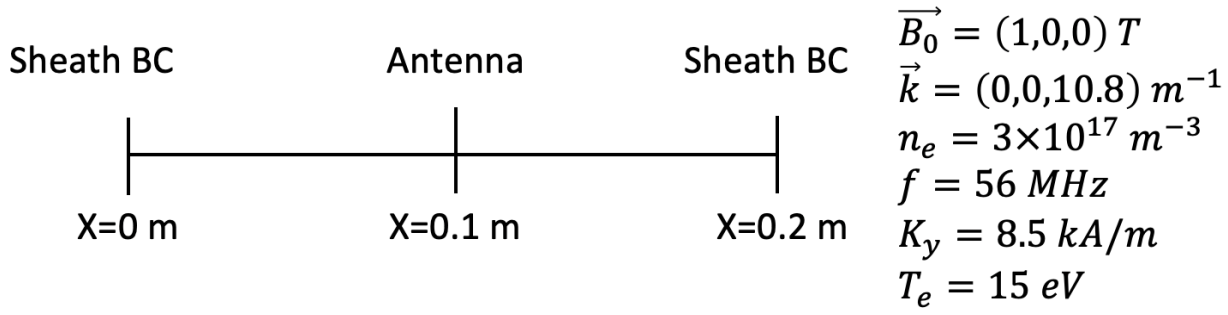

Figure 3.10: Diagram of the 1D bounded sheath plasma wave case along with the plasma parameters described in [52].

This 1D multiple root case consists of a bounded domain spanning from 0 to 0.2 m in the x direction with an antenna source placed in the middle. The domain setup along with the plasma parameters is shown in Fig. 3.10. Here the RF sheath boundary condition is placed on both ends of the domain. This case's analytic solutions for various antenna current amplitudes are plotted in Fig. 3.11 and show for an antenna current amplitude of 8.5 kA/m results in 5 RF sheath solutions of which 2 are unstable. Of the 5, solutions 2/4 and 3/5 are asymmetric inverses of one another while the first solution is symmetric.

Similar to the unbounded case, with fixed point iteration Stix can reach the roots using a comparable magnitude in the initial guess as the root solution. For the symmetric stable root 1, the code can reach it with a conducting wall initial guess. Interestingly for this case, Stix begins to converge on the unstable asymmetric root 2 before it ultimately converges on

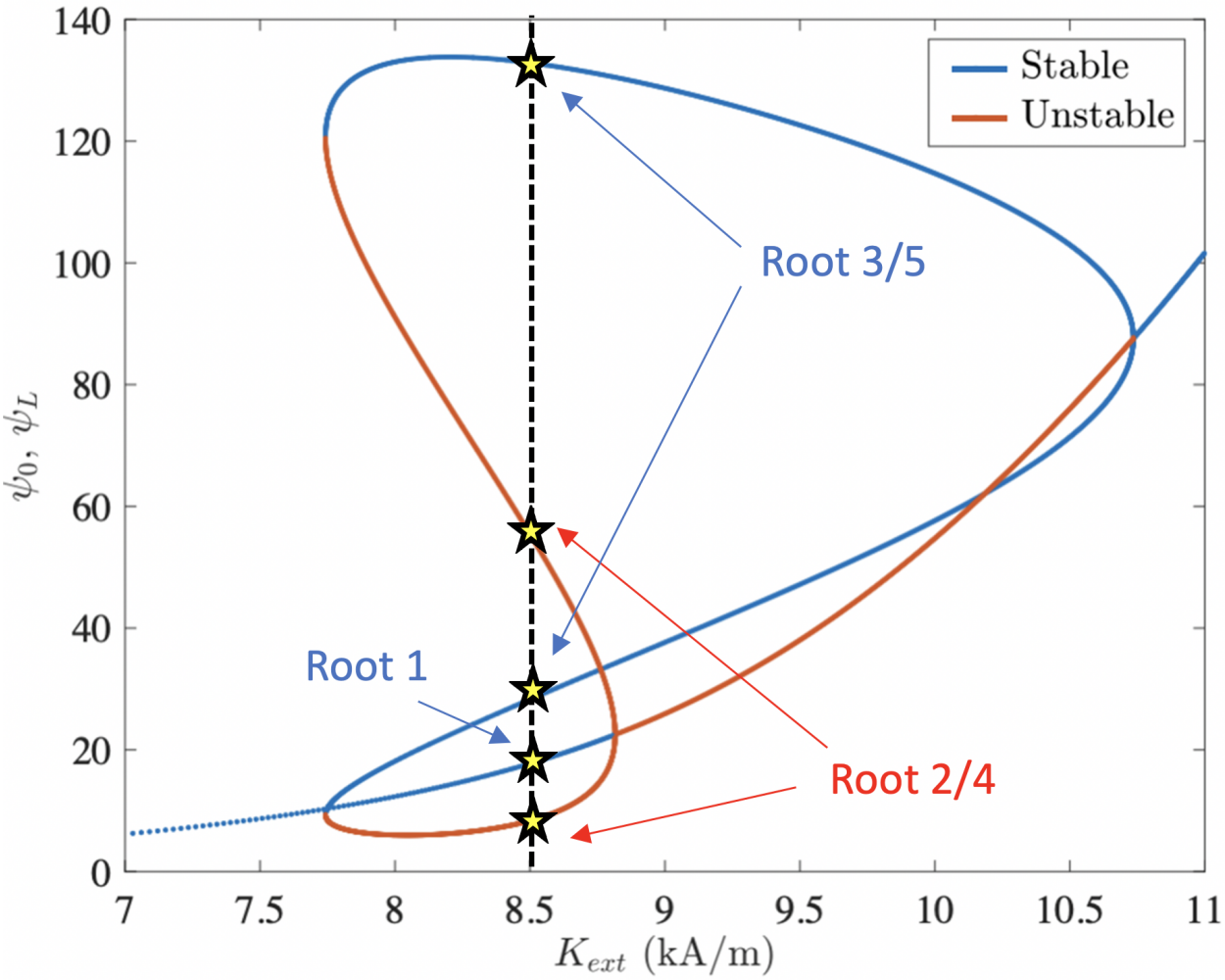

Figure 3.11: Figure taken with permission from [52] and adapted to display the multiple root solution for the bounded case. ψ is normalized to the electron temperature and is therefore unitless. Using an antenna amplitude of 8.5 kA/m indicated by the black dashed line shows 5 RF sheath potential solutions of which 2 are on the unstable branch shown in red.

Solution	Stix LHS $[e\,\lvert V_{sh}(0)\rvert\,/T_e]$	Stix RHS $[e\,\lvert V_{sh}(0.2)\rvert\,/T_e]$	Analytic LHS $[e\,\lvert V_{sh}(0)\rvert\,/T_e]$	Analytic RHS $[e\,\lvert V_{sh}(0.2)\rvert\,/T_e]$
1	17.67	17.67	17.7	17.7
2	8.68	54.54	8.3	55.5

Table 3.3: The comparison of 2 of the normalized multiple root solutions for the 1D bounded case of Stix versus the true analytic solutions taken from [52]. Here $V_{sh}(0)$ indicates the normalized RF potential solution at x=0 m domain boundary and $V_{sh}(0.2)$ represents the solution at the boundary x=0.2 m.

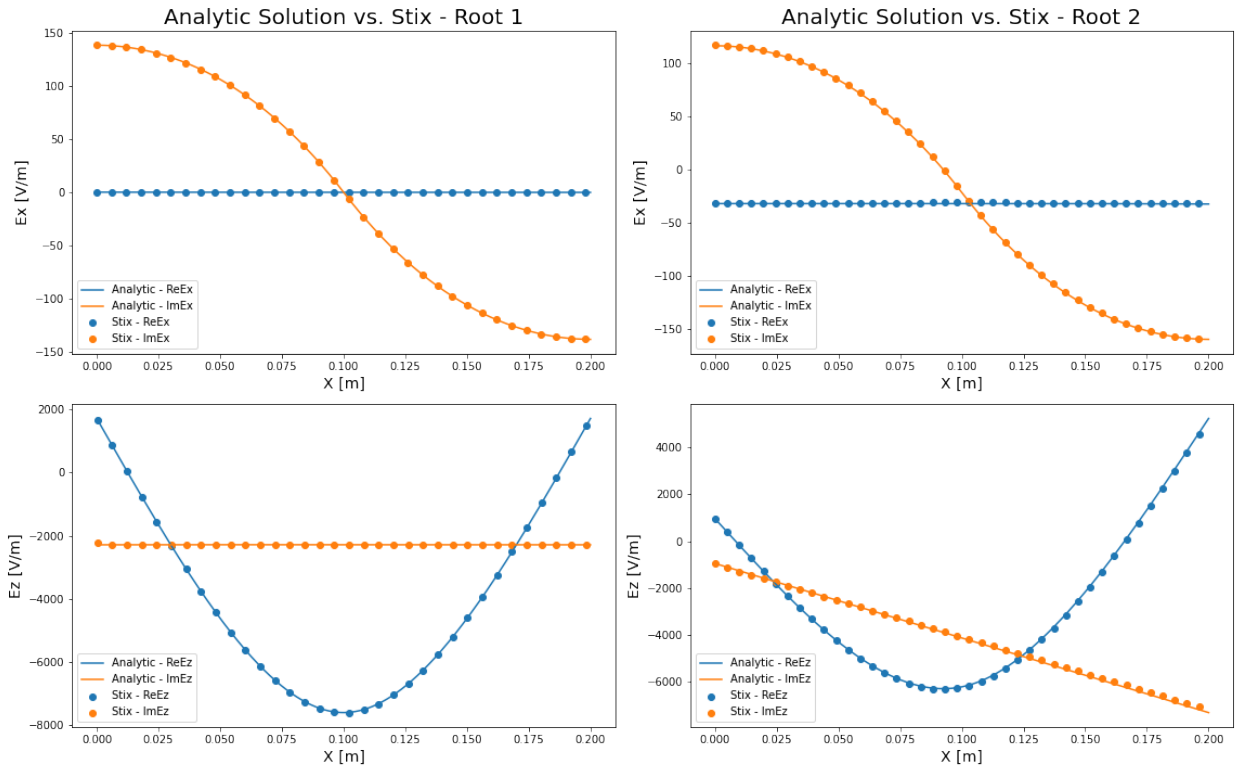

Figure 3.12: The comparison of the real (blue) and imaginary (orange) x and z components of the electric field for the bounded multiple roots case from [52]. Left column shows the solution for the stable root 1 while the right column shows the solution for the unstable root 2 which is the mirror of unstable root 4. The solid plotted lines are the analytic solution are courtesy of M. Poulos. The over-plotted dots are taken from the Stix code showing good agreement with the analytic solution.

the symmetric root 1 if an asymmetric initial guess on the RF potential is used. Here only 2 root solutions, roots 1 and 2, are chosen to compare against the analytic solutions. Table 3.3 reports the calculated normalized sheath voltages for both boundaries of x = 0 m and x = 0.2 m. The corresponding real and imaginary E_x and E_z for roots 1 and 2 are plotted in Fig. 3.12 and show agreement between the computed (points) and analytic (solid line) results.

3.6.2 2D - Propagating SW, Flat Wall

With confidence in the 1D RF sheath solves, a natural extension is to 2D problems. The following case was taken from Kohno et. al 2017 [47] who uses the RF code "rfSOL." This case represents a propagating slow wave. The x domain spans from 0 to 1.2 m while the y domain spans from 0 to 0.2 m with an antenna source centered at (1.0, 0.1) m of thickness 0.05 m in y and infinitely thin in x. The antenna is set up to follow a cosine squared profile, $J_{ext} = 10\cos^2\left(\frac{\pi}{0.05}\left(y - 0.1\right)\right)$, so that the current vanishes at both ends of the antenna. The RF sheath boundary condition is placed on the right hand side of the antenna at x = 1.2 m while the other 3 remaining walls are taken to be conducting wall boundaries. A phase factor in the z direction was taken to be $k_z = 320\ m^{-1}$ and an electron temperature of 15 eV was used for the RF BC. There is a constant background magnetic field of $\vec{B}_0 = (1, 0, 0)$ T and a constant density of $1 \times 10^{17}\ m^{-3}$. Lastly, to account for no reflections an artificially enhanced collisional profile of $\nu = 3 \times 10^{11}\mathrm{e}^{-x/0.1}$ was used with an effective electron mass. This case essentially equates to an unmagnetized problem given that the angle of the magnetic field is 90 degrees into the sheath boundary surface.

Comparing the imaginary parallel electric field normalized to the antenna surface current from the Stix code, Fig. 3.13b, and rfSOL code from Kohno et. al 2017, Fig. 3.13a, [47] shows good agreement between one another. This result is further bolstered by comparing the two code's line-outs of this field taken at y = 0.11 m and shown in Fig. 3.13c. The case of scanning various antenna current amplitudes from Fig. 7b was additionally run using Stix to test the non-linearity of the RF BC. The results from both codes are plotted in Fig. 3.14 where the orange stars represent Stix's computed maximum magnitude of the RF potential versus Kohno et. al 2017's data shown with blue crosses. The non-linearity of the trend in maximum RF potential can be seen in the range of the highest antenna amplitudes as demonstrated by the grey dashed linear reference in Fig. 3.14.

Lastly, it is worthwhile addressing a challenge of replicating this benchmark. This pertained to including enough resolution through the number of elements to capture the amplitude of the wave. A common metric to use is 10 elements per λ, however as demonstrated

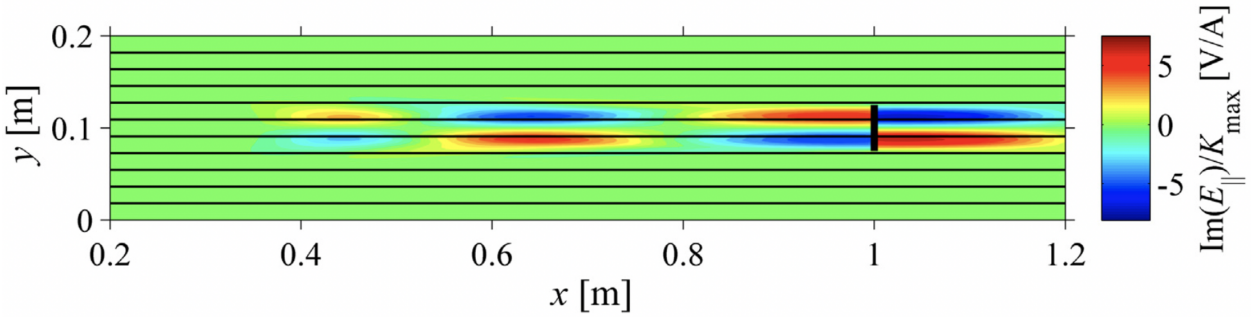

(a) Pseudo-color plot of the normalized imaginary parallel electric field from Fig. 6 of Kohno et. al 2017 with the background magnetic field overlaid in black, reproduced with permission from [47].

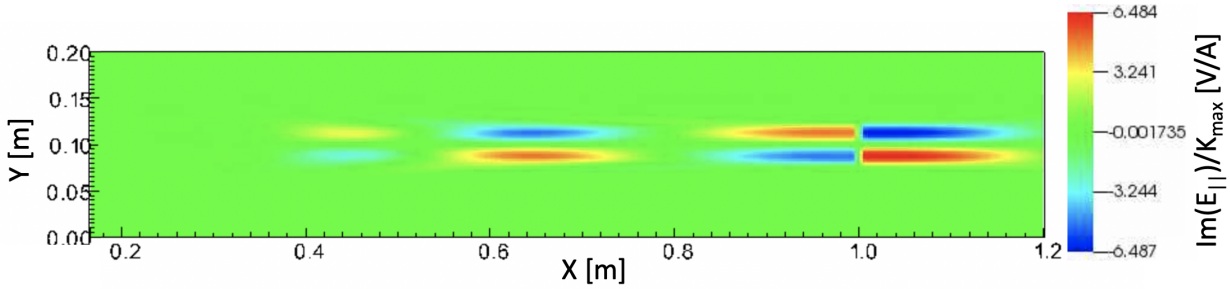

(b) Pseudo-color plot of the normalized imaginary parallel electric field from the Stix code, reproduced with permission from [1].

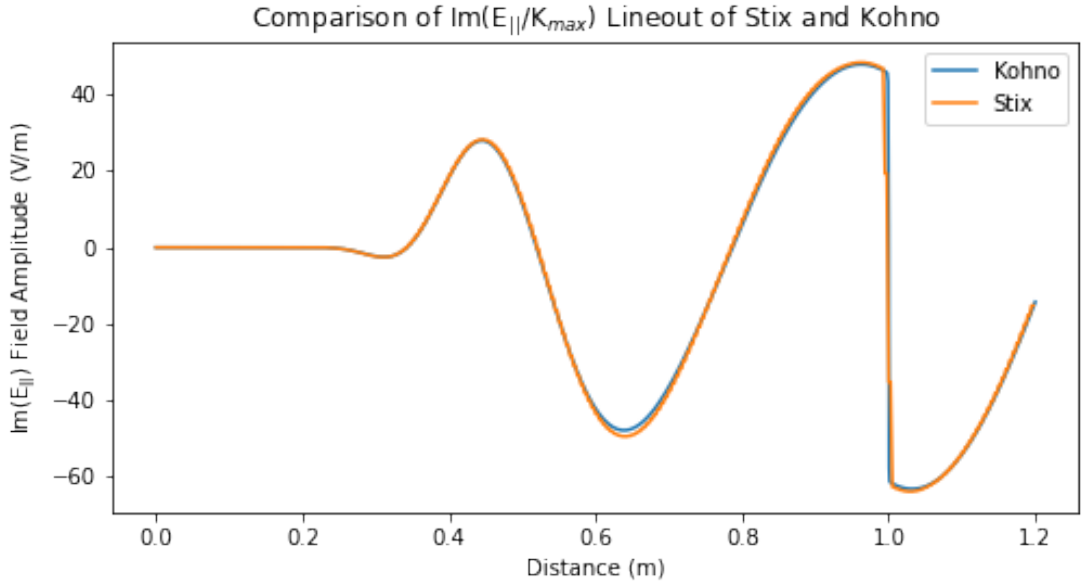

(c) Normalized imaginary electric field lineout taken at y = 0.11 m spanning from x = 0 to 1.2 m comparing the Stix code (orange) to Kohno et. al 2017 [47] (blue), reproduced with permission from [1].

Figure 3.13: RF sheath 2D validation propagating slow wave case taken from Kohno et. al 2017 [47]. Comparison between the rSOL data in a) and the Stix data in b) shows good agreement between the codes further bolstered by over-plotting the electric field solution of the two codes plotted in c).

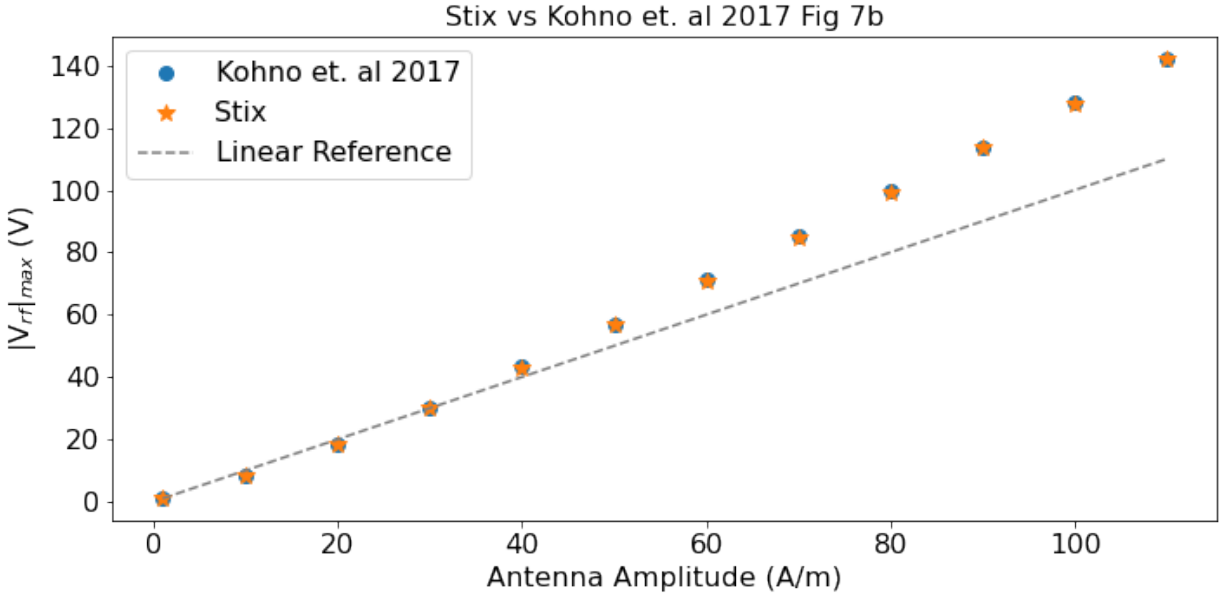

Figure 3.14: Comparison of scanning antenna amplitudes versus maximum magnitude of RF sheath potential comparison between Stix (orange) and Fig 7b of Kohno et. al 2017 (blue) [47]. The grey dashed line is a linear reference that serves to show the non-linearity of the sheath voltages at higher antenna amplitudes.

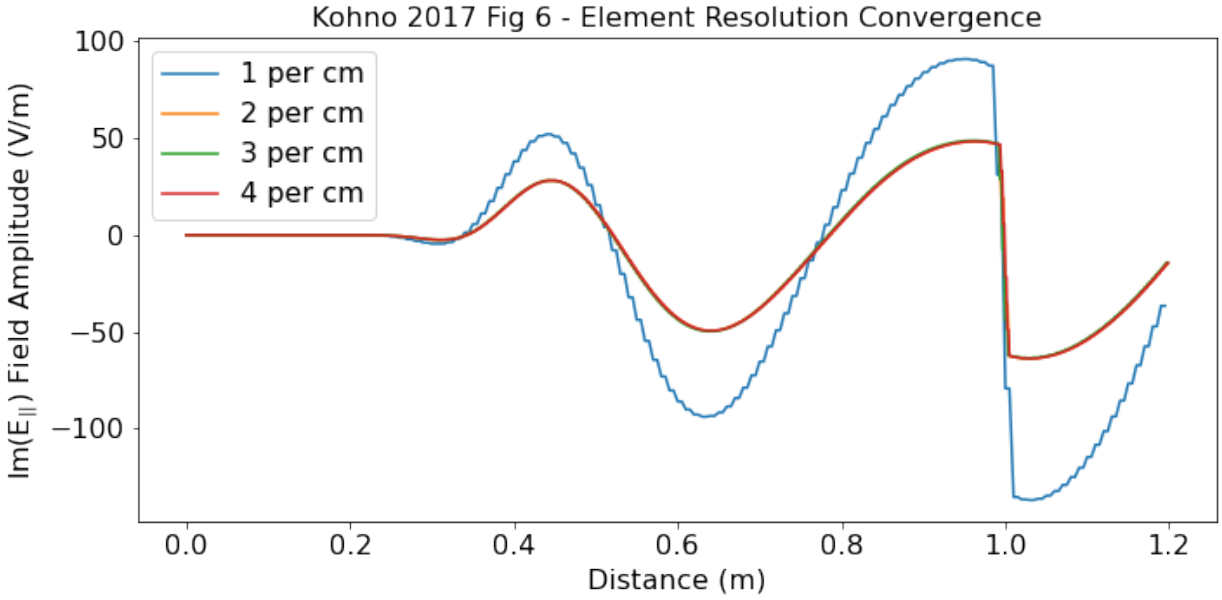

Figure 3.15: Plot of the imaginary parallel electric field using varying amounts of elements in the x direction demonstrating the necessary amount of elements to reach the solution. 1, 2, 3, and 4 per cm lines correspond to 1, 2, 3, and 4 elements per cm. It is seen that with 1 element per cm (88 elements per λ) is not enough resolution to reach the converged electric field solution.

by Fig. 3.15, this case needed a significant amount more elements per λ. Fig. 3.15 shows the comparison of the imaginary electric field taken at y = 0.11 for various amounts of elements in the x-direction spanning from 1 to 4 elements per cm. This case corresponds to a wave with a 88 cm wavelength meaning that 88 elements per λ was not enough to resolve the electric field as shown by Fig. 3.15. Only using 176+ elements per λ was enough to resolve the field. This result is most likely due to this case corresponding to using an infinitely thin antenna source which requires a jump condition at the antenna. The antenna source in Stix is set as a volumetric current density with a finite thickness. Therefore making the current sheet as thin as possible as to not introduce an additional phase shift but having enough elements to capture the discontinuity in the electric field solution within the current sheet width was a difficulty.

3.6.3 2D - Propagating SW, Curved Wall

The last verification case discussed is taken from Kohno et. al 2019 [53] using again the code rfSOL in which a propagating SW is impinging on a curved surface that has the RF sheath BC. Here there is an added effect of a rapidly changing magnetic field angle which is known to influence RF sheath rectification [42]. The domain spans from 0 to 6 m in x and 0 to 0.8 m in y. The curved surface at x = 6 m follows the parameterization of $h_{\text{sh}}(y) = h_{\text{bump}} \exp\left[-\frac{(y-L_y/2)^2}{w_{\text{bump}}^2}\right]$, where $h_{\text{bump}} = 0.4$ m, $w_{\text{bump}} = 0.1$ m, and L_y is 0.8 m [53]. There is both a uniform magnetic field solely in the x direction of 4 T and density of 1×10^{17} m^{-3}. The k_z value was taken to be 160 m^{-1}, a frequency of 80 MHz, and temperature of 15 eV were used as well as an artificial collisional profile of $\nu = 3 \times 10^{11}$ s^{-1} to ensure there are no reflections from the left hand side. The antenna current follows the same profile as in the 2D flat wall case above using an amplitude of 6 kA/m.

It is seen from Fig. 3.16a and Fig. 3.16b that Stix's real parallel electric field normalized to the antenna surface current follows rfSOL's field closely. As a further check that the RF sheath voltages are consistent, Stix's values are plotted against those from rfSOL along the y direction of the sheath boundary surface shown in Fig. 3.16c and are shown to agree closely.

3.7 Optimization of the RF Sheath BC: The MPE Method

From the previous section it is shown that the fixed-point iteration technique implemented in Stix computes the expected RF voltages. However one disadvantage of this method is that the number of global field iterations needed to reach a converged solution can be substantial, on the order of ~ 20, depending on the case. For large computational problems this poses a

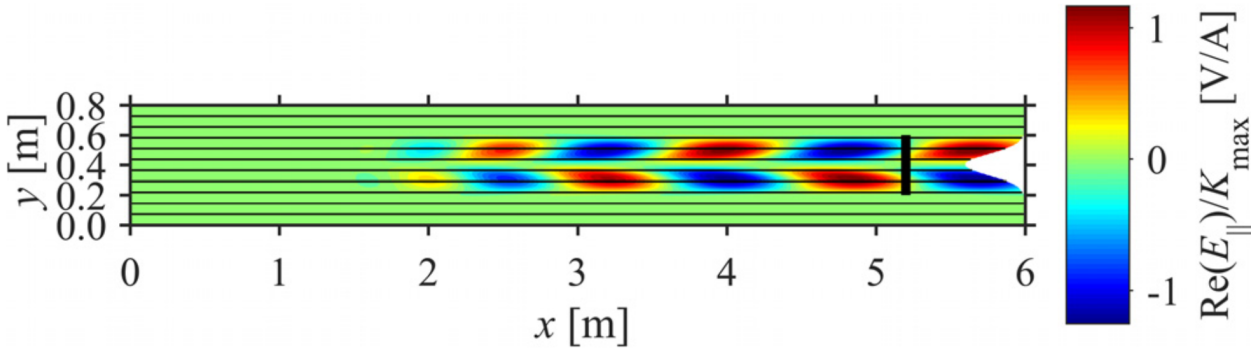

(a) Pseudo-color plot of the normalized real parallel electric field from Fig. 11 of Kohno et. al 2019 with the background magnetic field overlaid in black, reproduced with permission from [53].

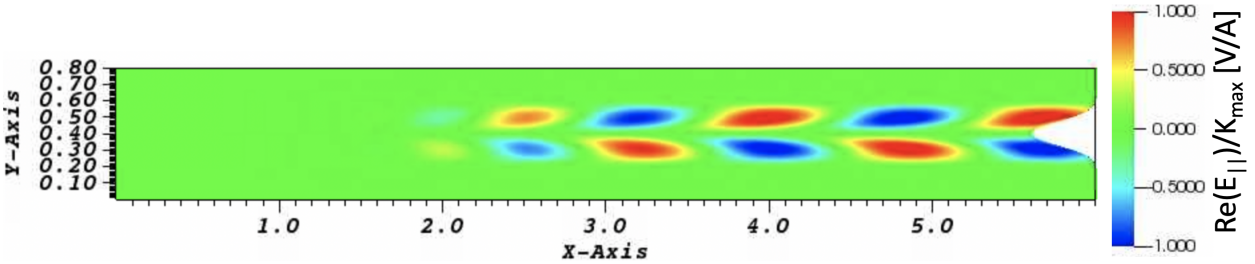

(b) Pseudo-color plot of the normalized real parallel electric field from the Stix code.

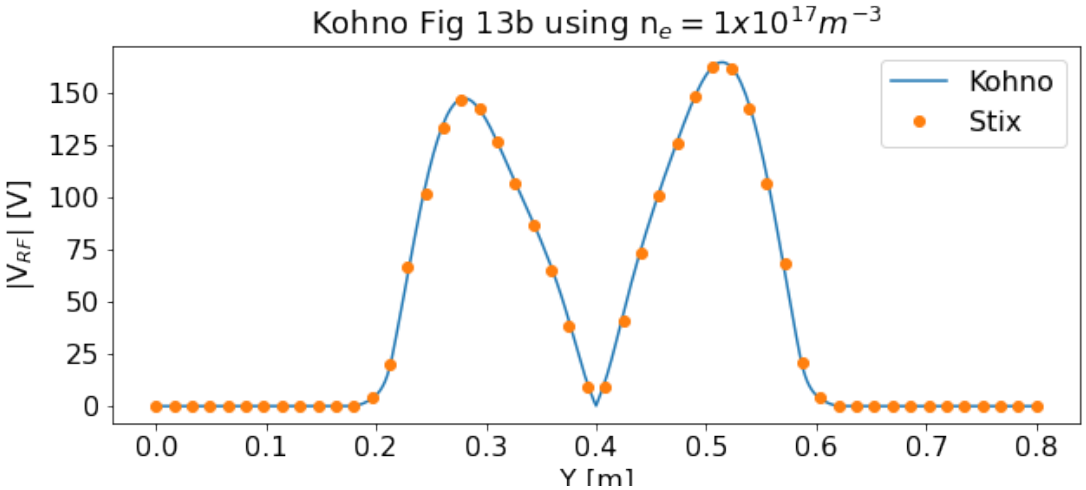

(c) Comparison of $|V_{RF}|$ along x=6.0 m curve boundary wall from Stix (orange dots) to Fig. 13b of Kohno et. al 2019 (solid blue line), reproduced with permission from [53].

Figure 3.16: Comparison of 2D RF sheath validation case of a propagating slow wave impinging on a curve surface taken from Fig. 11 from Kohno et. al 2019 [53]. The electric field from Kohno et. al 2019 [53] in a) and the electric field from Stix b) give good agreement with one another. This result is further supported by comparing the magnitude of the RF sheath potential along the curved domain boundary plotted in c).

problem with efficiency of the code. This section discusses a technique used to optimize the non-linear solve of the RF sheath potential, V_{sh}, that replaces the fixed point iteration. Here the method of "minimal polynomial extrapolation" otherwise known as "MPE" is introduced and the algorithm logistics described in Table are discussed.

One can first show that the non-linear expression of the RF sheath potential

$$V_{sh} = -i\omega D_n z_{sh}(V_{sh}) \tag{3.10}$$

behaves linearly near its solution, i.e. where $V_{sh} = s$. This linear behavior of Eq. 3.10 near the solution allows one to use vector extrapolation methods that use linear systems for their derivatives. For this BC, the vector extrapolation method of MPE was chosen. The idea behind MPE is to get the solution, $\vec{s}$, as a weighted average of the $\vec{V}_{sh,n}$ where the weights are determined by the coefficients of the minimal polynomial, P(λ), of matrix, A, with respect to $\left(\vec{V}_{sh,1} - \vec{V}_{sh,0}\right) = \vec{u}_0$. The derivation below follows Sidi 2008 [55] and Smith et al. 1987 [56].

First, assume there is a linear system given by

$$V_{sh,n+1} = AV_{sh,n} + b \text{ for } n = 0, 1, 2 \cdots \tag{3.11}$$

where $\vec{V}_{sh,n}$, b $\in C^N$ and A $\in C^{N\times N}$. In order for their to be an unique solution, $\vec{s}$, one must assume $(I - A)$ is non-singular, meaning there exists no eigenvalues that equal 1. For simplicity, one can introduce the term, $\vec{u}_j$ as

$$\vec{u}_j = \Delta\vec{V}_{sh,j} = \vec{V}_{sh,j+1} - \vec{V}_{sh,j} \tag{3.12}$$

Now take at the moment an arbitrary fixed integer as k that follows $k \leq N$. Next, one can define a matrix of $N \times k$ in which the columns are composed of the vectors of the differences, i.e.

$$U \equiv [\vec{u}_0, \vec{u}_1, \cdots, \vec{u}_{k-1}] \tag{3.13}$$

One can invoke the definition of the monic polynomial $P(\lambda)$ given as

$$P(\lambda) = \sum_{j=0}^{k} c_j \lambda^j \;\rightarrow\; P(A) = \sum_{j=0}^{k} c_j A^j \tag{3.14}$$

where $c_k = 1$ being the minimal polynomial of matrix A with respect to $\vec{u}_0$ if,

$$P(A)\vec{u}_0 = 0 \tag{3.15}$$

and $P(\lambda)$ having the smallest degree. Note that,

$$\vec{u}_{j+1} = A * \vec{u}_j = A^{j+1} * \vec{u}_0 \tag{3.16}$$

Combing Eqs. 3.16 and 3.14 gives

$$P(A)\vec{u}_0 = \sum_{j=0}^{k} c_j A^j \vec{u}_0 = \sum_{j=0}^{k} c_j \vec{u}_j = 0 \tag{3.17}$$

Expanding Eq. 3.17 gives an expression for the coefficients, $\vec{c}$, with respect to the vector differences as

$$c_0\vec{u}_0 + \cdots + c_{k-1}\vec{u}_{k-1} = -c_k\vec{u}_k = -\vec{u}_k \tag{3.18}$$

The above expression can now be rewritten using Eq. 3.13 as

$$U * \vec{c} = -\vec{u}_k \tag{3.19}$$

Now $\vec{c}$ can be found using the Moore-Penrose generalized inverse: $U^+ = (U^*U)^{-1}U^*$ [55]. The simplest way to do this is by taking $\vec{c}$ as the least-squares solution to Eq. 3.19, i.e.

$$\min_{c_0,c_1,\ldots,c_{k-1}} \left\| \sum_{j=0}^{k-1} c_j u_j + u_k \right\| \tag{3.20}$$

The last step requires the use of the theorem stating if $P(\lambda)$ and $Q(\lambda)$ are the minimal polynomials of A with respect to vectors $\vec{u_0}$ and $(\vec{x}_0 - \vec{s})$ respectively then $P(\lambda) \equiv Q(\lambda)$. Now one can get an expression that relates $\vec{\phi_j}$, $\vec{c}$, and the solution, $\vec{s}$ as

$$\sum_{j=0}^{k} c_j A^j \left(\vec{\phi}_0 - \vec{s}\right) = \sum_{j=0}^{k} c_j \left(\vec{\phi}_j - \vec{s}\right) = 0 \;\rightarrow\; \sum_{n=0}^{k} c_j \vec{\phi}_j = \left(\sum_{j=0}^{k} c_j\right) \vec{s} \tag{3.21}$$

Here $\vec{s}$ represents the optimized solution for the RF sheath potential.

The MPE algorithm is summarized in Table 3.4. With this new numerical method incorporated into Stix, there were two 1D test cases chosen to see its efficiency: the unbounded multiple roots case from Section 3.6.1, shown in Fig. 3.7, as case 1 and the simple 1D propagating FW case from Section 3.5, shown in Fig. 3.3, as case 2 but with RF sheath BCs placed on both ends. Fig. 3.17 shows the resulting convergence of the RF sheath potential versus the iteration number for various k values. The convergence criterion of RF sheath iteration for both cases is user specified, in this case chosen to be $|V_{sh,n+1} - V_{sh,n}| < 10^{-5}$. This reduction in the number of global iterations demonstrated in Fig. 3.17 shows promising

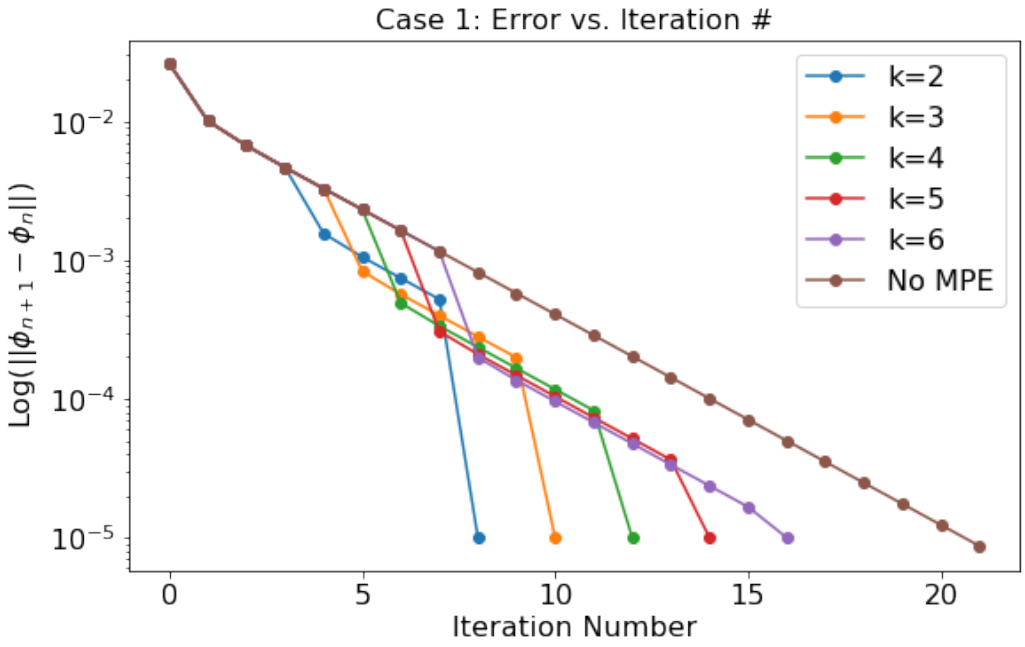

(a) Case 1: The relative error versus the iteration number for unbounded multiple roots described in Section 3.6.1.

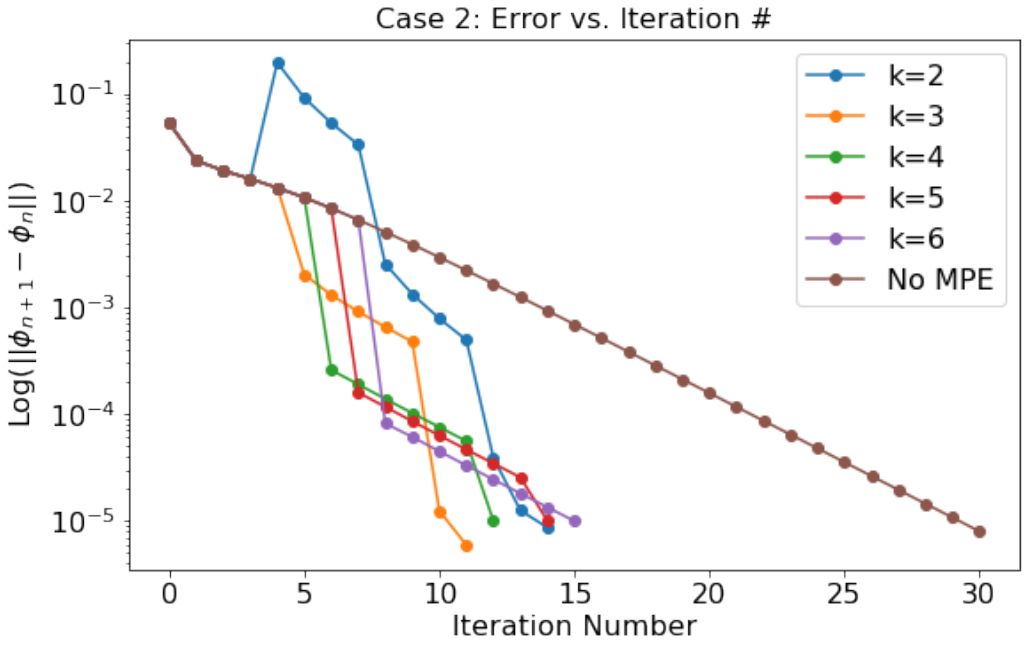

(b) Case 2: The relative error versus the iteration number for 1D global field solve with RF BCs placed on both ends described in Section 3.5.

Figure 3.17: Log error difference of the RF sheath potential between iterations: n+1 and n versus the number of iterations it took to reach below set threshold of 10^{-5}. The brown line indicates the fixed point iteration solution which took the longest to convergence in both cases.

Minimal Polynomial Extrapolation (MPE) Algorithm
Choose an integer value for k
1) Use $\vec{V_{sh,0}}$ as initial condition
2) Find $\vec{V_{sh,1}}, \vec{V_{sh,2}}, \cdots, \vec{V}_{sh,k+1}$ using Eq. 3.10
3) Calculate $\vec{u_k}$ and U using Eqs. 3.12 and 3.13
4) Compute the coefficients $\vec{c}$ using Eq. 3.20
5) Calculate $\vec{s}$ using Eq. 3.21
return $\vec{s}$

Table 3.4: The MPE algorithm steps used for optimizing the fixed-point iteration implemented in Stix.

results for optimizing Stix's original non-linear solve.

It should be noted that the route of using a small 1D cases was chosen intentionally on the basis of easy testing. Both cases 1 and 2, only have 100 elements in each mesh with no refinements and used linear polynomials, making the number of unknowns $\sim 10^3$. In more realistic geometric cases that either are of the tokamak's poloidal cross section or a cut of the launched antenna structure, the mesh sizes become increasingly refined with a significant amount of elements. Because with each iteration, the wave equation needs to be solved on the entire mesh cutting down on the number of iterations is key. The fact that the number of iterations using the MPE method regardless of the choice of k was less the original fixed-point algorithm shows that this method would be advantageous to continue to use and optimize.

Chapter 4

Comparison Modeling: Near-Field Sheath Behavior on Alcator C-Mod

In this chapter, the Stix code is used to replicate in 2D an antenna strap power phasing experiment done on the Alcator C-Mod tokamak for insight into near-field sheath behavior [2]. The primary motivation for choosing this experimental study was that there are direct measurements of the enhanced potential proxy and impurities in the plasma both near and far from the antenna [33], [34], [57]. Similarly, the data for both the potentials and impurities show a clear minimization trend with respect to antenna phasing power fraction, described further in Section 4.2, that serves as valuable validation for simulation.

With confidence in the RF sheath BC implementation described in Chapter 3, moving to a realistic tokamak geometry scenario was the next step for Stix. As such, the first aim of this study was to see whether the experimental trend can be reproduced numerically and to observe the differences between computational and experimental data. Additionally, given the limited realistic antenna geometric simulations done with the full non-linear RF sheath BC, described in Section 4.1, another objective was to see whether there are any near-field sheath insights that could be extracted when the RF sheath is represented versus when the common conducting wall BC is used. Likewise, these simulations aimed to look at various antenna phasing schemes to further study antenna operation optimization. Lastly, with knowledge of the DC rectified potentials on the walls the resulting sputtering yield can be inferred and consequently the erosion rate of the wall material due to it. Similarly, one can compare its trend over the power phasing fractions to that found experimentally in the C-Mod campaign.

4.1 Previous Numerical Studies of Near-Field Sheaths

There have been numerous computational studies centered around understanding and mitigating the formation of RF near-field sheaths. Earlier work has used finite-element electromagnetic wave solvers to model the complex antenna geometry using conducting wall boundary conditions that do not represent the RF sheath to look at the electric fields generated on the structures such as TOPICA [58], RAPLICASOL [59], [60], and Petra-M [48]. With the introduction of the J. Myra et. al 2015 RF sheath BC [16], EM codes like Petra-M [49], VSim [61], SSWICH [45], rfSOL [47], and COMSOL [60] now have incorporated some version of a RF sheath BC as described in Chapter 3. Of the five codes, rfSOL and the time domain RF solver VSim are the only ones to include the full non-linear form of the RF sheath BC.

Most recently, numerical simulations of ICRF antennas have progressed to modeling the full 3D structure of the antennas, ones of particular note are the WEST [49], [62] and SPARC [63] antennas. The WEST antenna was simulated by both Petra-M [49] and COMSOL [62] using an asymptotic limit of the RF sheath BC and it was found that there were regions along the RF limiters with enhanced potentials exceeding 200 V. Additionally, Petra-M showed that there was significant poloidal variation along the limiter implying the importance of including geometric effects [49]. Conversely, the SPARC antenna using VSim did show that there was formation of localized sheath potentials along the inner RF limiters and Faraday screens, but the values were much lower than those of WEST, of order ~ 50 V [63]. Similar work done in 2D of the JET antenna using SSWICH has shown the drastic variation of the rectified potential poloidally as seen with the Petra-M WEST simulation [21], [49]. These latest investigations which include a form of the RF sheath show the complexity in the behavior of RF sheaths given the variation in voltages and field patterns found on the various ICRF antennas. Consequently, using these numerical tools are an essential process of ICRF antenna operation and design optimization.

4.2 The C-Mod Power-Phasing Experiment

Much of the focus of reducing near-field RF sheath effects has been to optimize the ICRF antenna design and operation as discussed in Chapter 1. The main objective of these efforts has been to minimize the parallel electric fields, $E_{\parallel}$, on the antenna and the nearby structures due to the dependence of the RF sheath on $E_{\parallel}$ [21].

"In the pursuit of decreasing tungsten (W) impurities during ICRF heating, the AUG team investigated methods of optimizing their 2-strap antenna to reduce the $E_{\parallel}$ on the

antenna limiters that included reducing RF image currents [13]. This discovery led to a new design of a 3-strap antenna that did see a reduction of W impurity generation [35]. Using this antenna on AUG a straps phasing of $0/\pi/0$, a power-phasing study was done in which the fraction of power of the central strap (P_{in} relative to the outer straps (P_{tot}) was varied to see if there is an ideal operating scenario [32]. On both sides of the RF limiters, the RF potential (V_{RF}), the DC current (I_{DC}), and the tungsten sputtering yield (Y_W) were measured in several poloidal locations [32], [35]. It was found that there were variations in the local minima of V_{RF} in power-balance and phasing space on both sides of the limiters [32]. The overall trend indicated a minimum of both V_{RF} and Y_W between $P_{in}/P_{tot} \sim 0.55 - 0.7$ with the ideal fraction at $P_{in}/P_{tot} \sim 0.67$ [21], [32]."‡

"Following AUG's $E_{\|}$ minimization efforts via image current cancellation, experiments were run on Alcator C-Mod's field aligned 4-strap ICRF antenna using the same power phasing method with $0/\pi/0/\pi$ current strap phasing for both $P_{ICRF} = 1$ and 1.5 MW. Although the C-Mod antenna geometry and SOL density are different, the trends of minimization measured in C-Mod were similar to that of AUG. Using gas-puff imaging (GPI) measuring the upper outer corner of the antenna"‡ in addition to a magnetically connected Langmuir probe in the upper divertor "showed that enhanced potentials were at a minimum between $P_{in}/P_{tot} \sim 0.7 - 0.9$ [21], [32], [33]. In the case of the 1 MW scan, in the region of minimization, the potentials were similar to that of having no RF [33]."‡ While the heavy Z impurity for C-Mod is molybdenum, the interior wall of C-Mod is coated in boron [64]. Therefore the impurities measured in this experiment were boron and "found to be minimized for $P_{in}/P_{tot} \sim 0.5 - 0.8$ for both near and far from the antenna [33], [34], [57]."‡

4.3 Simulation Set-Up

"For replicating the C-Mod 4 strap antenna numerically, the simulation domain was taken to be a 2D slice along the 10 degree pitch angle of the background magnetic field in the mid-plane of the field-aligned antenna shown in Fig. 4.1. For these simulations, the phase factor that represents the parallel wavenumber, $k_{\|}$, is imposed through the physical dimensions of the 4 antenna current straps as well as their dipole phasing of $0/\pi/0/\pi$ which resulted in $k_{\|} = 11\ m^{-1}$. The features and dimensions of this 2D mesh were taken from a slice of the"‡ 3D Computer Aided Design "(CAD) of the ICRF antenna that did not include the Faraday screens. The computational domain spanned from $R_{major} = 0.4$ to 1.1 m and -0.6 to 0.6 m in the tilted quasi-toroidal plane. Following the true C-Mod geometry, the front of the RF limiters were placed at $R_{major} = 0.913$ m and the front of the current straps was placed at $R_{major} = 0.935$ m. The current straps were simplified to be boxes of current with dimensions

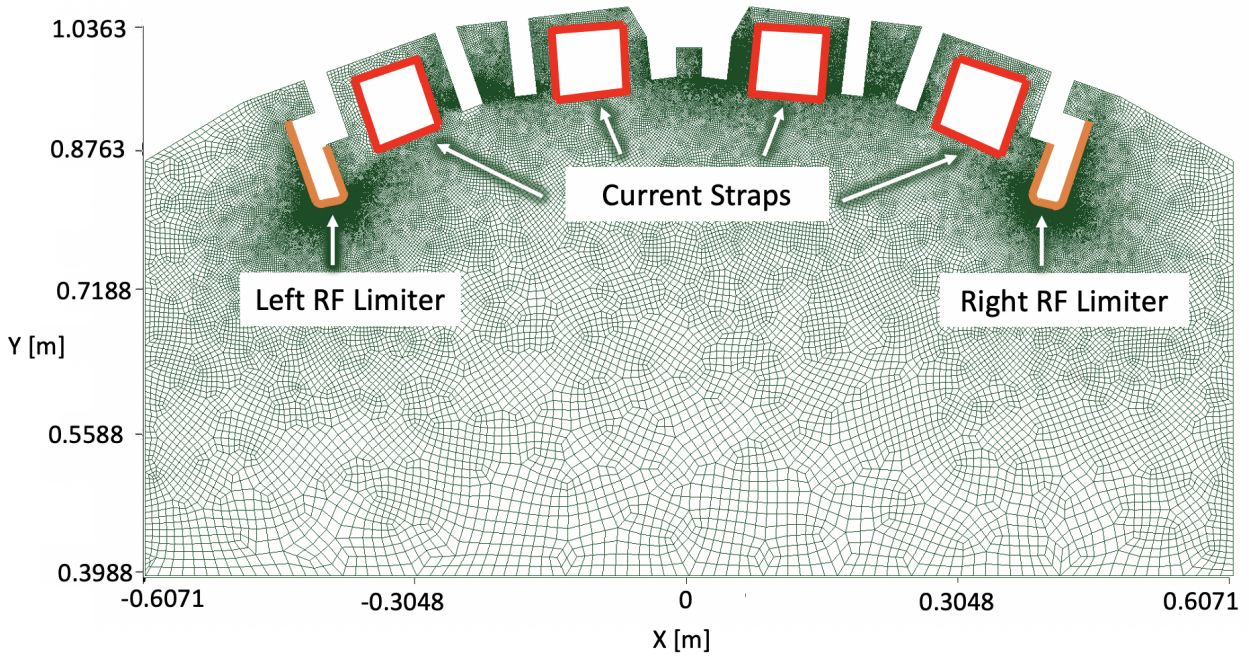

(a) The 2D Stix domain in Cartesian coordinates. The RF sheath BC is applied along both the left and right RF limiters shown in orange while the current strap boundaries are shown in red.‡

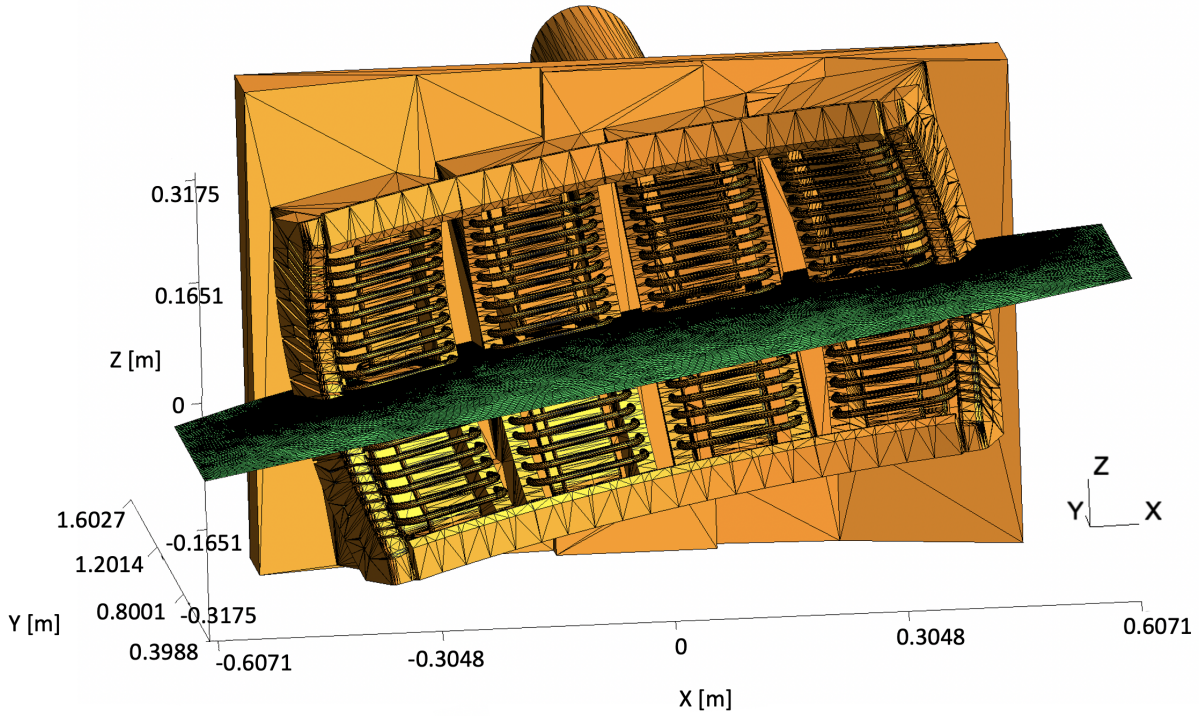

(b) Stix 2D domain (green surface) superimposed on the full 3D CAD of the C-Mod ICRF Antenna (orange surface).‡

Figure 4.1: 2D slice of the 4-strap field aligned ICRF antenna on C-Mod taken along the 10 degree pitch angle of the magnetic field. This is the computational domain taken in the Stix simulations.‡

of 70 mm in the quasi-toroidal direction and 10 mm in the radial direction in which each strap's total current was set using Dirichlet boundary condition on tangential component of the magnetic field, H_t. The poloidal current was assumed to be a cosine squared profile that peaks at the center of the strap near the mid-plane. Given that the poloidal variation is not represented in the Stix 2D plane, the amplitude of the current was taken to be at the peak of the cosine squared poloidal profile that corresponds to the mid-plane of the antenna."‡

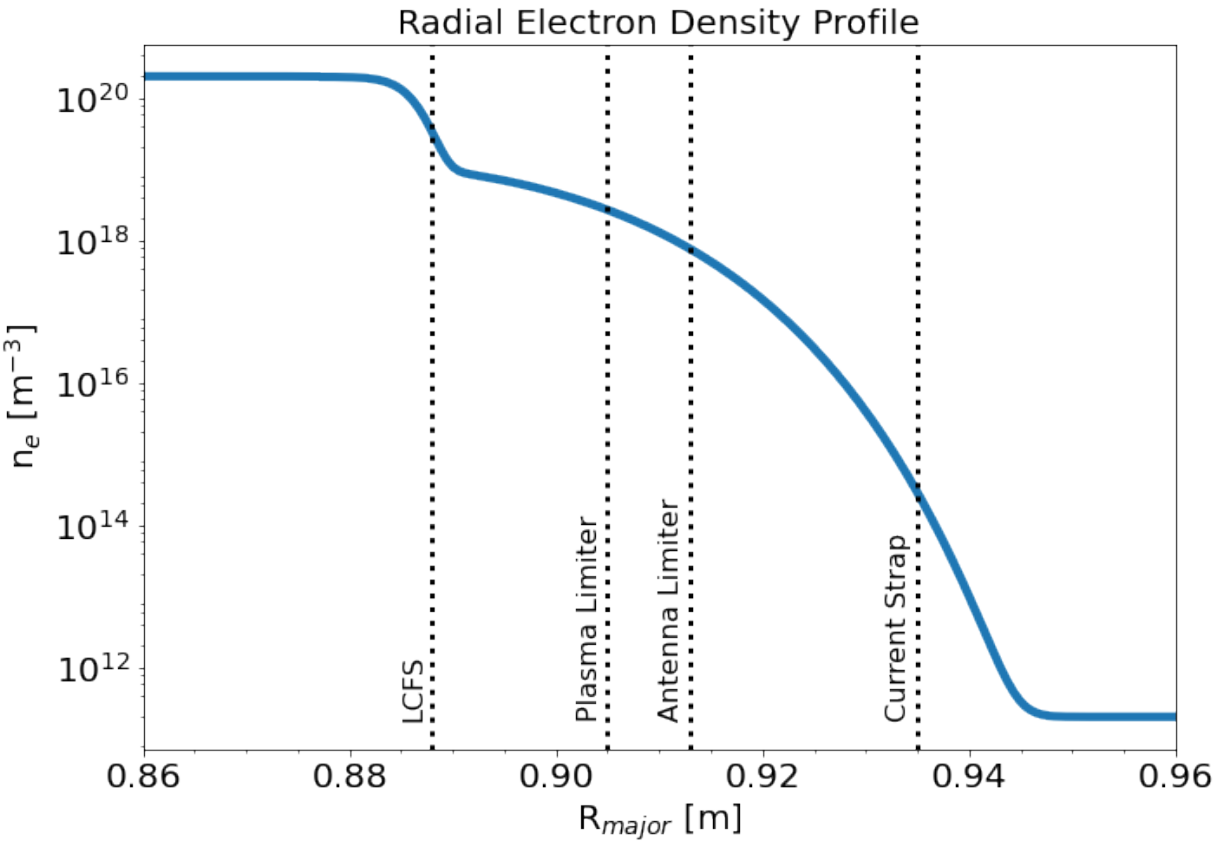

Figure 4.2: Radial electron density profile taken in Stix's simulations. In this profile the LH resonance is located just behind the antenna limiter at 0.915 m thereby having a region for propagating SWs in between the front of the current straps and the antenna limiters.‡

"The radial electron density profile was found using a pedestal-like sech profile along the major radial direction adapted from Kohno et. al 2015 given by Eq. 4.1 where j represents the particle species of deuterium ions and electrons [65]. To get as close as possible to experimental conditions, for this simulation the density profile used two pedestal-like profiles in which $\lambda_{n,j}, \nu_j, n_{max,j}$, and $n_{min,j}$ in Eq. 4.1 were parameterized to fit previously measured L-mode density scans from C-Mod [66]. This experimental density data was only measured to the RF limiter which is located at 0.913 m and therefore for this simulation the profile

needed to be extrapolated to the vacuum vessel wall using a ~ 2.4 mm e-folding depth. The parameterized electron density profile is shown in Fig. 4.2. In this profile the lower hybrid resonance occurs just behind the RF limiter at 0.915 m, the slow wave cutoff (P = 0) occurs just in front of the current straps at 0.934 m, and a density below the plasma frequency occurs at and behind the current straps."‡

$$n_j\left(R_{major}\right) = \left(n_{max,j} - n_{min,j}\right) \operatorname{sech}\left[\left(\frac{R_{major}}{\lambda_{n,j}}\right)^{\nu_j}\right] + n_{min,j} \tag{4.1}$$

"These simulations did not include the high-field side in the domain and therefore to account for no wave reflections, an artificial collisional profile was used through an effective mass of the electrons. This profile was chosen as an exponential profile, similar to damping profile given in [47], which increased in strength as the wave propagates towards the core represented in Eq. 4.2."‡

$$\nu_{absorb}\left(R\right) = C_1 \exp\left[-\frac{\left(R - R_{min}\right)}{\lambda_1}\right] \tag{4.2}$$

"Here C_1 represents the strength of absorption, λ_1 represents the e-folding decay length scale, and R_{min} represents the beginning of the domain on the high field side at 0.4 m. Using values $\lambda_1 = 0.035$ m and $C_1 \sim 10^2\omega$, gave an absorption profile that showed no reflected waves verified through fast Fourier transforms of the resulting electric fields."‡

"In addition to damping out the launched wave, given the density profile used there were two problematic regions that needed to be resolved using artificial collisionality: the lower hybrid (LH) resonance at S = 0 and the slow wave cutoff at P = 0. Usually cutoffs are not an issue for EM RF solvers, however because Stix solves for the magnetic field, the dielectric tensor, $\bar{\bar{\varepsilon}}$, needs to be inverted therefore making P = 0 a singularity. For both P = 0 and S = 0 layers, the artificial collisional profile used was a thin Gaussian represented by Eq. 4.3."‡

$$\nu\left(R\right) = C_2 \exp\left[-\frac{\left(R - R_{loc}\right)^2}{\lambda_2}\right] \tag{4.3}$$

"Similar to Eq. 4.2, C_2 is the strength of absorption, λ_2 is the squared e-folding decay length taken to be 10^{-4} m^2, and R_{loc} is the location of the resonance/cutoff. In contrast to Eq. 4.2, Eq. 4.3's C_2 was on the order of $\sim \omega$ due to the fact that the solver needed only a small amount of finite collisionality to resolve the singularity rather than be strong enough to damp out the wave entirely. For the P = 0 layer, the term with the most influence for these plasma parameters is the electron contribution and therefore modifying the artificial collisional frequency of the electrons, ν_e, using Eq. 4.3 allowed the cutoff to be resolved.

Similarly, the LH resonance can be resolved by adding some finite amount of collisionality to the ion term shown in Eq. 4.3."‡

"The last plasma profile needed was the background magnetic field which was taken from an EFIT reconstruction of the magnetic equilibrium of the experimental discharges, stored in an EQDSK file format [67]. This file only has the flux function calculated for the poloidal (R, Z) plane and therefore a transformation into the Stix computational reference frame needed to be done. This was done by transforming the magnetic field values from the poloidal cross section to a 3D torus then finding the values that corresponded to the tilted top-down view of the 4-strap antenna."‡

"Given the sharp density gradients, the existence of the lower hybrid resonance and SW cutoff, and the proximity of these layers to one another, this problem poses difficulty to numerically resolve. Shown in Fig. 4.3 is the evolution of the uniform global refinement of the mesh with both linear and second order polynomials on the real parallel electric field using the Stix code. With increasing uniform refinement and 2nd order polynomials, the solution of the SW propagating in this thin region becomes increasingly visible. The first and second most resolved cases showed the H field solution's norm varied by 0.01% from one another deeming the solution to be resolved. Every uniform refinement increases the number of elements by 4× therefore allowing for only a few"‡ successive refinements increasing the memory footprint of Stix. "The most intensive simulations were the order 2 polynomial with uniform refinement of 1 with $\sim 5 \times 10^5$ elements at $\sim 1.7 \times 10^6$ number of unknowns. From these refinement simulation studies, a key takeaway is that in the region in between the RF limiters and the front of the current strap using a realistic density profile, it is necessary to have significant resolution using higher order polynomials along with some non-negligible artificial damping at the S = 0 and P = 0 layers when using a cold plasma model."‡

4.4 Calculated Rectified Potentials

The following section describes the three different antenna phasing scenarios simulated in Stix to look at the behavior of near-field sheaths with respect to varying antenna power ratio. First, the original dipole phasing scheme of $0/\pi/0/\pi$ that was used in the experiment is simulated. Next, the investigation of using a phasing of $0/0/0/0$ in which the 4 straps of the antenna act as monopole antenna is examined. Lastly, due to the drastically different behavior of the minimization in the parallel electric fields found in TOPICA modeling of the JET and ITER antenna for $0/\pi/\pi/0$ [21], [68], this phasing scheme is simulated and compared against the previous phasing regimes in the C-Mod Stix simulations.

For all three antenna phasing scenarios in Stix, "the sheath BCs were placed on the faces

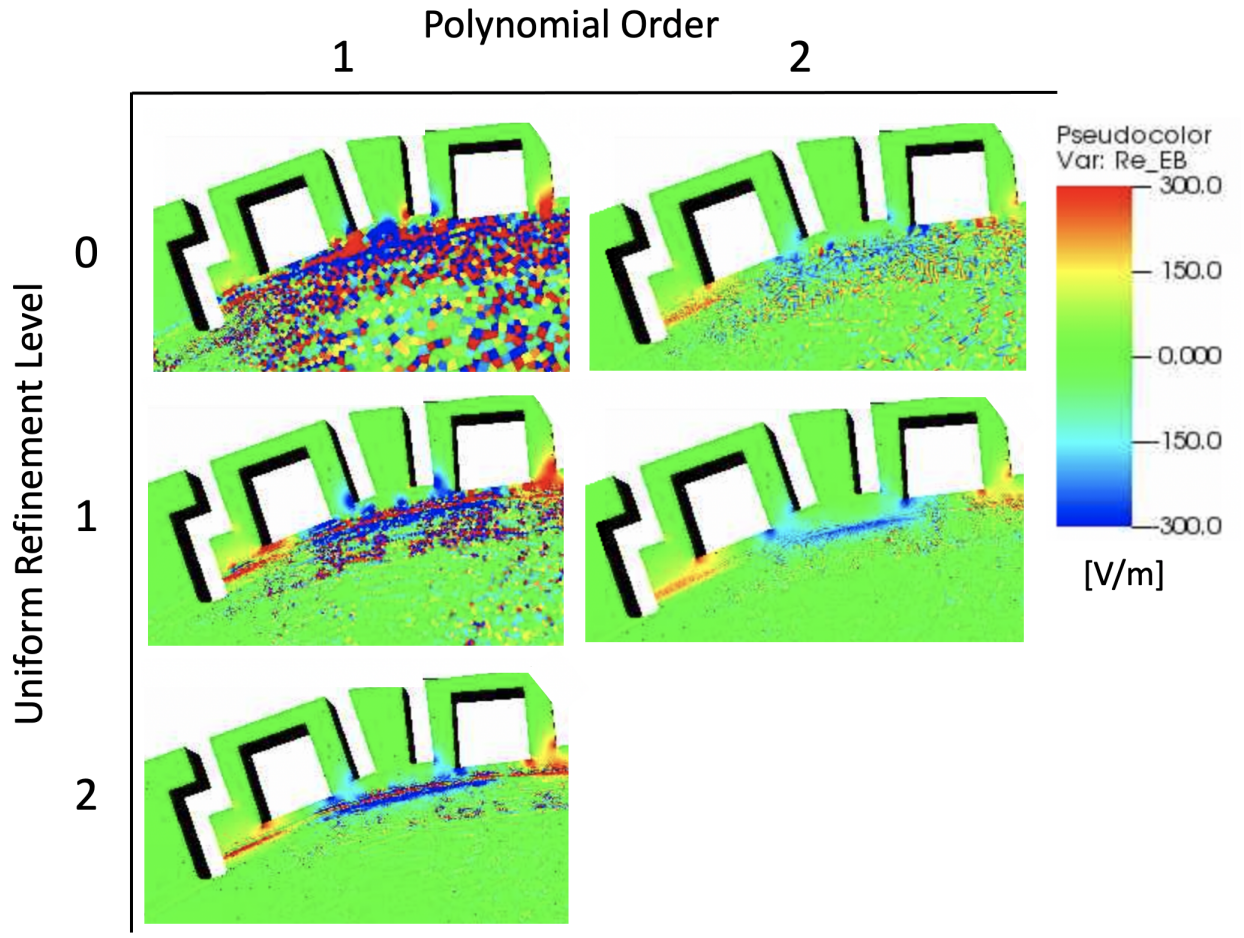

Figure 4.3: Pseudo-color plot of the real parallel electric field for $P_{in}/P_{tot} = 0.5$ for various uniform refinement levels (RS) and order of finite element polynomial. The RS value denotes the number of times the mesh has been refined uniformly with 0 as no refinement. This region is highlighting the slow wave propagation between the front of the current strap boxes and the RF limiter that is responsible for this rectification. The noise is due to the sharp density gradient in addition to the LH and P = 0 SW cutoff nearby which needed to be resolved with artificial collisionality.[‡]

of both the left and right RF limiters, shown by the orange lines in Fig. 4.1a, bypassing regions in which the magnetic field is tangent to the surface where the sheath BC breaks down [16]. All other domain boundaries for these simulations were taken to be conducting wall in which lossy materials were not considered. Emulating C-Mod's experiment, a pure deuterium plasma was used along with a background magnetic field of 5.4 T on axis read in from the EQDSK. A constant temperature profile of 10 eV was taken which was only used within the sheath BC. Using a 80 MHz launched wave, power-phasing fractions of P_{in}/P_{tot} = 0.05 to 1.0 were scanned."‡ "Both 1 and 1.5 MW cases were run in which the total power

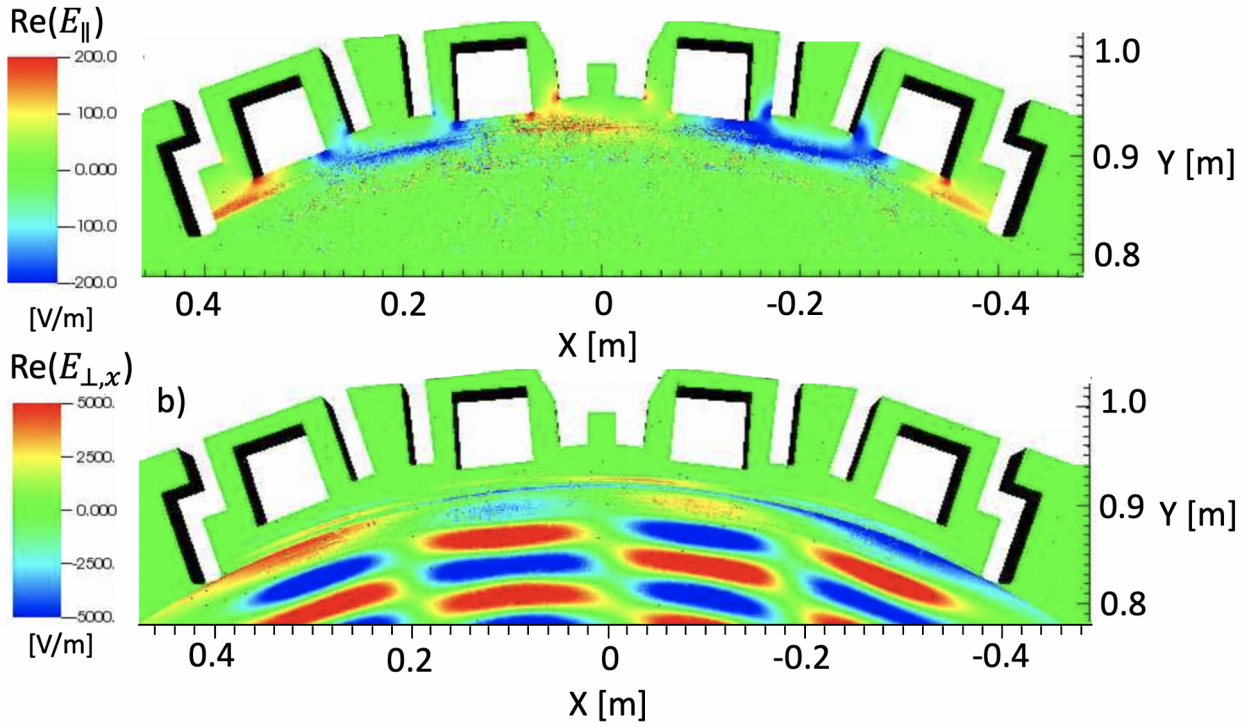

Figure 4.4: Pseudo-color plot for the case P_{in}/P_{tot} = 0.5 showing a) the real parallel electric field, Re($E_\parallel$), representing the slow wave and b) the real perpendicular electric field, Re($E_{\perp,x}$), representing the fast wave. It should be noted that this plot does not show the entire computational domain.‡

of the 4 straps was held constant and the total current of each strap was adjusted to match the given power fraction. The resulting parallel electric field and rectified potentials were measured on both the left and right RF limiters and found to have the largest values on the inner facing components. This region of enhancement aligns with the fact that the C-Mod density profile traps the propagating SW in the region between the front of the straps and the RF limiter. Plotting the real parallel and perpendicular electric fields in Fig. 4.4

shows the propagating SW and its intersection with the limiter corresponding to where the rectification was found."‡

4.4.1 Standard Dipole Phasing - $0/\pi/0/\pi$

Here the results of the simulating a true dipole antenna phasing of $0/\pi/0/\pi$ which was used in the C-Mod experiment are described. Using this configuration results in the first and third antenna strap's currents following the same direction and similarly having the second and fourth current straps following the exact opposite direction. Having this kind of formation is advantageous because it maximizes the image currents generated on the metal antenna box that influence the formation of RF sheaths and produces a more peaked antenna spectrum with respect to $k_{\|}$ [34], [57].

"Shown in Fig. 4.5a is the resulting DC rectified potentials (V_{REC}) taken at the location where the largest potential was found. This peak occurred on the left inner facing limiter for both 1 and 1.5 MW cases. Similarly, Fig. 4.5b shows the parallel electric field magnitude taken at the same point as in Fig. 4.5a. In both power-phasing scans, one sees that there is a minimization of $E_{\|}$ and V_{REC} for $P_{in}/P_{tot} \sim 0.8-0.95$. The only difference in trends between V_{REC} and $E_{\|}$ is that there is less of an increase towards the highest fraction in the V_{REC} plot. This distinction is due to the fact that the RF sheath rectification is a non-linear effect which was also observed in TOPICA runs of the JET A2 antenna [21]. Using a linear sheath boundary condition, taking $z_{sh} \sim \infty$, would show the rectified potentials follow the same trend as the parallel electric field and would overestimate their values particularly towards the highest P_{in}/P_{tot} fractions."‡

"Fig. 4.5 shows that Stix's 2D reference frame along the background magnetic field in the middle of the antenna does not produce a large amount of rectification given that the Bohm sheath is at 31.86 V. This suggests that there are 3D geometrical effects not accounted for. The importance of these 3D effects is supported by the experimental measurements and TOPICA simulations of V_{RF} and the tungsten sputtering yield (Y_w) found to significantly change in strength and shape in the poloidal direction on the limiters in the AUG 3-strap antenna [21], [32]. Comparing the values of the measured V_{RF} on AUG in the region closest to Stix's reference frame shows that V_{REC} are at the lowest values agreeing with the low voltages found for Stix's scans. In addition to the 2D reference frame, the amplitude of V_{REC} is strongly dependent on the strength of the SW. While not as realistic to the true density in the experiment, it was seen in Stix simulations using a density profile that pushed the SW cutoff behind the current straps resulted in ~ 20 V higher values of V_{REC}. Even though changing the density profile resulted in a different amplitude of V_{REC}, the minimization

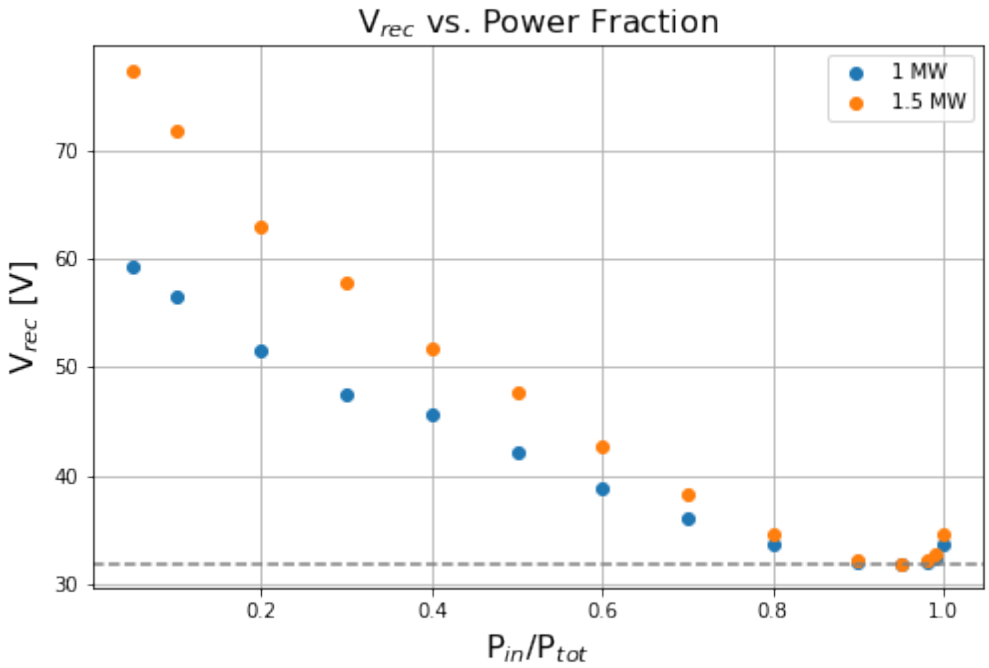

(a) The rectified potential versus the ratio of RF power on the 2 central straps to the total 4 straps for both 1 (blue) and 1.5 (orange) MW.‡

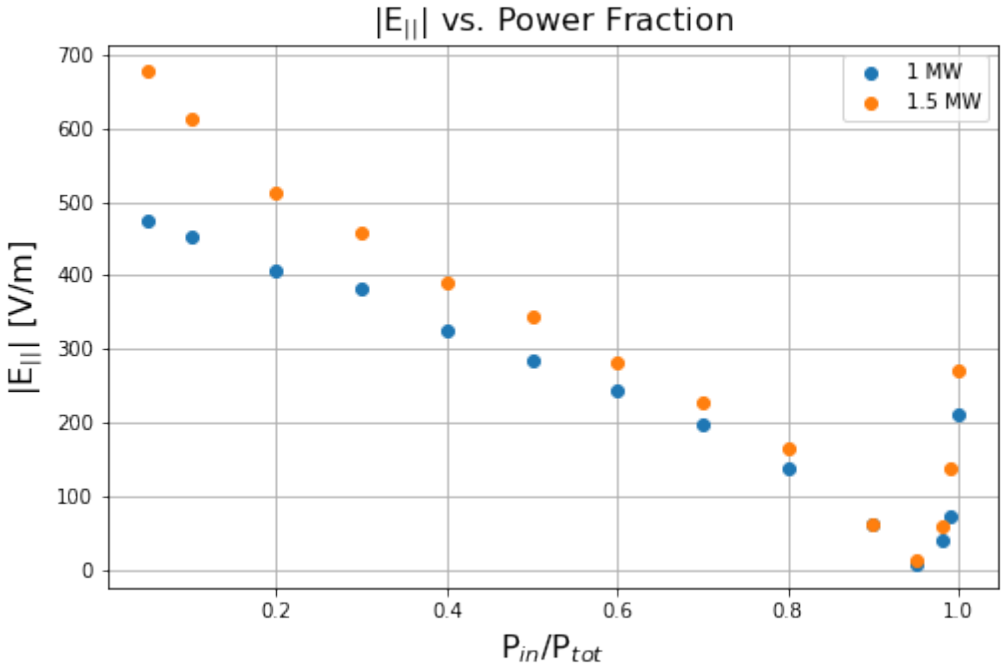

(b) The magnitude of the parallel electric field versus the ratio of RF power on the 2 central straps to the total 4 straps for both 1 (blue) and 1.5 (orange) MW.‡

Figure 4.5: The peak DC rectified potential a) and the corresponding magnitude of the parallel electric field b) for the $0/\pi/0/\pi$ dipole phasing for both the 1 and 1.5 MW cases. These data points were taken at the same positional location corresponding to the largest rectification on the inner RF limiter.‡

stayed at the same power fraction range. This effect was also seen in similar TOPICA and SSWICH simulations of the JET A2 antenna [21]."‡

"Comparing to the C-Mod measured enhanced potentials given in [34], Stix's V_{REC} shows qualitative agreement in the trend that minimization occurs at around $P_{in}/P_{tot} \sim 0.85$. It is difficult to compare the GPI measurements" and Langmuir probe data "of the plasma potential to the V_{REC} found in Stix due to the fact that they are measured in different locations." Additionally, the GPI experimental data measured was the E×B velocity taken to be a proxy for the DC potentials while the Langmuir data is not a direct measurement at the antenna because it was taken at the upper divertor on a magnetic field line connected to the antenna. "The simulated enhanced potentials from Stix are taken from the inner facing left RF limiter near the mid-plane of the antenna while the experimental data is taken in the upper outer corner of the antenna box. It has been seen both experimentally and in EM simulations that there is a larger enhancement of electric fields and rectified potentials around the corners of the antenna box than at the mid-plane of the antenna that would explain the difference in rectification strength of Stix versus experiment [32], [49]. This difference in where V_{REC} was measured between simulation and experiment would also explain the shift of the minimum towards a higher power fraction seen in Stix. This effect of the poloidal variation in the minimum of $\langle V_{RF} \rangle$ was seen in TOPICA and RAPLICASOL simulations that showed a shift towards the highest fractions in the same regions as the Stix 2D reference frame [32]."‡

"More generally, due to the complicated nature of this region in the plasma it is difficult to get a quantitative analysis of V_{REC} for comparing computational and experimental data. There are two notable limiting factors: 1) one cannot truly know the density in front of antenna straps since it is inaccessible to density diagnostics and 2) there are transport effects like the E×B flow that are neglected. Transport effects play a key role in RF sheath rectification as discussed in the introduction [69]. These effects can be seen experimentally in the 3-strap AUG antenna which measured density fluctuations in various locations along the front of the antenna that would affect the resulting enhanced potentials [70]."‡

4.4.2 Monopole Phasing - 0/0/0/0

The following phasing simulations were run using all the antenna current straps following the same direction, also known as a monopole configuration. "It should be noted that previous experiments on the field-aligned C-Mod antenna using monopole (0/0/0/0) phasing showed a significant increase in enhanced potentials [71]. Due to all the current strap's phasing being in the same direction, the image current cancellation is drastically reduced allowing for

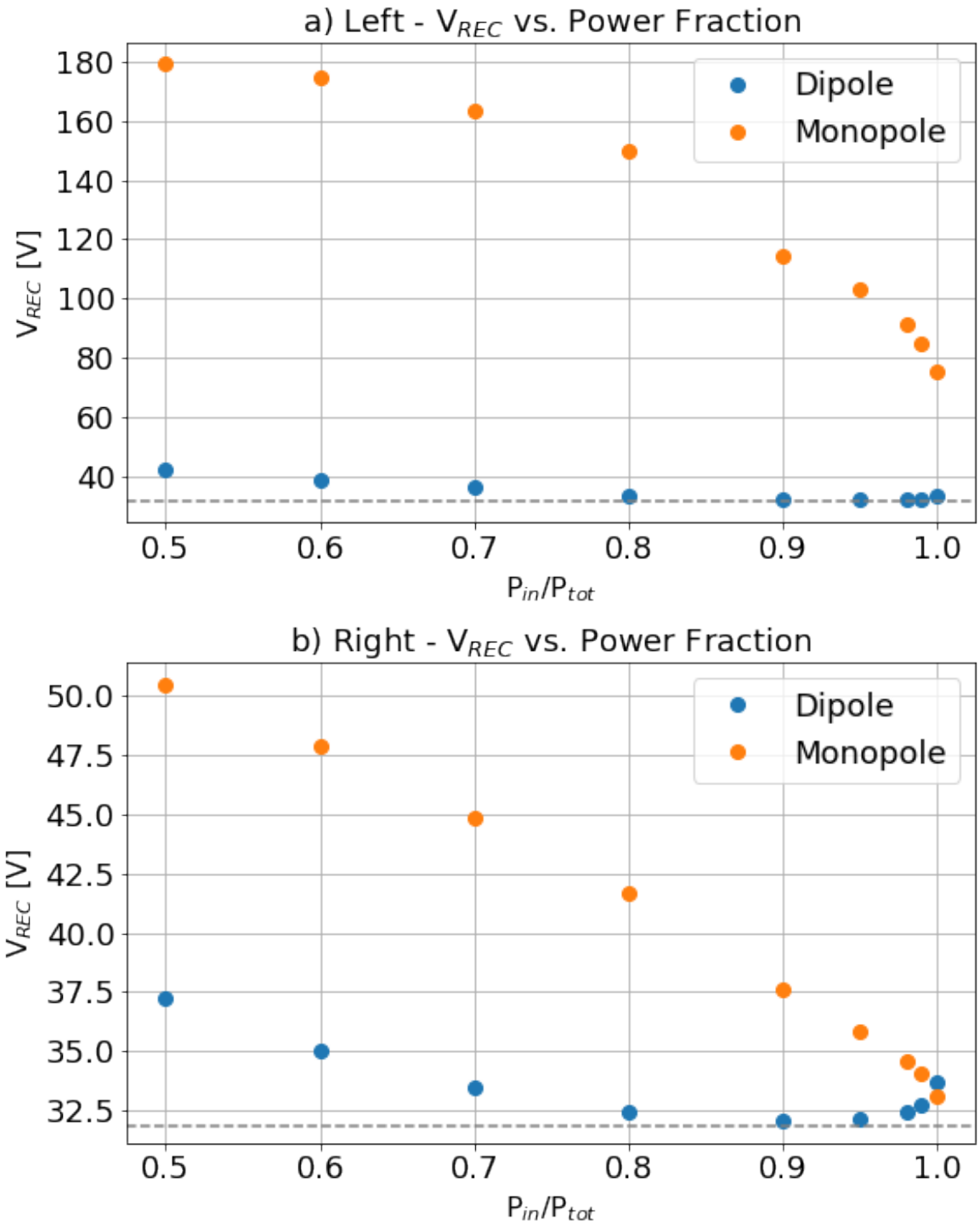

Figure 4.6: Comparison of monopole (0/0/0/0) and dipole ($0/\pi/0/\pi$) phasing of rectified potential versus power phasing (from $P_{in}/P_{tot} = 0.5$ to 1.0) taken at strongest rectification point on the a) left and b) right inner RF limiters. The grey dashed line denotes the Bohm sheath.

much more sheath rectification. Using the same plasma conditions and background magnetic field, running Stix's C-Mod configuration with monopole phasing for $P_{in}/P_{tot} = 0.5$ to 1.0 confirmed what is seen experimentally. A comparison of the peak sheath rectification for the monopole and dipole phasing is shown in Fig. 4.6. The potentials in Fig. 4.6a are taken at the largest point of rectification on the right RF limiter's inner side in contrast to Fig. 4.6b where the potentials are taken on the left RF limiter's inner side for both phasing regimes. On both sides of the antenna's RF limiters, the rectification is enhanced with monopole phasing with no minimization. Fig. 4.6 also shows an asymmetry of the strength of the sheath potential, an effect that is seen in"‡ all "phasing Stix simulation scans but which is exacerbated with monopole phasing. This effect comes from the poloidal magnetic field variation and is also seen experimentally as shown in [32]."‡

4.4.3 Modified Dipole Phasing - $0/\pi/\pi/0$

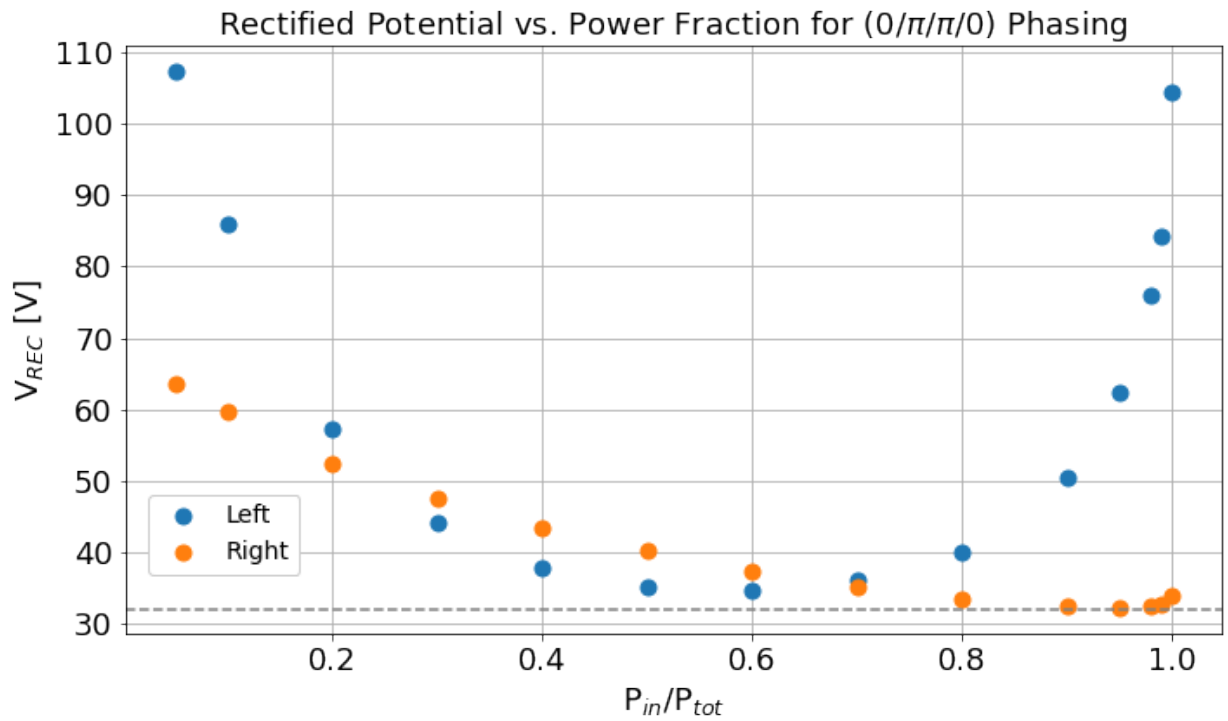

Figure 4.7: The rectified potentials for the modified dipole phasing of $0/\pi/\pi/0$ taken on the left (blue) and right (orange) inner RF limiter for various antenna power phasing fractions. The thermal Bohm sheath of 31.86 V is plotted by the grey dashed line.

The last phasing scheme discussed here is using $0/\pi/\pi/0$, referred to here as the modified dipole phasing, in which the two middle straps have currents in the same direction while the two outer straps currents follow the opposite direction. The decision to simulate this

antenna phasing case was motivated by TOPICA simulation results of both the JET and ITER antenna [21], [68]. For the JET simulations, a comparison between the standard dipole, $0/\pi/0/\pi$, and the modified dipole, $0/\pi/\pi/0$, showed that the modified dipole phasing resulted in a shift of the minimum of $\langle E_{\|} \rangle$ to a much lower power phasing fraction of $P_{in}/P_{tot} \sim 0.2$ - 0.4 versus $P_{in}/P_{tot} \sim 0.6$ - 0.8 for the standard dipole phasing [21]. Similarly, the ITER simulations showed $\langle E_{\|} \rangle$ minimizing for the modified dipole phasing between $P_{in}/P_{tot} \sim 0.3$ - 0.6 versus the standard dipole phasing that minimized at $P_{in}/P_{tot} \sim 0.8$ - 1.0 [21], [68]. Further ITER simulations showed that the power coupling of the antenna to the plasma was higher for the modified dipole phasing than the standard dipole phasing which is vital for larger machines like ITER due to the long evanescent layer in front of the antenna providing motivation for using this phasing scheme [68].

Fig. 4.7 shows the DC rectified potentials for left and right sides of the RF limiter. Each data point is taken at the same inner limiter location that corresponds to the peak voltage. Like the monopole phasing case, it is seen that there is variation in strength of the rectified potential on the left and right limiters due to the poloidal magnetic field. When compared to Fig. 4.5a, this phasing scheme's minimization occurs at a much lower power fraction of 0.4 - 0.8 and is much broader. The voltages in Fig. 4.7 are higher for the left limiter than those seen in the standard dipole configuration in Fig. 4.5a for both the high and low power fractions. These results are not surprising given at these extreme power ratios the antenna acts like a monopole and therefore imagine currents are not as influential at minimizing $E_{\|}$. The TOPICA modeling of the JET and ITER antennas show a similar shift to lower power phasing fractions. This difference is due to the strong image currents induced in the center of the antenna given that the two inner straps are in phase with one another and therefore there is minimal image current cancellation in the center. Although the extremes of the power fractions have higher potentials, the minimum in this case hovers just above the thermal Bohm sheath and is much closer to the $P_{in}/P_{tot} = 0.5$ regime. It may be more advantageous to move towards lower P_{in}/P_{tot} fractions given that it helps with turbulence suppression in the far SOL [72], [73]. Running this antenna phasing scheme using the full 3D geometry would be worthwhile to explore if this scheme is more favorable to use that the standard dipole phasing.

4.5 Implications for Sputtering of Impurities

The previous section reported various DC voltages for the inner side of the RF limiters on C-Mod using three different antenna phasing schemes. With the knowledge of these potentials, one can derive some insights into the sputtering of impurities and the subsequent erosion

rate. Sputtering is the process of an incoming ion hitting and displacing an atom from the wall material into the plasma. The common metric to use is a sputtering yield curve in which one can calculate the loss of atoms from the plasma facing component into the plasma. The amount of impurities largely depends on the incident ion's energy, the material of the wall, and the angle of incidence [15]. There exists a threshold in energy that the incident ion must have in order exceed the surface binding energy of the lattice structure for sputtering to occur. This threshold varies with the both the mass of the incident and target atoms [15]. Table 4.1 [74] shows the various threshold energies for the bulk ion and common impurities species found in C-Mod [64] impinging on the wall materials of both molybdenum and boron. Boron is included in this analysis due to C-Mod having $\sim 0.2\mu$m thick boron layer coating the molybdenum walls [40]. The possible incident ions considered here are the bulk species is deuterium (D) and the impurities of boron (B), carbon (C), oxygen (O), and molybdenum (Mo).

	Incident Ion				
Target Ion	Deuterium	Boron	Carbon	Oxygen	Molybdenum
Boron	20 eV	35 eV	40 eV	40 eV	106 eV
Molybdenum	90 eV	31 eV	55 eV	27 eV	64 eV

Table 4.1: The threshold energy in eV needed for the incident ion to sputter out the target wall atom taken from [74] and calculated using Eq. 18 of [14].

First, the question of how much impurity flux is generated from the standard dipole operation using 1 MW of RF power is considered. The following analysis is a qualitative calculation using empirical expressions for the sputtering yield values and is done to provide an estimate of the impurity fluxes generated by the enhanced potentials. To calculate these values, one needs to know the ion flux into the sheath given by the density at the top of the sheath multiplied by the ion sound speed and the resulting sputtering yield, Y_s, based on the incident ion's energy hitting the wall [15]. Y_s can be obtained using a sputtering yield curve calculated from an empirical parameterization[1] by Yamamura et. al 1996 [14]. Fig. 4.8 shows an example of such a sputtering curve where the incident ion is taken to be D impinging on either a B (orange curve) or Mo (blue curve) target. Fig. 4.8 emphasizes the influence of the target material's mass in which there is more resulting sputtering from deuterium impinging on boron (Z=5) than deuterium impinging on molybdenum (Z=42).

It should be noted that the empirical Y_s from this analysis is less realistic for incident ion energies that are close to the threshold energy due to the model not accounting for all the forces at play [75], [76]. An impurity flux binary collision approximation (BCA) code is a

[1]Provided by Prof. D. Curreli and A. A. Gonzalez Galvan from University of Illinois Urbana-Champaign.

more appropriate method to yield a quantitative value for the sputtering yield values and as a result, current efforts are underway to couple Stix to the impurity generation code RustBCA for this power phasing scan [75], [77]. The Yamamura et. al 1996 [14] empirical sputtering yield parameterization used here is further described in Appendix C. Additionally, the other incident ion sputtering yield curves used for this calculation are plotted in Appendix C. The incident ion energy is taken to be Eq. 4.4 in which both the kinetic and potential components of energy are included [15].

$$E_0 = 2T_e + qZ_i|V_{REC}| \text{ [eV]} \tag{4.4}$$

For the ion flux, the density is taken to be that corresponding to the location where the peak enhanced potentials were measured and equated to 10^{17} m^{-3} for this case. Additionally, the densities used for the impurities for boron, carbon, and oxygen are taken to be 1% of the electron density while the molybdenum's density in the plasma is taken to be 0.01% of the electron density based on L-mode measurements done in C-Mod [40], [64], [78].

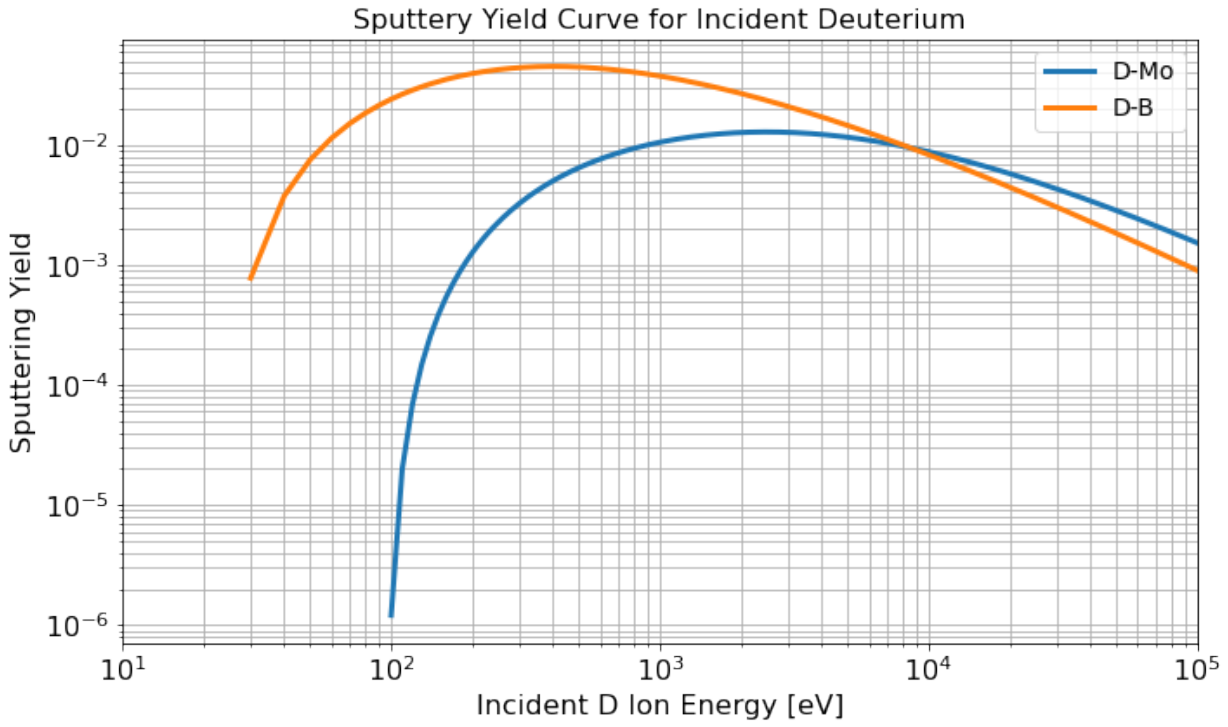

Figure 4.8: The empirical parameterization calculated using [14] of the sputtering yield curve for an incident deuterium ion impinging on a molybdenum (blue) and a boron target (orange).

Figure 4.9 shows the resulting impurity fluxes for each sputtering combination. The top figure represents a boron target while the bottom figure shows the impurity flux using a molybdenum target. Seen in the molybdenum target figure is that there is no D $\rightarrow$ Mo

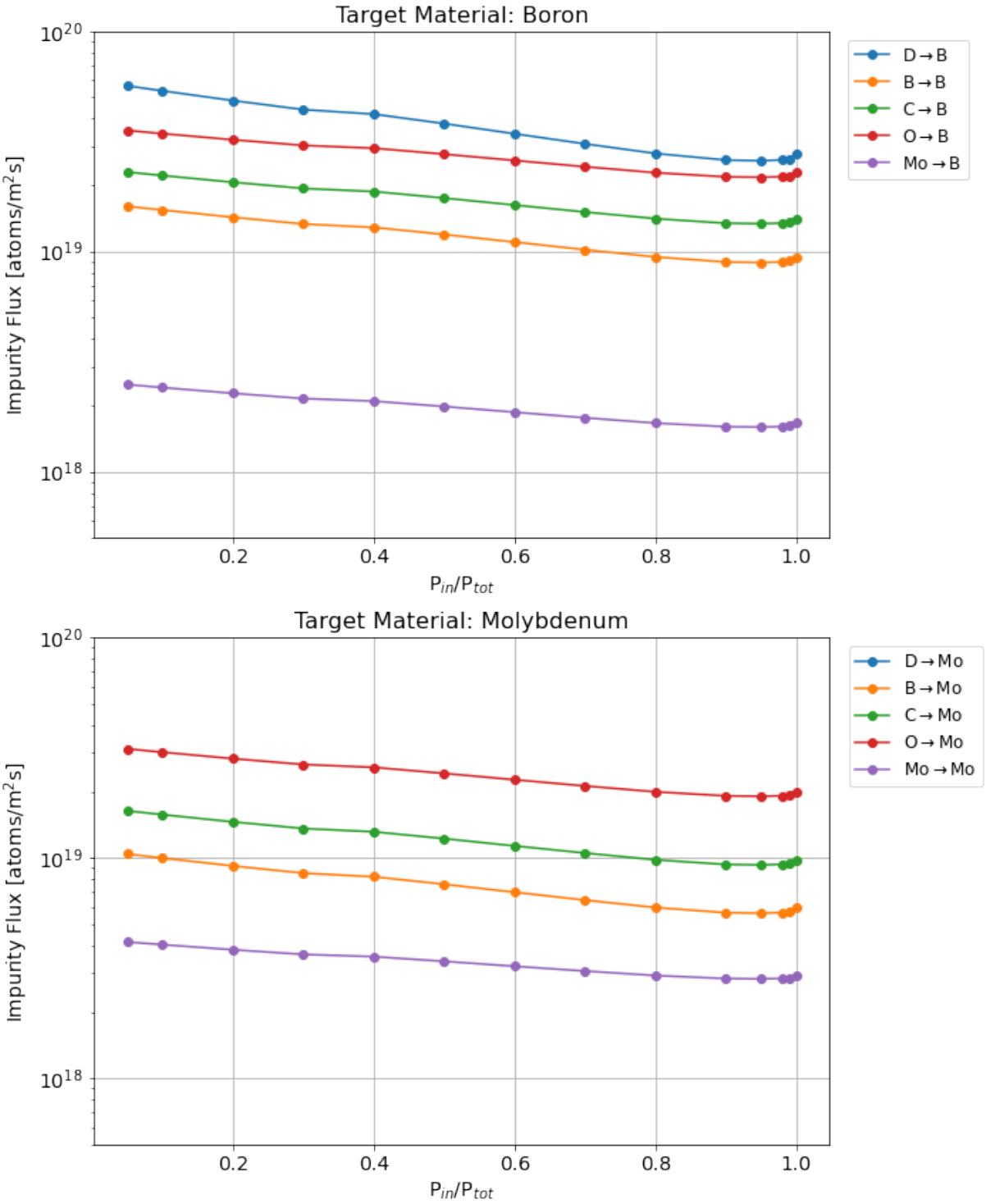

Figure 4.9: The resulting impurity flux from simulated RF near-field sheaths found for the standard dipole phasing of the 4 strap ICRF antenna on C-Mod using 1 MW. The top figure shows various incident ions impinging on a boron wall and conversely the bottom figure shows the same ions impinging on a molybdenum wall.

sputtering due to the high threshold energy of Mo at 90 eV. These two plots also show the expected result that a boron target results in an order of magnitude larger impurity flux into the plasma due to boron being much lighter than molybdenum. Additionally, the impurity flux from a boron wall shows that the deuterium ion produces the largest sputtering values due to the bulk ion species consisting of deuterium and therefore has the largest density amongst the considered ion species.

Figure 4.9 gives an idea of the impurity flux but in terms of engineering constraints calculating the erosion rate is a better metric for how problematic RF sheaths are. The method described in Stangeby 2000 [15] is used to calculate this erosion rate from the resulting enhanced potentials for the 1 MW case for an incident D or Mo on both B and Mo targets. To get the erosion rate one needs to know the DC rectified voltage drop across the sheath, the electron and ion temperatures, the density of the target wall material, and the sputtering yield from the resulting impact energy given by Eq. 4.4. The assumptions taken here are that the ion and electron temperatures at the wall are both 10 eV, the plasma is run 24/7 all year (steady-state), and that the incident ion angle into the wall is 90°, true for the location of the rectification found in Stix. The equation for the erosion rate is given by

$$\begin{aligned} \text{Erosion Rate} &= \frac{\Gamma_{inc} Y_s}{n_{tar}} \left[\frac{m}{s}\right] * 3.154 \times 10^7 \left[\frac{s}{yr}\right] * 100 \left[\frac{cm}{m}\right] \\ &= 3.154 \times 10^9 * \frac{n_i c_{s,inc} Y_s}{\rho_{tar}/m_{tar}} \left[\frac{cm}{yr}\right] \end{aligned} \tag{4.5}$$

Here the "inc" subscript indicates the incident ion, the "$targ$" subscript is the target wall material, and Y_s term represents the resulting sputtering yield [15].

Table 4.2 shows the resulting erosion rates for the three antenna phasing cases. The worst and best case scenarios correspond to the power fraction that has the lowest or highest collective, from both the left and right side, enhanced potentials respectively. Here, the largest potential in both the worst and best cases is chosen to represent the most detrimental erosion for the phasing scenario. The values indicated as "n/a" meant that the incident ion's impacting energy wasn't enough to exceed the energy threshold of the target material. The trend from this table is as expected; the larger the rectification, the more erosion of the material occurs. Similarly, it is not surprising that there is more erosion of a boron surface than the much heavier molybdenum surface for the incident deuterium ion. In contrast, an incident molybdenum ion impinging on a molybdenum surface produces more sputtering than boron due to the higher likelihood of the molybdenum embedding itself in the boron material.

It is seen that even in the best case scenario, in which the potential is essentially a thermal

Standard Dipole Phasing ($0/\pi/0/\pi$)	Best Case (31.86 V)	Worst Case (59.31 V)
D $\rightarrow$ Mo	n/a	n/a
D $\rightarrow$ B	0.062 cm/yr	0.137 cm/yr
Mo $\rightarrow$ Mo	0.139 cm/yr	0.204 cm/yr
Mo $\rightarrow$ B	0.004 cm/yr	0.006 cm/yr

Monopole Phasing (0/0/0/0)	Best Case (75.29 V)	Worst Case (179.22 V)
D $\rightarrow$ Mo	2.7×10^{-7} cm/yr	0.190 cm/yr
D $\rightarrow$ B	0.172 cm/yr	0.295 cm/yr
Mo $\rightarrow$ Mo	0.233 cm/yr	0.395 cm/yr
Mo $\rightarrow$ B	0.007 cm/yr	0.011 cm/yr

Modified Dipole Phasing ($0/\pi/\pi/0$)	Best Case (34.61 V)	Worst Case (107.34 V)
D $\rightarrow$ Mo	n/a	0.019 cm/yr
D $\rightarrow$ B	0.070 cm/yr	0.226 cm/yr
Mo $\rightarrow$ Mo	0.147 cm/yr	0.279 cm/yr
Mo $\rightarrow$ B	0.004 cm/yr	0.008 cm/yr

Table 4.2: The erosion rates for the three antenna phasing schemes from using the smallest (best case) to largest DC potential (worst case) scenario found in Stix over $P_{in}/P_{tot} = 0.1-1.0$ for 1 MW for $n_e = 10^{17}$ m^{-3}.

Bohm sheath, that the deuterium ions have enough energy to sputter out a non-negligible amount of boron, an effect that worsens with larger potentials. Conversely, there needs to be a significant enhancement in the potential for deuterium to sputter out molybdenum as seen by the "worst case" scenario in the standard dipole phasing case. Even though the molybdenum concentration is taken to be $n_{Mo}/n_e = 10^{-4}$, the amount of erosion from Mo $\rightarrow$ Mo is on the order of a few mms for the wide range of voltages due to the high sputtering yield values as seen in Appendix C. It should be noted that these erosion rates are for a low electron density (10^{17} m^{-3}). However, it is not unusual to have higher densities around the antenna surface of order $\sim 10^{18}$ - 10^{19} m^{-3} depending on the device. Since the erosion rate scales linearly with the ion density at the top of the sheath, this calculation emphasizes how deleterious near-field sheaths can be. The key takeaway from Table 4.2 is that for even low values of potential on the plasma facing components, if the material was boronized or there is some finite amount of a heavy impurity like molybdenum in the plasma, the erosion rate is noteworthy.

Chapter 5

Predictive Modeling: Far-Field Sheath Behavior in SPARC

This chapter describes how Stix is used in a predictive study of the effects of ICRF heating in the non-magnetically connected far-field sheath regime on the upcoming high field tokamak called SPARC. As mentioned in Chapter 1, far-field sheaths form due to an unabsorbed fast wave hitting plasma facing components (PFCs) such that coupling to a slow wave occurs and results in an enhanced potential. This investigation primarily focus is on how varying parameters that are directly tied to the fast wave's behavior, in particular the strength of single pass absorption through the minority ion concentration fraction and SOL densities, influence the resulting rectified voltages. Similarly, another aim of this study is to assess how problematic far-field sheaths will be for the SPARC tokamak with their baseline operating scenario.

SPARC is a high-field tokamak currently being constructed in Devens, Massachusetts by Commonwealth Fusion Systems (CFS) in partnership with the MIT Plasma Science and Fusion Center. The magnetic field on axis is 12.2 T with a major radius of 1.85 m and minor radius of 0.68 m [79]. The early campaigns will be D-D fusion with the eventual transition to D-T [79]. SPARC will solely rely on Ohmic heating and 12 ICRF antennas to reach fusion relevant temperatures on the order of Te $\sim$ 18 keV on axis in H-mode [80]. The inner vacuum vessel wall will be made of tungsten whose atomic number is 74, making it a high Z impurity if it is sputtered out of the PFCs. With such a material used, mindful attention to the sputtering flux induced when running the machine, in particular during ICRF heating will be need. The energy threshold for sputtering tungsten (W) varies with what atom is colliding with the wall but values of $\sim$ 40 eV are enough to cause sputtering if oxygen is present [74]. For the majority ion population of deuterium (D) and tritium (T), the threshold energies are higher due to light mass of these hydrogen isotopes with 220 eV

for D-W and 140 for T-W respectively [74]. With high Z impurities being a major concern for the operation of the device, this chapter will focus on a possible source of such impurities: non-magnetically connected far-field sheaths.

5.1 Previous Numerical Studies of Far-Field Sheaths

As described in Chapter 1, the focus of most numerical modeling effects of RF sheaths has been done in the near-field frame of reference. However, there have been a select few numerical cases done for the far-field regime that are limited to simple geometry. The two noteworthy studies mentioned here are D. A. D'Ippolito et. al 2013 [81] and H. Kohno et. al 2015 [65].

The primary objective of D. A. D'Ippolito et. al 2013 was numerically investigating non-magnetically connected far-field sheaths that were seen experimentally in Alcator C-Mod [38], [81]. Using a 1D model of a local far-field sheath, the role of limiter geometry through the normal component of the background magnetic field intersecting the wall was examined [81]. It was found that the tangential variation of the local magnetic field with respect to the wall plays a critical role in the strength of far-field sheath rectification [81]. This work along with the experimental results from C-Mod [38] set the precedence of including limiter-like geometry when simulating RF sheaths.

The other study to discuss is the most recent investigation of far-field sheaths done by H. Kohno et. al 2015 [65] that was an extension of D. A. D'Ippolito et. al. 2013 [81]. In this work, the cold plasma RF solver "rfSOL" was used to investigate FW propagation in an idealized circular cross-section mimicking a poloidal tokamak cross-section with a limiter bump protrusion on the "high-field side." Using a launched FW, significant rectification of order ~ 100 V was found in regions of rapidly changing magnetic field angle on the corners of the limiter bump [65]. This enhancement was due to the FW mode converting to a SW demonstrated by the parallel and perpendicular electric field components shown in H. Kohno et. al 2015 [65]. The main findings of this study were first that the mode conversion from FW to SW can occur in regions of sharp magnetic field angle variation. Additionally, increasing the toroidal mode number decreases the rectification due to widening of the FW evanescent layer, and lastly that decreasing the edge density leads to a magnetically connected far-field sheath farther from the antenna [65]. While this study provides important insight into the behavior of non-magnetically connected far-field sheaths, there are some limitations. Mainly that study is an oversimplification of a true poloidal cross-section due to the central absorption being taken to be exponentially decreasing from the "core" region and that the RF sheath BC was in the capacitive limit which is known to overestimate the rectified potentials

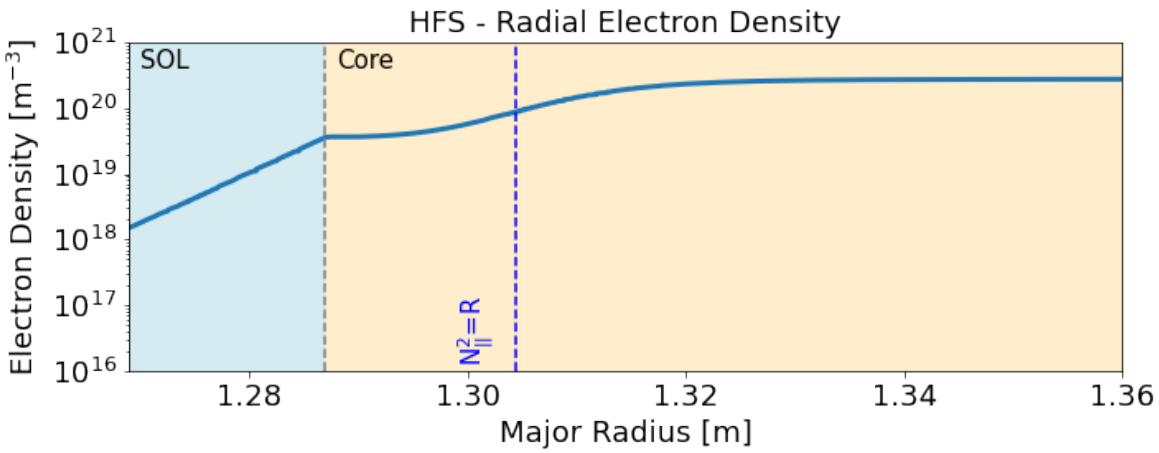

(a)

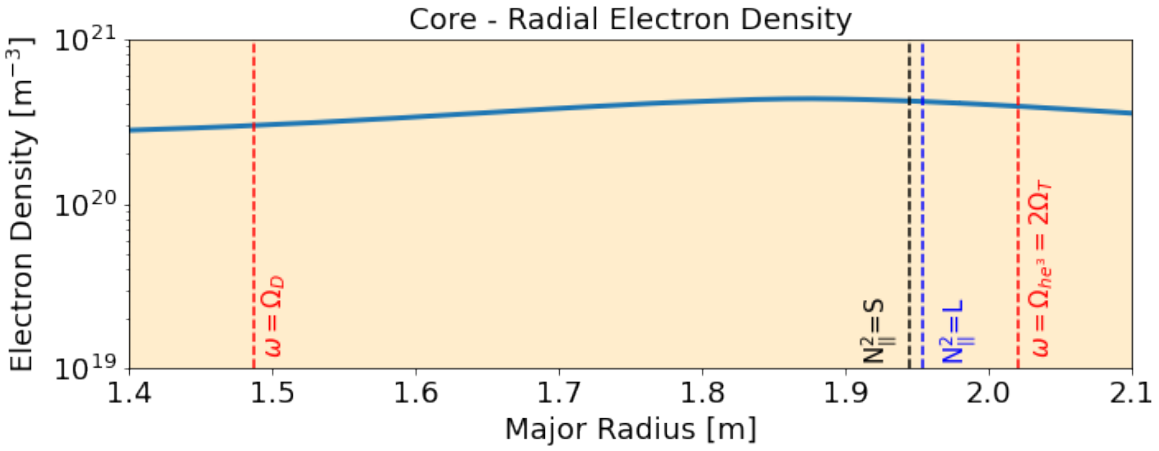

(b)

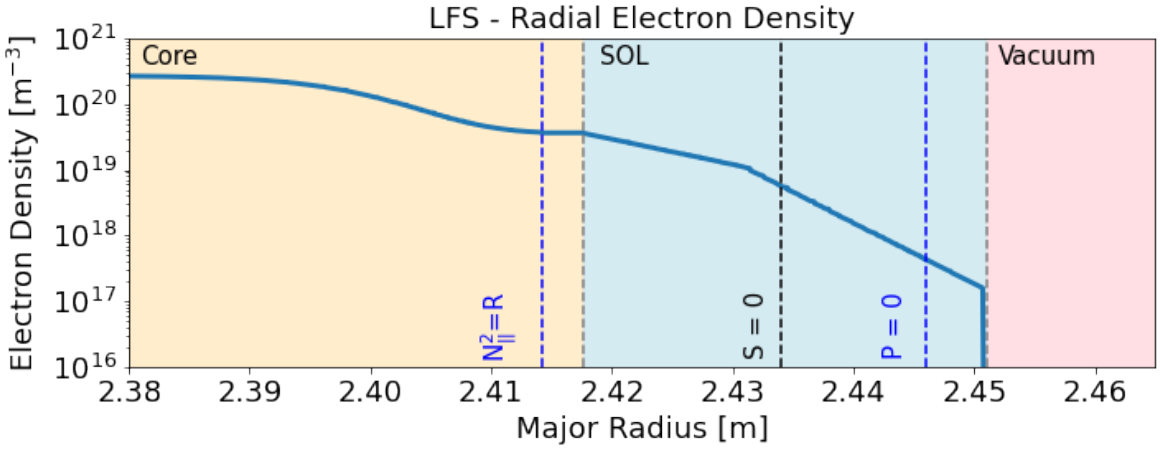

(c)

Figure 5.1: Radial electron density plots taken at Z=0 for a) the low-field, b) middle portion of the core, c) and high-field regions of the poloidal cross section. The red dashed lines indicate the wave-particle resonances, the blue dashed lines indicate the FW and SW cut-offs, and the black dashed lines show the FW and SW wave resonances.

[65].

5.2 Stix's Simulation Set-up

For these SPARC simulations, the reference frame of the poloidal cross-section was chosen with a fixed toroidal mode number, n_ϕ, taken to be 45 equating to $k_\parallel \sim 18\ m^{-1}$ at the antenna straps [57]. Due to Stix's inherent 3D nature, the toroidal direction was taken to be periodic and extruded toroidally into a 3° wedge to explicitly impose the radial effects lost due to using Cartesian coordinates in the plasma wave equation. The poloidal slice was taken to be through a toroidal wedge of the device whose (R,Z) points were sampled from a smoothed CAD of the SPARC device that included 2 ICRF antennas stacked on top of one another. Each antenna strap was set to represent the total power of each ICRF antenna taken to be 1.67 MW equating to 20.1 MW of combined power for all 12 antennas on the device [57]. The two current sources were oppositely phased and had a surface current density set to a cosine-squared profile, shown in Fig. 5.2d, peaking in the center of the strap poloidally following the field pattern found in simulations of the antennas through the RF code VSim [63]. The magnetic field was taken from an EQDSK file [67] and interpolated to fill in the values within the domain shown in Fig. 5.2a. The plasma composition consisted of deuterium and tritium with a user defined amount of helium-3 as the minority ion species. The helium concentration in the base case was taken to be $n_{He3}/n_e = 5\%$. The launched ICRF waves were taken to be at 120 MHz with a fast wave polarization.

The density profile was split into three distinct regions based on the mesh: the core, the scrape-off layer (SOL), and the vacuum region within the antenna box shown in Fig. 5.2c. For the core, the scenario chosen was that of a H-mode taken from P. Rodriguez Fernandez et. al 2022 [80] that peaked at $4.2\times10^{20}\ m^{-3}$ on axis and dropped to $8.4\times10^{19} m^{-3}$ at the last closed flux surface (LCFS). The SOL region was broken up into the high field side (HFS) and the low field side (LFS) based on differences measured in the density on the HFS and LFS of C-Mod [82]. The HFS profile followed estimates from CFS in which 1.5 cm exponential decay length was used from the LCFS to the outer limiter and 6 mm exponential decay length for regions beyond. For the HFS, a 6 mm decay length was used from the LCFS to the wall mimicking what was found on the HFS of C-Mod [82]. The last region is located right before the antenna current straps that extends to the rest of the domain on the low field side and was set to a low density of $10^{12}\ m^{-3}$ to mimic a vacuum within the antenna box. The radial electron density profile taken along Z = 0 for the low field side, Fig. 5.1a, the central core region 5.1b, and the high field side, Fig. 5.1c, highlights the three distinct regions as well as the important wave cutoffs and resonances. It should be noted that the

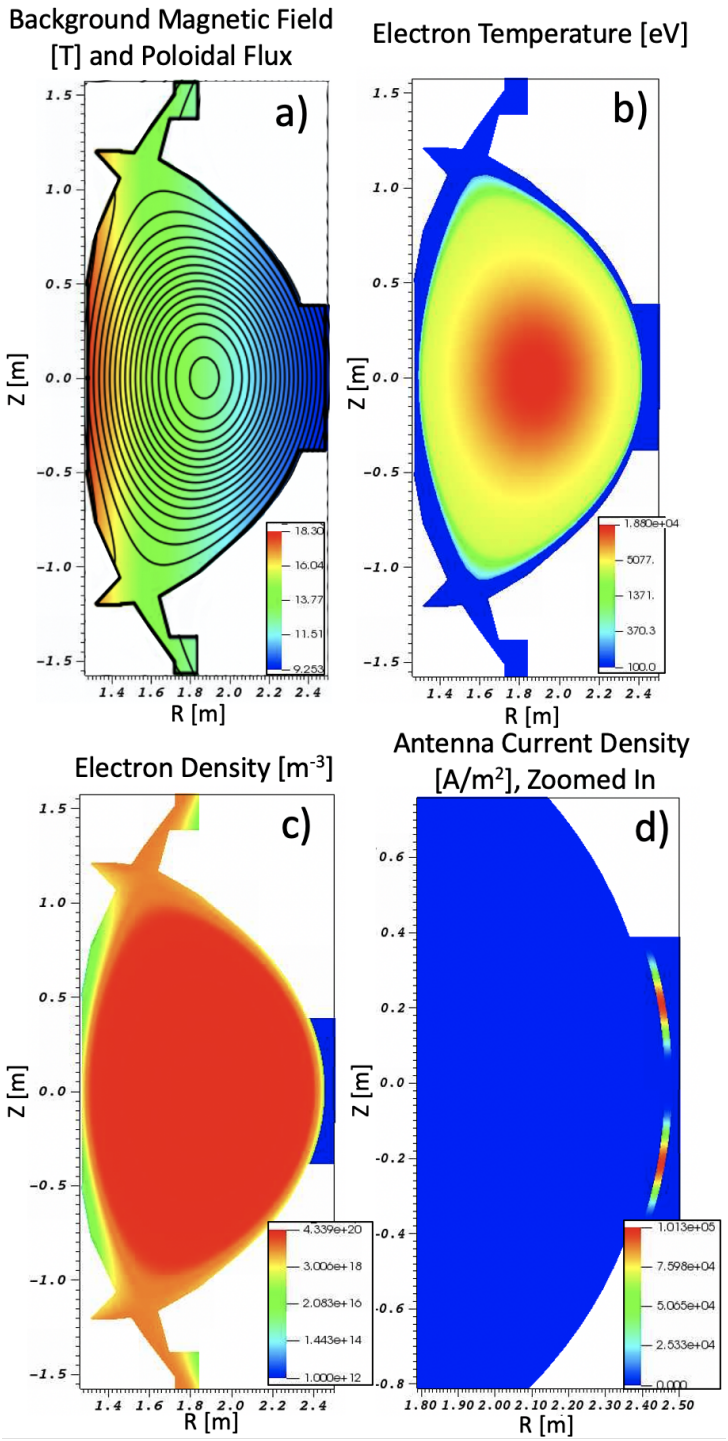

Figure 5.2: The various plasma and device parameters used in the set-up of the SPARC poloidal cross section simulations done in Stix. The magnitude of the background magnetic field along with the flux contours in shown in a). The electron temperature is shown in b) with the core values following a parameterized H-mode profile while the SOL is taken to be a constant 100 eV. The electron density is shown in c) following a parameterized H-mode profile in the core, an exponential decay in the SOL, and vacuum in near the antenna straps. The antenna current density is shown in d) following a cosine squared profile peaking at the center of the current strap.

Stix's SOL, shown in Fig. 5.2c, isn't fully representative of the true SPARC SOL in which density peaks near the divertor regions as found in transport simulations [83]. Future work can extend the electron density profile to include more realistic values near the divertors.

Figure 5.1 shows the complexity of modeling realistic SOL density profiles given the proximity of the wave cut-offs and resonances as well wave-particle resonances in the core to one another. These problematic layers pose numerical singularities in Stix due to the inversion of the plasma dielectric matrix. To resolve these resonances and cut-offs, the method of tailoring a finite amount of artificial collisionality using a Gaussian profile around the regions where they occur, the same approach described in the Chapter 4, was chosen.

It should be noted that the approach of adding artificial collisions is only used to resolve the wave resonances and cutoffs, not the wave-particle resonances which occur at $\omega = \Omega_i$ and are responsible for heating the plasma. Although adding some arbitrary imaginary component to the Stix coefficients will resolve these wave-particle resonances, given that this study was largely dependent on modeling the strength of single pass absorption of the fast wave, the method of adding the lower order kinetic effects to the cold plasma dielectric was chosen to capture the true ion cyclotron damping for the D, T, and He^3 ions. In addition, the effect of electron Landau damping was included to further capture kinetic effects in the core. These kinetic corrections are described in Chapter 2 and derived in Appendix B, repeated here for reference as

$$\begin{aligned} S = 1 - \frac{\omega_{p,e}^2}{\omega^2 - \Omega_e^2} + \frac{\omega_{p,i}^2}{\omega} \frac{e^{-\lambda}}{2k_{\|} v_{th,i}} \left[Z\left(\zeta_1\right) + Z\left(\zeta_{-1}\right) \right] \\ + \frac{\omega_{p,i}^2}{\omega} \frac{\lambda e^{-\lambda}}{2k_{\|} v_{th,i}} \left[Z\left(\zeta_2\right) + Z\left(\zeta_{-2}\right) \right] \end{aligned} \tag{5.1}$$

$$\begin{aligned} D = \frac{\Omega_e}{\omega} \frac{\omega_{p,e}^2}{(\omega^2 - \Omega_e^2)} - \frac{\omega_{p,i}^2}{\omega} \frac{e^{-\lambda}}{2k_{\|} v_{th,i}} \left[Z\left(\zeta_1\right) - Z\left(\zeta_{-1}\right) \right] \\ - \frac{\omega_{p,i}^2}{\omega} \frac{\lambda e^{-\lambda}}{2k_{\|} v_{th,i}} \left[Z\left(\zeta_2\right) - Z\left(\zeta_{-2}\right) \right] \end{aligned} \tag{5.2}$$

$$P = 1 - \frac{\omega_{p,e}^2}{k_{||}^2 v_{th,e}^2} Z'\left(\zeta_0\right) - \frac{\omega_{p,i}^2}{\omega^2} \tag{5.3}$$

Here it is assumed that $k_{\|} = n_{\phi}/R$ with the poloidal mode of m=0. Using the plasma dispersion function, $Z(\zeta_n) = Z(\frac{\omega - n\Omega}{k_{\|} v_{th}})$, requires an electron temperature profile due to the ion thermal velocity term in the above equations. A parameterized electron temperature was taken through P. Rodriguez Fernandez et. al 2022 [80] for the same H-mode scenario

that the electron density follows, displayed in Fig. 5.2b. The peak electron temperature was 18 keV on axis and dropped to 289 eV at the LCFS. The SOL temperature was taken to be a constant value of 100 eV, which collapses the kinetic corrected dielectric back to the cold plasma values. Lastly, the temperature at the plasma domain walls was taken to be a constant 10 eV.

5.3 Comparison of Hot vs. Cold Plasma with Kinetic Corrections for SPARC

To give confidence that adding lower order kinetic corrections to the cold plasma dielectric is enough to capture the wave-particle resonance, a comparison to the hot plasma RF solver called TORIC was first done. The TORIC code solves for the electric field of a launched RF wave within the core region of a poloidal cross section using the full kinetic plasma dielectric, given by Eq. 2.32 in Section 2.3 [84]. It is a finite-element code in the radial direction and spectral code in the poloidal direction allowing for multiple poloidal modes. Due to its spectral nature, the domain only includes the closed field line region of the poloidal cross-section and therefore to add a scrape-off layer the LCFS of the plasma must be displaced inward through user specification.

The simple test case of one ICRF antenna centered at Z = 0 with a length of 32.5 cm was chosen for both TORIC [85] and Stix. For both codes the same H-mode electron density and temperature profiles were used, the SOL was taken to be vacuum, the toroidal mode number was set to 45, and both codes used 1 MW of coupled RF power. There are some noteworthy differences between the two solves: 1) the distance between the antenna current strap and the LFCS, 2) the antenna currents in the both codes had different poloidal variations, 3) the background equilibrium files have different magnetic axis locations, and 4) TORIC includes kinetic effects that are not included in Stix. The distance between the LCFS and the antenna current strap in the Stix simulations is taken to be the actual value of 3.23 cm, whereas TORIC's distance is 7 cm. This difference in SOL layers means that for the larger SOL layer the launched wave must tunnel through a longer evanescence layer and therefore lose more of its amplitude before reaching the plasma which becomes more apparent when comparing the electric field line-outs between the two codes. Additionally, Stix's antenna current was taken as a flat current profile while TORIC's had the current peak in the center of the strap poloidally therefore changing the focusing of the launched wave. The background magnetic fields have a 2 mm difference in the magnetic field axis due to how the codes process the equilibrium from the EQDSK causing the wave's electric

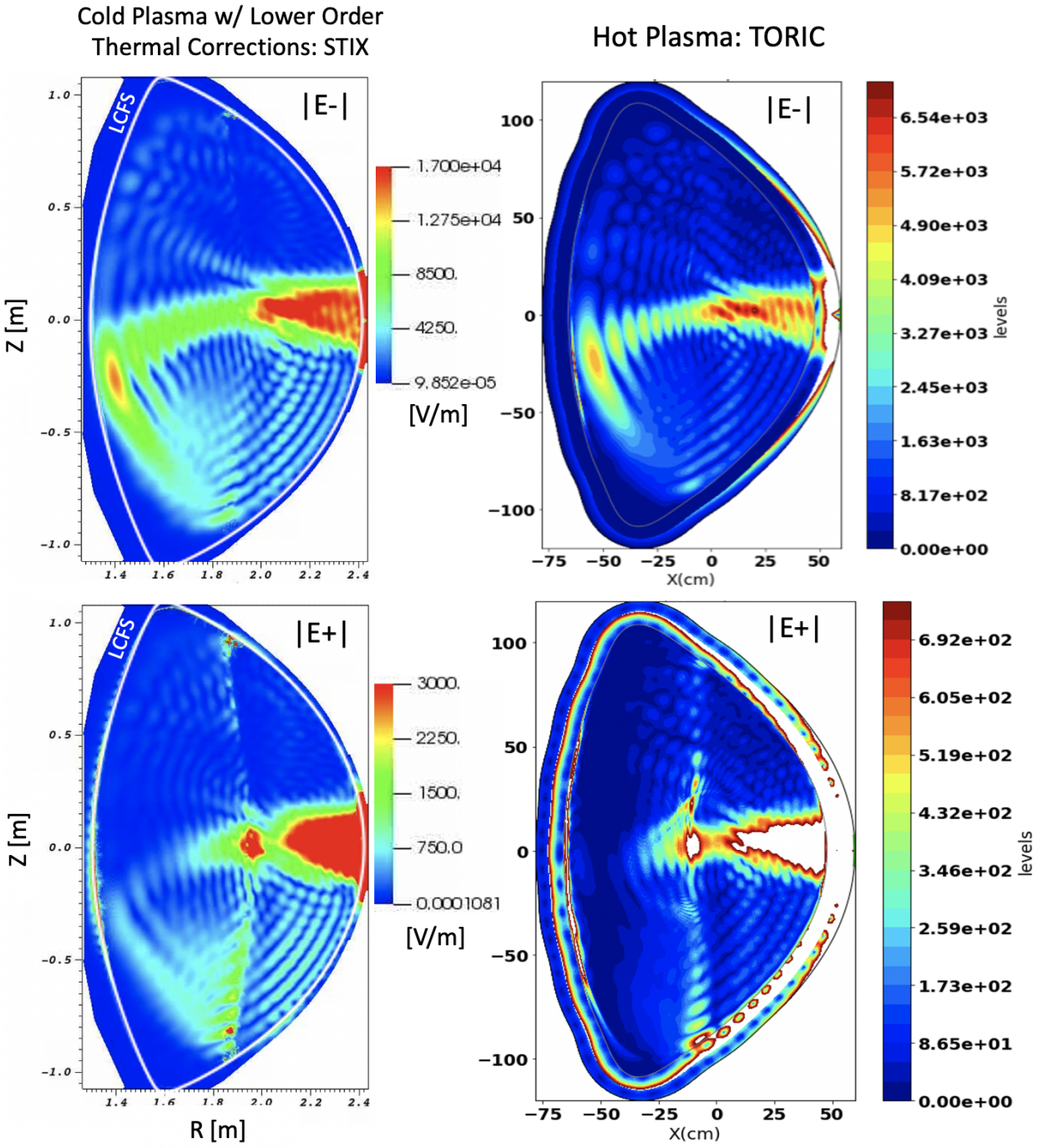

Figure 5.3: The comparison of the 2D poloidal cross section electric field polarizations, E_+ and E_-, for Stix with thermal corrections (left column) and the hot plasma RF solver, TORIC (right column). This case is done using 1 antenna centered at Z = 0 using a constant antenna current density profile. The core is represented using electron density and temperature from a H-mode parameterization while the SOL is set to be a vacuum. Note that the white regions of the electric field plots from TORIC represent values larger than the colorbar's maximum value.

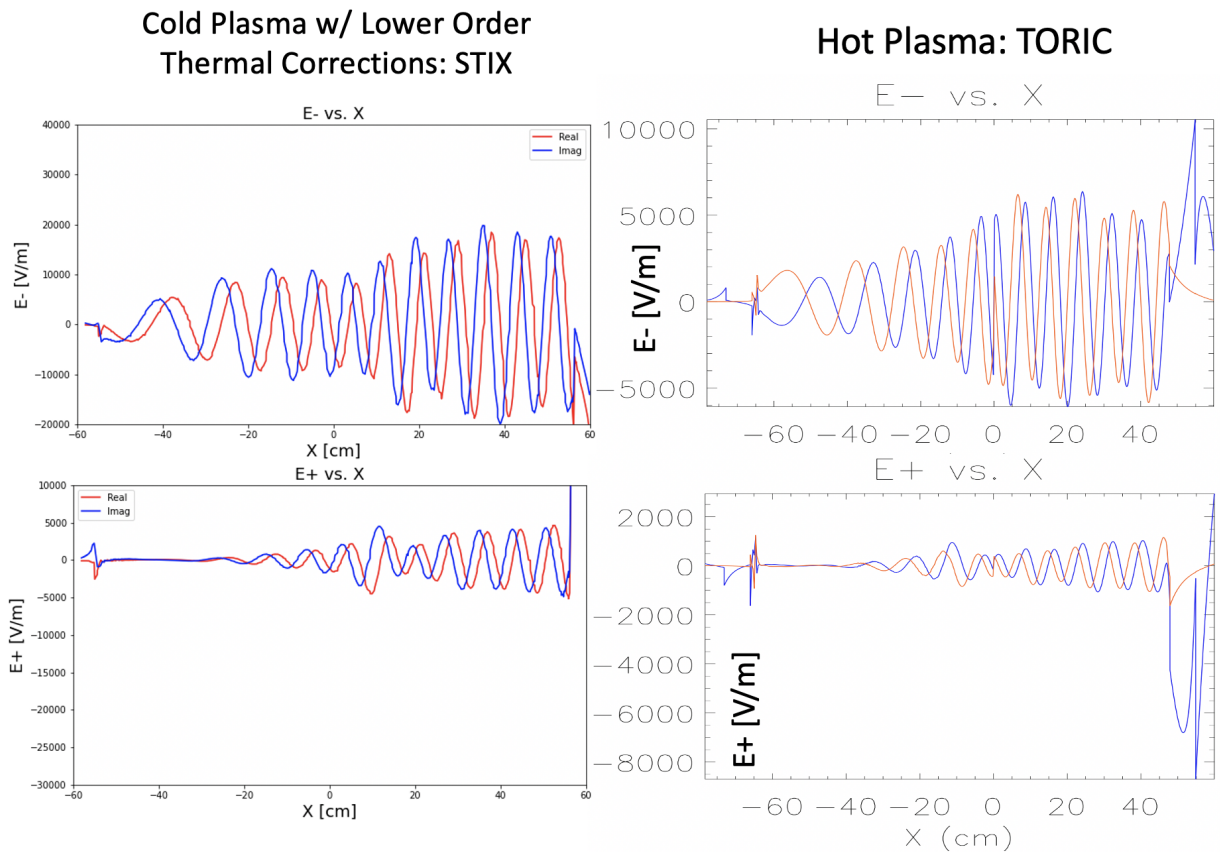

Figure 5.4: Comparison of the real and imaginary components of the E_+ and E_- electric fields from thermally corrected Stix (left column) and TORIC (right column). The red and blue curves correspond to the real and imaginary electric field component respectively.

fields to be shifted from one another. Lastly, one needs to mention that TORIC is a fully kinetic code that includes the effect of kinetic mode conversion to ion Bernstein waves and ion cyclotron waves, which can only be modeled accurately with finite poloidal mode number (typically |m| $\sim$ 200).

Figure 5.3 shows the 2D electric field plots for the magnitude of E_+ and E_-. The Stix code is represented in the left column while the TORIC code is displayed in the right column. It should be noted that the colorbar units are not the same for the two codes, Stix's are in SI units of V/m while TORIC's is normalized to $(\mathrm{V/m})/\sqrt{MW/m^3}$. From Fig. 5.3 it is seen that the two code's wave propagation pattern follow closely to one another. Similarly, Fig. 5.4 compares line-outs of the real and imaginary E_+ and E_- taken at Z=0 along the major radius from both codes. Here the real component is in red while the imaginary component is in blue. From these plots, one can see good qualitative agreement in the wave patterns however the amplitudes for the Stix fields are somewhat larger than TORIC's. This discrepancy can be attributed to the difference in the SOL layer thickness for both codes and the antenna current profiles of each codes. Given that TORIC's SOL is twice as wide as Stix's, the launched wave spends more time in the evanescent layer and therefore loses more of its amplitude as it reaches the plasma.

5.4 Far-Field Sheath Stix Simulations of SPARC

The following sections describe the various far-field sheath simulations for the poloidal cross-section of the SPARC tokamak. First, the baseline scenario in H-mode using 5% helium-3 minority is examined. Next, the relationship between varying the minority concentration to change the amount of single pass absorption is investigated to see its effect on the strength of rectification. The role of the SOL density is then varied to see its effect. Lastly, following H. Kohno et. al 2015 [65], limiter bumps are placed all along the vacuum vessel to see how influential the role of the magnetic field into the wall is on rectification.

The knob chosen to represent the strength of single pass absorption for the fast wave in these simulations is taken to be the percentage of the minority ion species which is helium-3 for SPARC. In the minority ion heating scheme, a dilute ion species is added to the majority so that the fast wave now acquires a left-hand circularly polarized component that can interact with the minority ion species and damp on that species via ion cyclotron damping. ICRF wave absorption is dependent on the minority ion plasma frequency and therefore by the square root of the minority ion's density [86]. Increasing the percentage of minority ions therefore increases single-pass absorption up to a certain value before the absorption regime shifts to an entirely different regime known as ion-ion hybrid mode conversion [86].

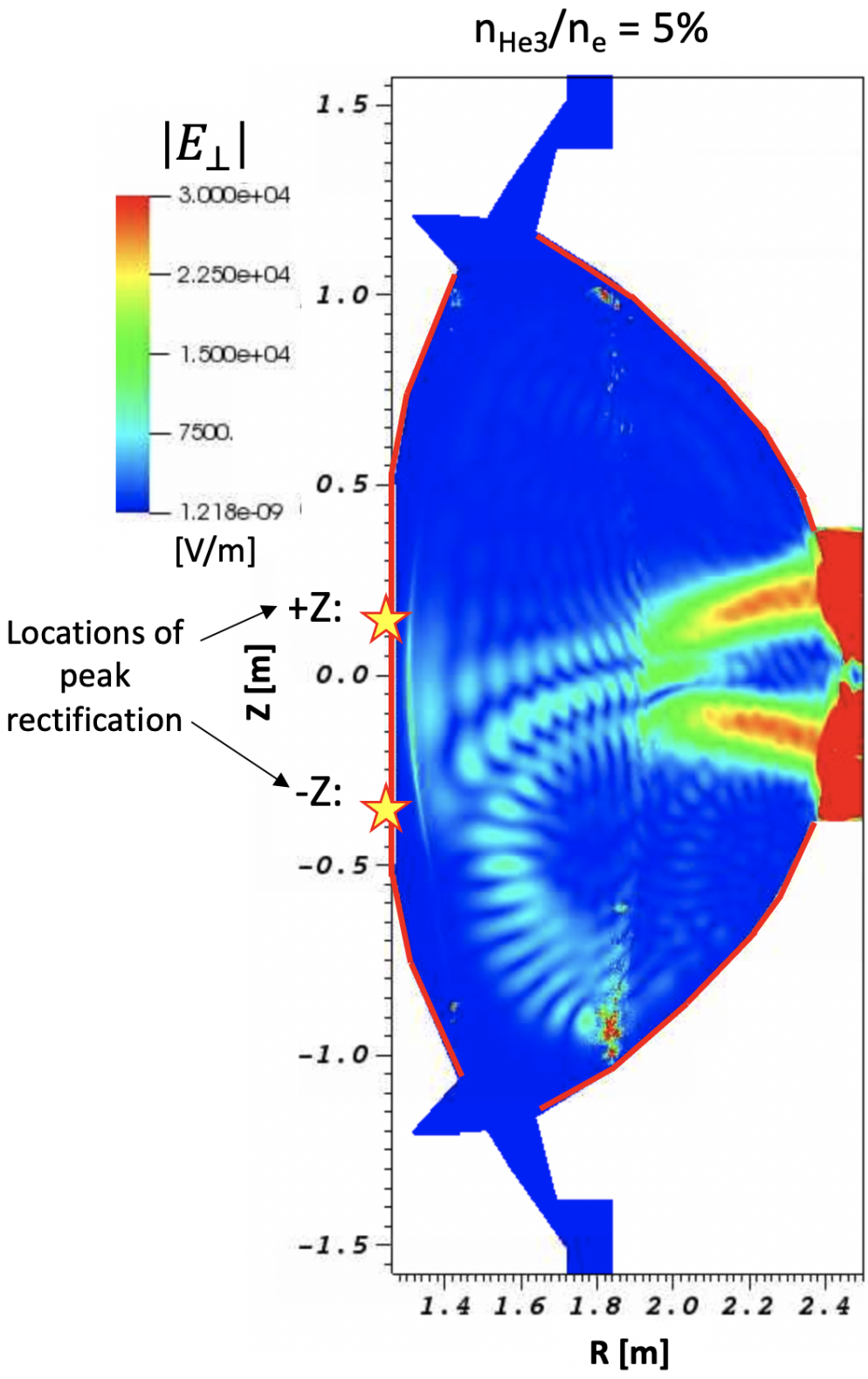

Figure 5.5: 2D color-plot of the magnitude of the perpendicular electric field for the baseline He^3 = 5% H-Mode plasma scenario of SPARC. The red border along the vacuum vessel indicates the domain walls where the RF sheath BC was placed.. The two yellow stars show the location of the peak rectification found to be on the high-field side and are referred to in the text as "+Z" and "-Z."

For all these cases, the core electron density and temperature profiles, the antenna current, the SOL and wall electron temperatures, the background magnetic field, and the SOL density (expect for Section 5.4.3) were kept the same. Each simulation used the maximum number of elements possible of 4.5×10^6 in the 2D poloidal frame within the memory limits of the direct solver MUMPS and used order 1 polynomials.

5.4.1 Baseline H-Mode Flattop Scenario

The baseline $n_{He3}/n_e = 5\%$ H-mode scenario plasma parameters are those described in Section 5.2. This minority concentration corresponds to high single pass absorption ($> 90\%$) which is seen in the resulting perpendicular electric field magnitude, $|E_\perp|$, in Fig. 5.5. Here and in the remaining sections the plots of $|E_\perp|$ will serve as the proxy to represent the FW since the FW consists primarily of $|E_\perp|$.

The regions of the domain wall that included the RF sheath BC are shown by the red line segments in Fig. 5.5 in which the divertors and antenna box are excluded. Although the BC was placed along the low field side of the device, much of this region did not meet the minimum angle of sheath formation criterion [20], repeated here as

$$b_n = \cos\Psi > \sqrt{m_e/m_i} \sim 1^\circ \tag{5.4}$$

This resulted in the largest enhancement of potentials occurring on the high-field side of the device. The two points reported here are chosen as the largest voltage value above and below the Z = 0 mid-plane referred to as "+Z" and "-Z" respectively, shown in Fig. 5.5. It was found that +Z = 32.19 V and -Z = 32.37 V for $V_{peak} = |V_{RF}| + V_{REC}$. These values are negligible rectification when compared to the 31.86 V thermal Bohm sheath for this case. The primary reasons for such small values in this case are due to the high single pass absorption, i.e. there isn't much FW electric field on the HFS and therefore no source of rectification, and the normal component of the magnetic field angle is very small into the PFC as shown in Fig. 5.6. It is seen in Fig. 5.6 that a majority of the vacuum vessel wall does not meet the minimum sheath formation angle of 1° as indicated by the values left of the red solid line. This result is not surprising given the fact that the toroidal magnetic field component is much larger than the poloidal component of the magnetic field. Similarly, the toroidal component has no normal contribution into the wall in this poloidal reference frame.

It should be noted that even though the RF sheath BC is invalid following Eq. 5.4, physically there still is a sheath. The RF sheath boundary condition is derived from non-linear fluid equations and therefore do not account for finite Larmor effects (FLR). FLR effects need to be included for grazing magnetic field angles due to the Larmor orbit width

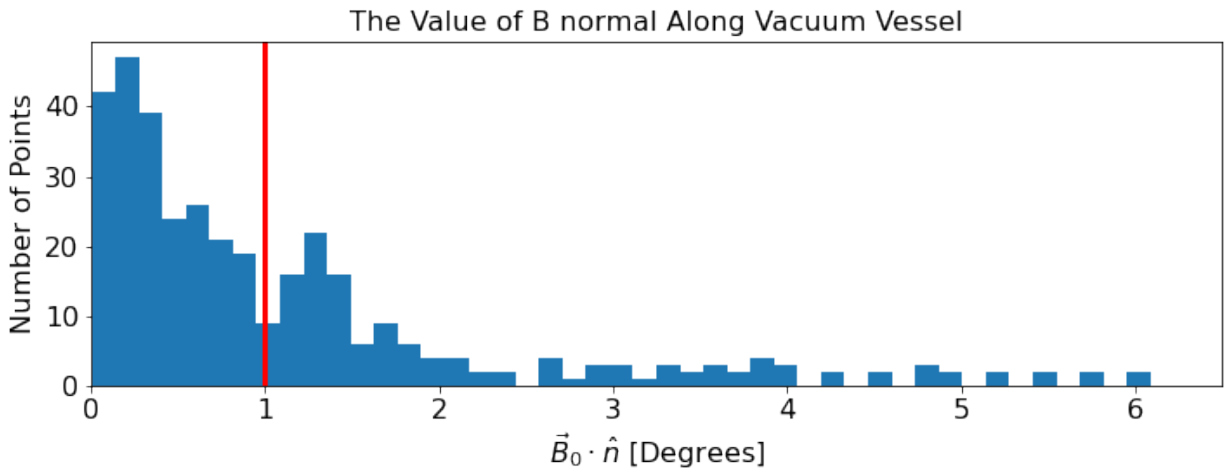

Figure 5.6: Histogram of the various values of the normal component of the background magnetic field with respect to the domain wall. The solid red line indicates the minimum angle of sheath formation where the values to the left are invalid to apply the RF sheath BC. This plot includes all VV values including the divertors and antenna box where the b_n are larger but where the RF sheath BC was not placed.

being comparable to the sheath width [20]. However, it is expected that including kinetic, non-neutral, and transport effects to account for grazing angles will have a minimal effect on the sheath rectification in this case [20].

5.4.2 Scanning Various Core Absorption Regimes

With the baseline case established, the question of what role does the strength of single pass absorption play in the amount of rectification was investigated. For this study, 7 different helium-3 minority ion concentrations were chosen, varying from multi-pass to high single pass absorption: $0.01\%, 0.05\%, 1\%, 2\%, 3\%, 4\%, 5\%$. Additionally, this study aimed to look at what percentage of helium-3 does the regime switch from single pass to multi-pass absorption.

To get a sense of how sensitive single pass absorption is with minority ion fraction, Fig. 5.7 gives a measure of how the power (normalized) changes with respect to the major radius. This measure of power was found by taking 50 equally distanced vertical slices along the major radius and sampling the real component of the Poynting flux normal to the vertical slice, visualized by Fig. 5.8. This Poynting flux was then integrated and multiplied by the radial location of the slice to get units of Watts, given as

$$\frac{1}{2}\int_{-Z}^{+Z} Re[\vec{S}\cdot\hat{R}]R\ dZ \tag{5.5}$$

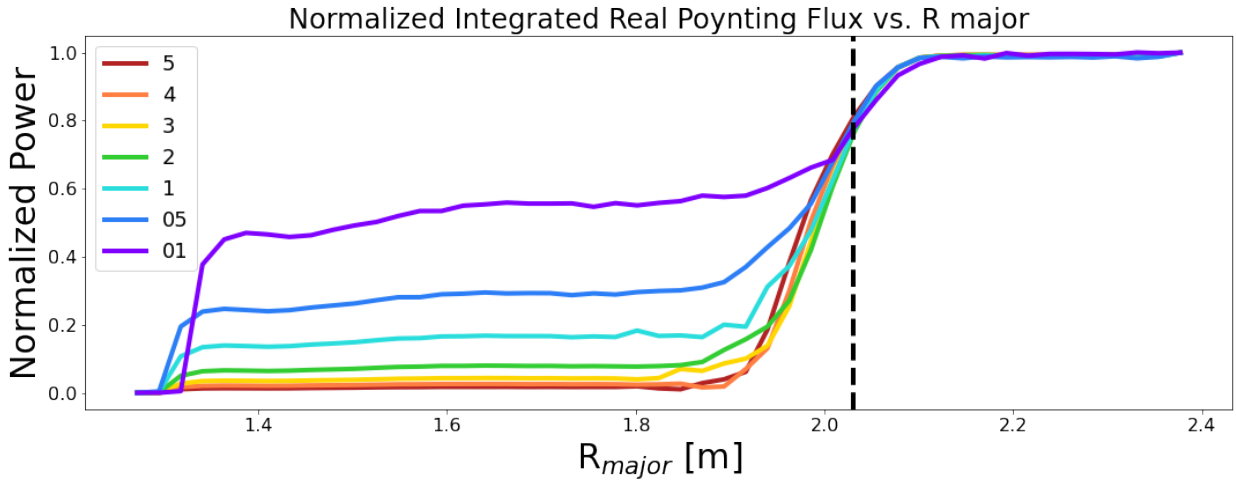

Figure 5.7: The projection of the normalized integrated real component of the Poynting flux in the major radius direction, $\vec{R}$, taken for 50 radial slices from the poloidal cross section for the various helium-3 concentration amounts. The grey vertical dashed line indicates the helium-3 cyclotron resonance. It is seen that there is a significant jump of power reaching the high field side going from 2% to 1% helium-3 concentration.

Fig. 5.7 shows that for cases $2\%, 3\%$,4%, and 5% the power deposition is similar in amplitude. This is an expected result given that there exists a threshold for the minority concentration in which the single pass absorption plateaus until eventually one increases the fraction too high and encounters the ion-ion mode conversion regime, not represented in Stix. This plot suggests that the transition from 2% to 1% helium-3 concentration gives rise to a drastic increase in the undesirable effect of more power propagating to the high-field side. In contrast, having a higher fraction of helium-3 is also not ideal given that it is an expensive resource and is undesirable for plasma confinement. Therefore, somewhere in the range of $3\% - 5\%$ gives an optimal amount of single pass absorption in line with the suggested baseline scenario.

With the RF sheath BC included, the 7 concentration cases were run. Like the baseline scenario, the two largest peaks, one above and one below the Z = 0 mid-plane were chosen to represent each scenario's strength of rectification. Due to the magnetic field angle on most of the LFS wall not satisfying the condition for application of RF sheath BC, peak rectification values were only found on the HFS. Fig. 5.10 shows the maximum peak voltage defined as $V_{peak} = |V_{RF}| + V_{REC}$ for both +Z and -Z along with the thermal Bohm sheath indicated by the grey dashed line. From this plot, one can see that even in the case where the single pass absorption is very low and therefore there is significant power reaching the HFS, the sheath voltage values are still small. This suggests that the small b_n on the HFS plays a notable role in rectification strength. This idea is further tested by artificially adding bumps

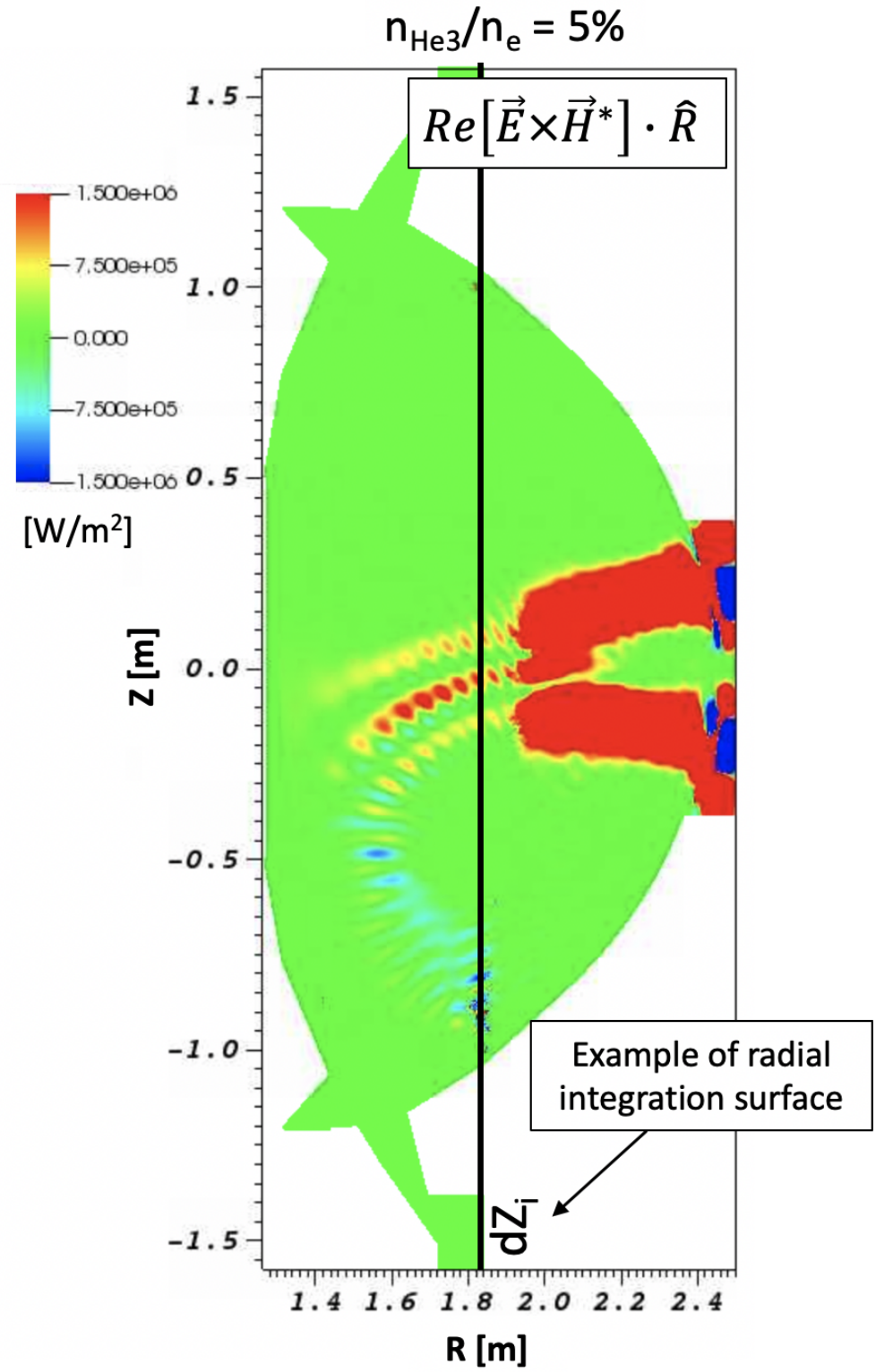

Figure 5.8: 2D plot of the major radial component of the real Poynting flux, $Re(S_R)$. The red field indicates power moving to the high field side while the blue field represents power moving back towards the low field side. One can measure the coupled power value by integrating along the surfaces of constant major radius, an example of which is shown by the black line.

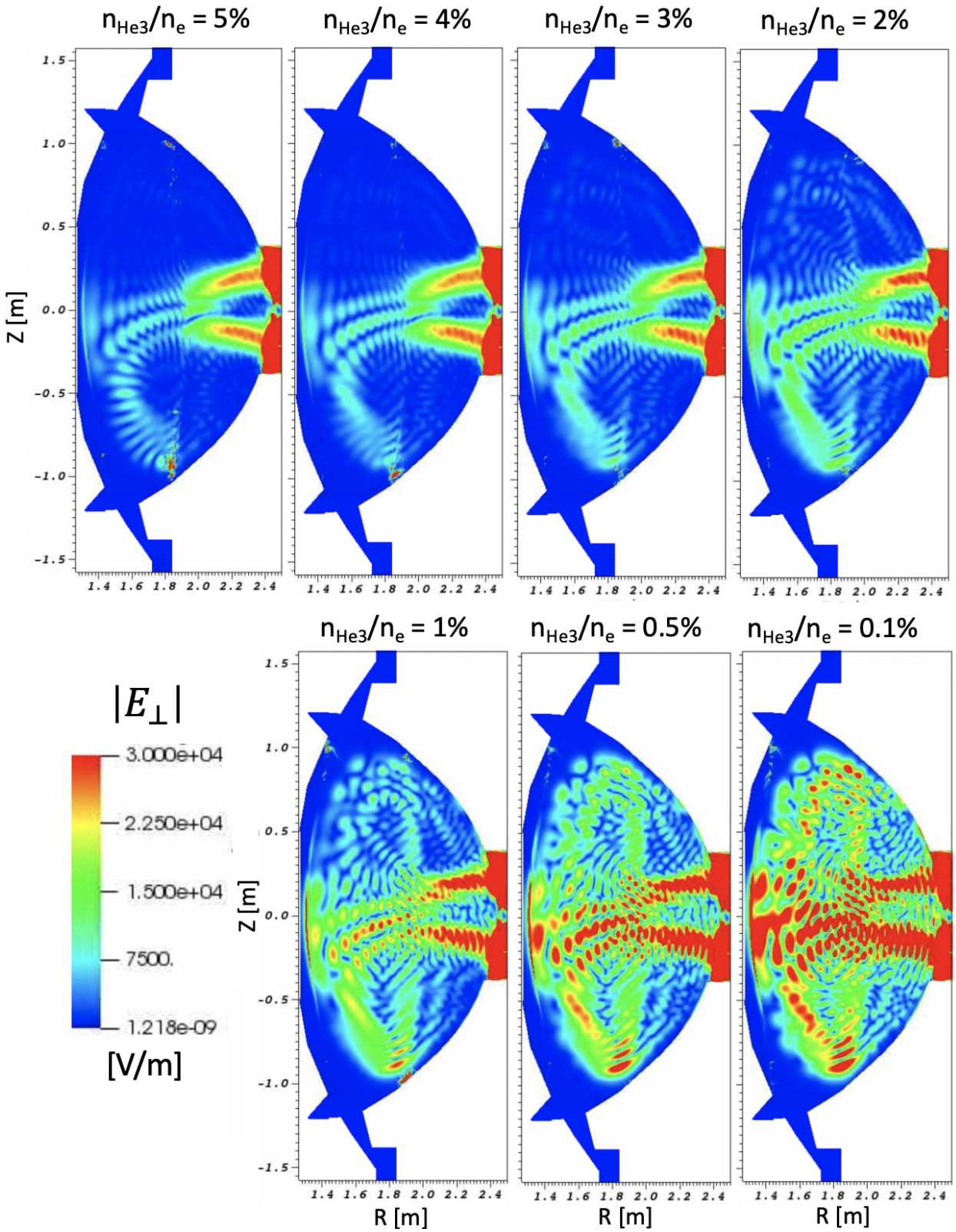

Figure 5.9: The magnitude of the perpendicular electric field, $|E_\perp|$, for helium-3 concentration amounts varying from $n_{He3}/n_e = 0.1\%$ to 5%. It is seen that as n_{He3}/n_e decreases the amount of single pass absorption decreases with the notable decline in the absorption strength from 2% to 1%.

along the wall to force a larger b_n which is described later in Section 5.4.4. Fig. 5.9 shows the corresponding magnitudes of the perpendicular electric fields for each concentration and are seen to agree with the results of the power deposition from Fig. 5.7 showing a noticeable shift in the strength of the electric field on the LFS between 2% to 1%.

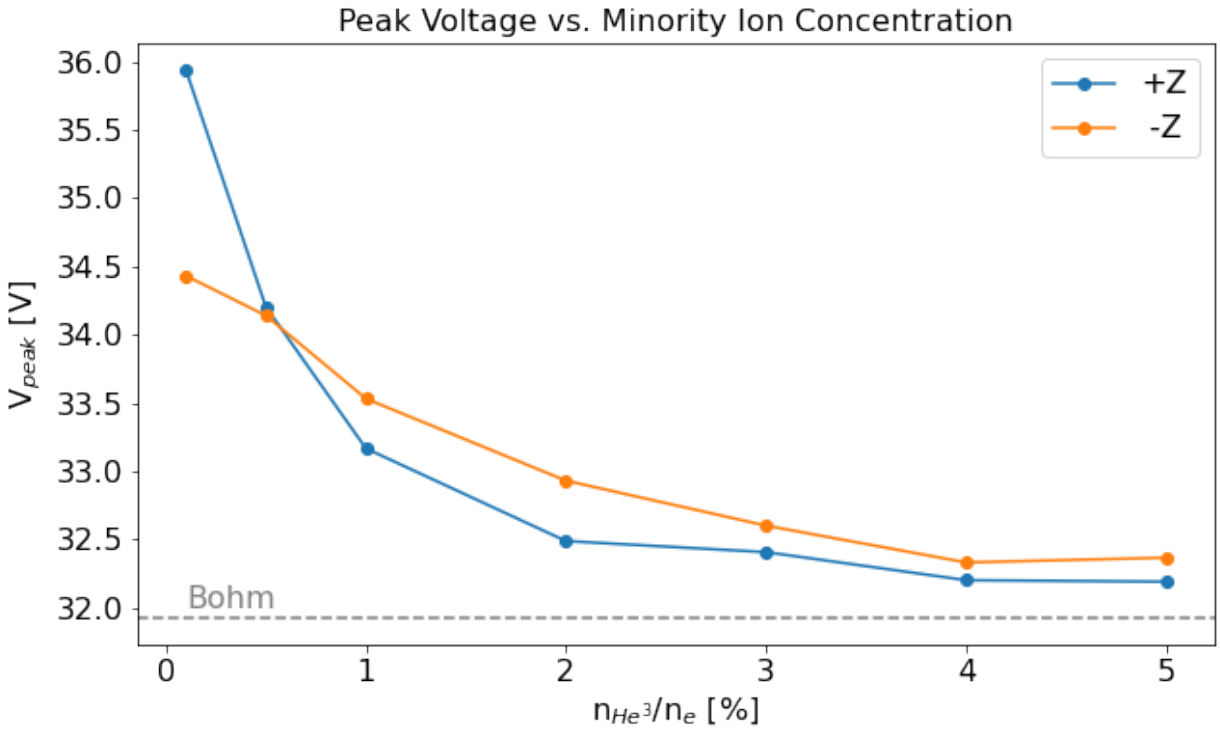

Figure 5.10: Plot of the maximum peak voltage, $V_{peak} = |V_{RF}| + V_{REC}$, for varying helium-3 concentration amounts taken from the top, +Z, high field side (blue) and bottom, -Z, high-field side (orange). The thermal Bohm sheath of 31.86 V is indicated as the grey dashed line.

Lastly, the amount of power dissipated in the sheath was calculated for each of the 7 concentration cases shown in Fig. 5.11. These values were found by adapting the classic power of a circuit formula of $P = V^2/R$ to be [53]

$$P_{sh} = \sum_k \frac{1}{2}|V_{RF}|^2 \Delta_{sh} \sum_{j=i,e} Re[y_{sh,j}]\ dS_k \tag{5.6}$$

Here, at each wall section, k, the values of electron and ion sheath admittance are multiplied by the local sheath width and the inner product of the local AC component of the sheath potential magnitude, $|V_{RF}|$. This is then summed over all the wall sections to get power dissipated in units of Watts per meter. Fig. 5.11 shows the resulting global power per meter dissipated in the sheath for each concentration and demonstrates that there is no significant

power being dissipated in the far-field sheaths. This result follows what is expected given the low RF voltages found due to the scaling with $|V_{RF}|^2$ while not including the DC component (V_{REC}) that is of order of the Bohm sheath.

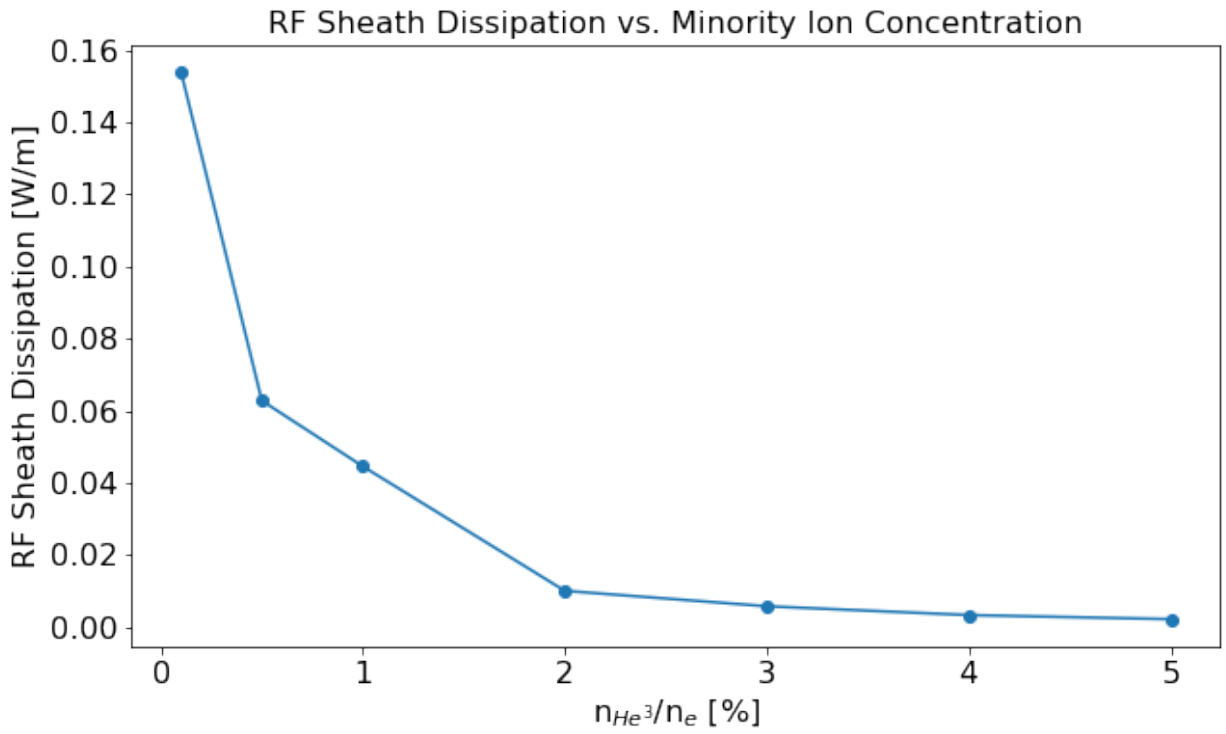

Figure 5.11: The calculated RF sheath dissipation power per unit length for varying helium-3 concentrations.

5.4.3 Varying SOL Density Profiles

Here it is described how varying the scrape-off layer (SOL) density profile changes the rectification for the 3% helium-3 scenario. For this study, 3 different decay length scenarios were chosen in which the core density was kept constant while two regions in the SOL were varied: the region between the LCFS and the outer limiter labeled λ_1 and the region between the outer limiter and the antenna strap labeled λ_2. It should be noted that the region behind the antenna straps was set to vacuum for all the density cases. Fig. 5.12 illustrates the variation of the three cases. Here the base case is from the baseline scenario of $\lambda_1 = 1.5$ cm and $\lambda_2 = 0.6$ cm, Case 1 has $\lambda_1 = 2$ cm and $\lambda_2 = 0.7$ cm, and lastly Case 2 has $\lambda_1 = 4$ cm and $\lambda_2 = 1.3$ cm. Case 1 and Case 2 correspond to raising the densities at the edge moving the SW's lower hybrid resonance closer to the antenna giving less room for a propagating SW in this region. The FW cut-off is not affected by this change in SOL density due to it occurring

near the pedestal region of the core, about 7 mm from the LCFS as shown by Fig. 5.1c.

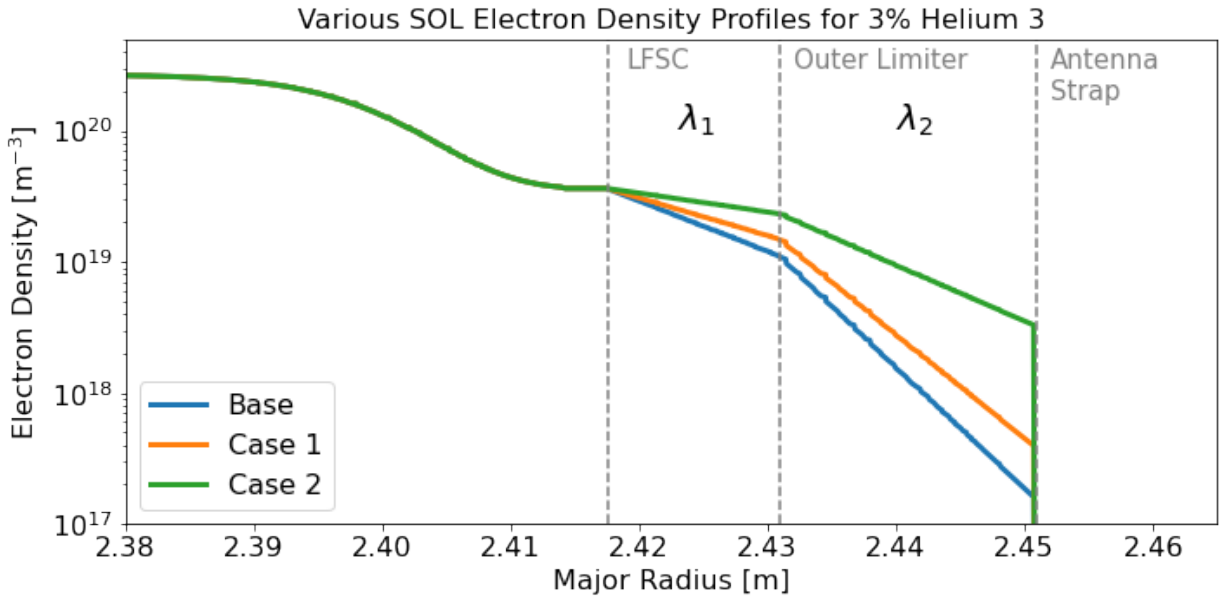

Figure 5.12: Radial plot along Z = 0 of the various SOL electron densities on the low field side for the $He^3 = 5\%$ case. The baseline density parameterization is shown by the blue line corresponding to a decay length of 1.5 cm for λ_1 and 6 mm for λ_2. Case 1 corresponds to a decay length of 2 cm for λ_1 and 7 mm for λ_2. Case 2 corresponds to a decay length of 4 cm for λ_1 and 1.3 cm for λ_2. The electron density past the antenna current straps is taken to be a low density value of 10^{12} m^{-3} to mimic a vacuum region and the core density is kept the same for all three cases.

As in the far-field simulations described earlier in this section, the two largest peaks above (+Z) and below (-Z) the Z=0 mid-plane on the high field side were chosen to represent the rectification of each case. Table 5.1 shows the resulting enhanced potentials. Seen in this data is that as the density increases at the edge, the rectification decreases. However, these values are so small when compared to the 31.86 V thermal Bohm sheath that one cannot infer if there is a relation between SOL density and far-field rectification. A different reference frame in which more of the low-field side is represented such as a top-down view of the antenna would provide more insight into this relationship and is left for future work.

5.4.4 Limiter Bump Case

The last case investigated in this SPARC study is the effect of the magnetic field angle into the wall. It is seen in previous literature that a rapidly changing angle plays a consequential role in the strength of the rectification [38], [65], [81]. Therefore, this study aimed to look at this effect in a realistic poloidal cross-section and to see whether this is the driving force

	V_{peak}: +Z [V]	V_{peak}: -Z [V]
Base $\lambda_1 = 1.5$ cm $\lambda_2 = 0.6$ cm	32.41	32.6
Case 1 $\lambda_1 = 2.0$ cm $\lambda_2 = 0.7$ cm	32.19	32.22
Case 2 $\lambda_1 = 4.0$ cm $\lambda_2 = 1.3$ cm	32.09	32.01

Table 5.1: The enhanced potentials for varying the SOL density profile measured above (+Z), below (-Z) and at the mid plane (Z=0). It is seen that although there is some slight variation in the values they are still very small.

as to why the enhanced potentials even in the worst absorption scenarios resulted in small voltages.

To artificially add more of a normal component of the background magnetic field to the poloidal cross-section, smooth limiter-like bumps are added following [65] to all four quadrants of the cross-section: top and bottom of both the low and high field sides. The chosen locations of the bumps were based on the plot of the $|E_\perp|$. The regions where $|E_\perp|$ was largest and closest to the wall were the prime locations to observe the FW to SW far-field sheath mode conversion. The bumps were parameterized as

$$bump(x) = \frac{h_{bump}}{2}\left[\left(1 + \tanh\left(\frac{x - x_1}{\delta x}\right)\right) - \left(1 - \tanh\left(\frac{x - x_2}{\delta x}\right)\right)\right] \tag{5.7}$$

where h_{bump} gives the height of the bump and δx gives the sharpness of the angle following [65]. Given that SPARC's SOL is so thin, the protrusion of the limiter bumps was chosen to vary between h_{bump} =1 to 1.8 cm into the plasma in order to not intersect the LCFS. Fig. 5.13 shows an example of how this artificial protrusion warps the vacuum vessel (VV). This plot represents a zoomed in view of the top low-field side portion of the cross-section. The original wall is plotted in red versus the parameterized limiter bump wall in blue. Here the 2D poloidal component, decomposed into the $\hat{R}$ and $\hat{Z}$, background magnetic field is over-plotted against the VV walls. This figure shows that a limiter-like bump results in a significantly larger fraction of the poloidal magnetic field being normal to the wall. It should be noted that this region of the VV in the original coordinates had too small of b_n to apply the RF sheath BC which is seen by how tangential the poloidal magnetic field vector is to the red line.

Figure 5.14 shows the plot of $|E_\perp|$ with the modified VV walls along with the corre-

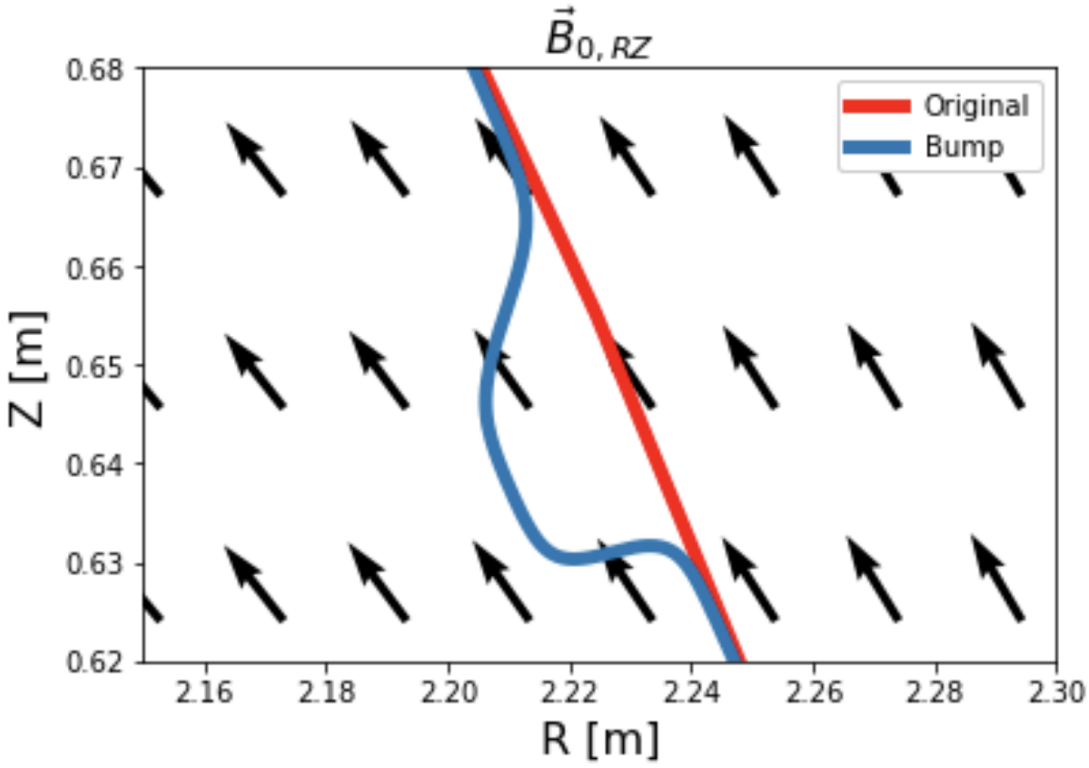

Figure 5.13: Vector field of the $\vec{R}$ and $\vec{Z}$ components of the background magnetic field overlaid onto a section of the vacuum vessel (VV) wall. The red line indicates the original VV wall while the blue line indicates the same VV wall with the inclusion of a limiter bump. The original VV wall shows near tangency of the magnetic field while the VV with the bump allows for more of the poloidal magnetic field to intersect the wall, increasing the angle of the magnetic field, b_n, into the wall and therefore increasing the likelihood of rectification.

sponding magnitude of the RF sheath potential (AC component only). This simulation was arbitrarily chosen to be a lower absorption case of 0.5% helium-3. For comparison, the original VV simulation at the same concentration had the largest rectification occurring on the HFS (due to the LFS having too small of a magnetic field angle) and was about $\sim$ 34 V for V_{peak}. Adding limiter bumps produced three distinct regions of rectification shown in a), b), and c) of Fig. 5.14. In this case, the largest voltages occurred on the LFS shown in a) with $V_{peak} \sim 77.97$ V for the voltage values shown in red. Similarly, b) $V_{peak} \sim 38.4$ V, region c) had $V_{peak} \sim 47.43$ V. The color scale of $|V_{RF}|$ in a), b), and c) are different from one another to show each region's specific peak voltages. With the inclusion of these bumps, the effect of the magnetic field angle shows a clear influence on resulting enhanced potential.

Even with the limiters added, the b_n in this 2D poloidal simulation was still relatively small, of order 5%, due to the strength of the toroidal magnetic field. This brings forth the

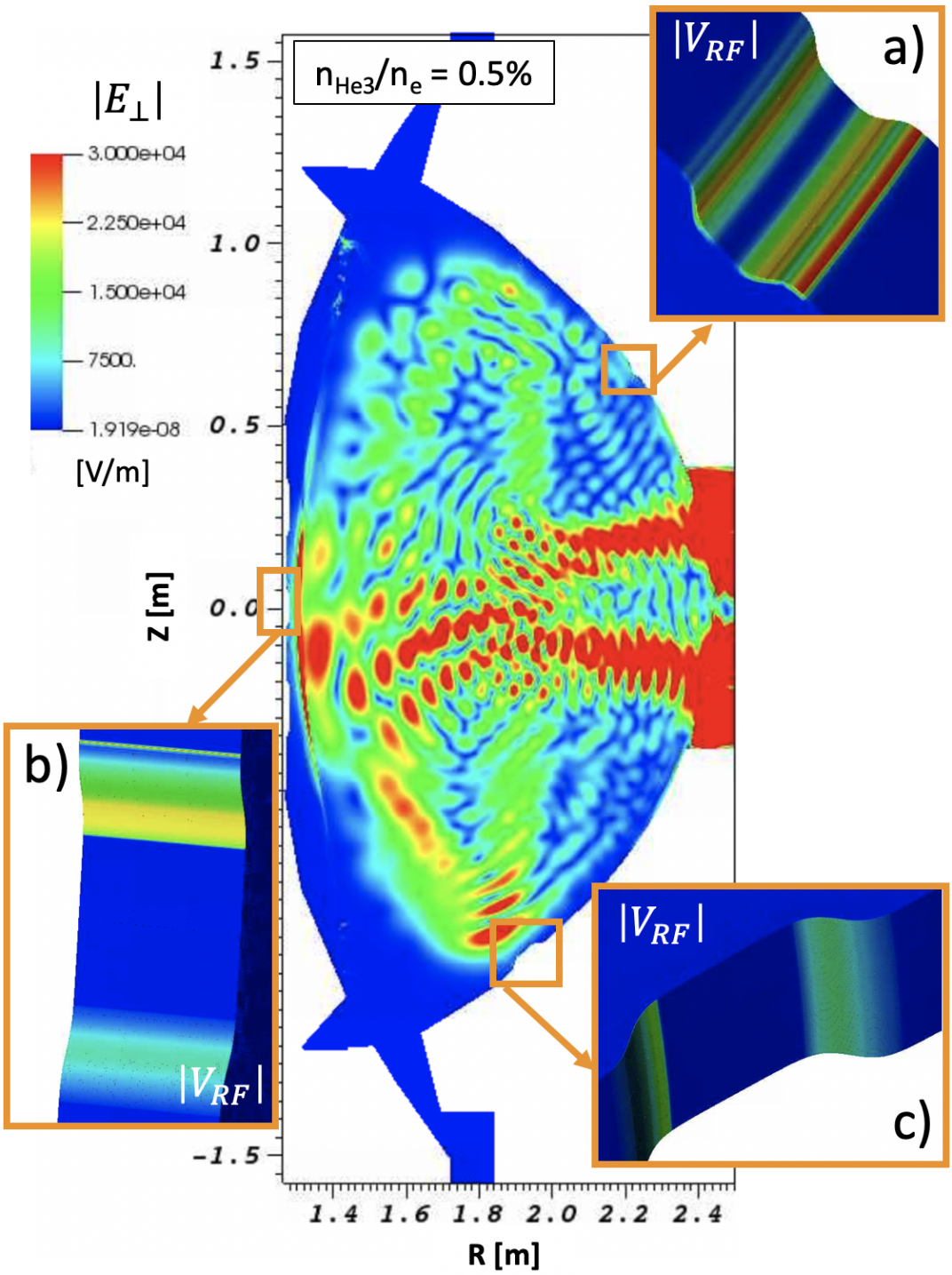

Figure 5.14: 2D plot of the magnitude of the perpendicular electric field, $|E_\perp|$, for the low single pass absorption case of 0.5% helium-3 with various limiter-like bumps placed poloidally along the vacuum vessel (VV). The fields shown in boxes a), b), and c) show the corresponding magnitude of the RF sheath potential along the limiter bumps. It is seen that by including these bumps, the regions where there is a rapidly varying magnetic field angle into the VV produces a peak in rectification. For this case the V_{peak} varied from 47.43 V to 77.97 V, a notable increase in voltage from the same absorption strength but having no limiter bumps.

question of what kinds of far-field sheaths form when b_n is larger or worst case scenario when the magnetic field angle is directly perpendicular to the wall. In the above simulated case, a majority of the peaks in the measured enhanced potentials are noticeably larger than the original VV case. If voltages are now in the 40 - 70 V range for still relatively small b_n, there is a good possibly that for larger b_n the enhanced potentials will be enough to be above the sputtering energy threshold of heavy materials like tungsten in the case of SPARC. These open questions give good motivation to look at the far-field sheath problem in a different reference frame that includes more of the toroidal background field. The top-down view, similar to that described in the previous chapter, extended farther into the toroidal direction with a limiter bump surface farther away from the antenna would be an excellent starting point. This would be a good computational counterpart of the far-field experimental work measured in a similar reference frame done on Alactor C-Mod [38].

Chapter 6

Conclusions and Future Work

6.1 Key Findings

This thesis describes the development of a novel radio frequency (RF) electromagnetic (EM) solver called Stix that supports a non-linear RF sheath boundary condition (BC) used to investigate RF sheath behavior in realistic tokamak geometry. A primary motivator to Stix's creation was to design a code that offers a light-weight but full featured high performance computing capability intended to provide an easier platform for both coupling to other codes as an integrated model and being a test-bed for various numerical methods.

Through Stix's development, it was found that solving for the magnetic field, $\vec{H}$, in the plasma wave equation bypasses the fundamental finite-element issue other EM codes have encountered when trying to implement the full non-linear RF sheath BC. This new approach allows one to solve for $\vec{H}$ simultaneously in the plasma wave equation and the RF sheath BC using a block matrix solve thereby eliminating the need to take the tangential gradient of the discontinuous electric displacement on the boundary that leads to instability. As described in Chapter 3, an extensive suite of 1D/2D analytic and numerical RF sheath cases were used to verify that Stix can successfully solve for the RF sheath potentials. Examples of these problems ranged from 1D multiple root solutions case, important to see whether a fixed point iteration is able to reach higher root solutions, to a 2D curved wall case that demonstrated the success of handling rapid variation of the magnetic field angle into the wall. Demonstrating its test-bed capabilities for various numerical methods, it was found that the scheme of multiple polynomial extrapolation (MPE) for the non-linear solve in Stix shows promising optimization of this problem.

In Chapter 4, the first extension into realistic geometry for the Stix code was replicating the antenna power phasing study done on the Alcator C-Mod tokamak in which the amount of power on the two inner straps (P_{in}) versus the total four straps (P_{tot}) was varied. Using

a 2D slice along the center of the antenna following the pitch of the background magnetic field, it was seen that Stix is able to reproduce the experimental trend of minimization of the enhanced potential using the standard dipole phasing of $(0/\pi/0/\pi)$. Following this phasing scheme done in the experiment, two different phasing schemes of the monopole (0/0/0/0) and the modified dipole $(0/\pi/\pi/0)$ were additionally simulated. Stix confirmed that the monopole configuration resulted in higher enhanced potentials as seen experimentally in C-Mod [71]. Conversely, while the modified dipole scheme did produce higher voltages at the extreme P_{in}/P_{tot} fractions, the minimization was centered around $P_{in}/P_{tot} = 0.5$ and was much broader than its standard dipole phasing counterpart. Having a lower P_{in}/P_{tot} fraction is beneficial for suppressing turbulence in the far SOL [72] but further investigation of this phasing is needed in 3D to see if its a viable operating scheme. Lastly, estimates of the resulting erosion rates and impurity fluxes were made for the worst and best case scenarios for each of the three phasing schemes. It was estimated that D $\rightarrow$ B produced a non-negligible amount of erosion even when the rectified potentials are minimized. Similarly, even with the Mo concentration taken as $n_{Mo}/n_e = 10^{-4}$, the resulting erosion rate of Mo $\rightarrow$ Mo was notable.

This phasing study highlighted the importance 3D geometric effects play in image current cancellation and in turn near-field RF sheath rectification. 2D simulations of an antenna slice are useful to explore the roles of various plasma and antenna parameters on rectification. However, to get a more comprehensive and realistic gauge for how problematic near-fields sheaths are one needs to perform simulations in 3D. Additionally, Stix, TOPICA, and SSWICH-SW simulations of various antenna power phasing scenarios all confirm that including the effects of transport is needed to accurately represent the near-field sheath problem due to the critical role the density plays in rectification and in the ICRF antenna power coupling to the plasma.

The last simulation discussed in this thesis is the predictive study of far-field sheaths in the upcoming high field tokamak SPARC. Using a poloidal slice through 2 of the 12 ICRF antennas, each with 1.67 MW of power, various concentrations of the minority ion species helium-3 were used as a proxy for changing the strength of single pass absorption to see its effect on rectification. First, the comparison to the hot plasma RF solver TORIC showed that adding lower order kinetic corrections (n=0, 1, and 2) to the cold plasma dielectric is able to capture the physical wave-particle resonances for when $\omega = n\Omega_i$ in Stix. Next, it was found that under SPARC conditions, the power with respect to the major radius calculated by integrating the Poynting flux shows that there is a shift from single to multi pass regime as the minority helium-3 concentration is decreased from 2% to 1%. In terms of rectification, it was seen in the 2D (R,Z) poloidal reference frame that the far-field sheath

potentials are minimal even in the lowest single-pass absorption regime. This effect was found to be due to the small normal component of the background magnetic field, b_n, into the plasma facing components with significant portions of the boundary not satisfying the minimum angle criterion for the RF sheath BC. The role of the magnetic field angle into the wall was further tested by incorporating limiter-like bumps along the vacuum vessel where b_n increased from $< 1^\circ$ to $\sim 5^\circ$. It was seen that even with a relatively small change in b_n, it was enough to make the sheath potentials notably higher. This result has implications for extending this investigation to a reference frame that includes more the toroidal component of the background field into the wall as discussed in the next section.

6.2 Future Work

The C-Mod and SPARC simulations have brought forth further insights for the next development steps of the Stix code. The sensible first advancement is to extend the code to be fully three dimensional. Since Stix already solves on a three-dimensional mesh and imposes periodicity in the extruded non-represented third direction, adding the full 3D operators will not be difficult. The importance of the geometry, like the antenna box corners, can be seen when comparing the results of the 2D Stix slice of the C-Mod ICRF antenna to the simulations done on the JET and ITER antennas with TOPICA. The wide poloidal variation of $E_\parallel$ on the RF limiters emphasises that the antenna geometry plays a critical role in RF sheath formations. Therefore, it would be advantageous for further numerical studies of near-field sheaths to include the full 3D geometry.

Although a cold-plasma model allows to solve for RF propagation in complex geometry, one of the difficulties associated with it is resolving the lower hybrid (LH) resonance (S=0) when the SW switches from propagating to evanescent. In the cold plasma limit, when the Stix coefficient S = 0, the SW's $k_\perp \to \infty$ in its dispersion relation. Physically, the wave is mode converting to a kinetic ion Bernstein mode, an effect that is not accounted for in the cold-plasma treatment [87]. To bypass this singular layer, many cold plasma codes simulate near-field sheaths by coupling a vacuum layer to a plasma layer whose density is above the LH resonance [49]. However, Stix and other codes like RAPLICASOL have shown good success in resolving this layer by adding a finite amount of collisionality to the dielectric [2], [88]. Given the SW's critical role in sheath rectification, including a representation of the mode conversion would greatly benefit capturing the true behavior of the wave near the ICRF antenna. Previous work on this problem has found that adding warm ion effects back into the Stix S coefficient by expanding it in terms of $(k_\perp \rho_i)^2$ allows for the inclusion of the mode conversion at the LH resonance [87]. Simulations done in a 1D slab geometry using

this thermal correction have been shown to be successful [89] and provide motivation for Stix to pursue a similar approach.

Another development step involves further extending the kinetic corrections to the cold-plasma dielectric, described in Chapter 2, by adding the toroidal broadening of the plasma dispersion function [90]. This correction adds the effects of toroidicity to ion cyclotron damping that results in a Doppler broadening of the resonance layer thus an increase in heating efficiency [90], [91]. Adding this correction would result in the Stix core plasma solutions being closer to the hot plasma solver TORIC's solutions that take this into account [90]. One can add toroidal broadening with a simple modification of $k_{\|}$ given by Eq. 11 of Brambilla 1994 [90].

In terms of progressing RF simulations, we see integrated modeling as a key component of simulating plasma-wall interactions in the presence of RF. From the investigation of the power phasing antenna C-Mod study, it was found that "while minimizing $E_{\|}$ on the antenna is important for decreasing the enhanced potentials, the mechanism behind the behavior of the associated impurity generation measured in the various experiments is still not fully understood. This effect can be highlighted by comparing the impurity results found on AUG and C-Mod that show the importance of geometry. In C-Mod,"‡ boron "sources were more prominent farther away from the antenna than in AUG because the RF limiter is behind the plasma limiter. In contrast, the AUG RF limiters are the plasma limiters and therefore the tungsten is more local as a source [21]. Not only does the antenna geometry have influence, as mentioned before, transport effects are important in this region and are completely missing with EM RF simulations. The impact of transport can be seen by comparing the minimization region of the"‡ boron "impurities versus the enhanced potentials measured on C-Mod in which the impurities were minimized for a lower power phasing fraction and for a broader region [33], [34]."‡

Another motivation to couple to a transport code is to have a more realistic density profile for the 2D (R,Z) poloidal cross-section. At the moment, the SOL density is taken to be an negative exponential with a characteristic decay length dependent on the distance from the LCFS. This parameterization is currently done using the square root of the normalized poloidal flux and therefore regions like the divertor do not have accurate densities. The divertor regions are the only areas in this poloidal reference frame where the b_n into the wall surface is large. Therefore it is important to include realistic densities to get a sense of whether ICRF waves can reach this region and cause rectification.

From the inception of Stix, it was designed to be part of a multi-physics workflow that includes the effects of transport and impurities aimed to provide a more complete picture of the impacts of RF sheath rectification. The two physics open-sourced codes of interest

are the MAPS [50] and RustBCA [75] codes. MAPS is a fluid transport finite-element code that solves for the coupled particle, parallel momentum, and energy equations. Combining the Stix and MAPS models in as multiphysics workflow is facilitated by their common FEM library, MFEM. RustBCA provides information on the resulting impurity generation by using a binary collision approximation code that calculates the sputtering yield based on the ion's angle and energy. Coupling to RustBCA requires the conversion from the macro-scale fluid to a micro-scale kinetic view using a particle-in cell plasma-edge interaction code called hPIC2 [92]. However, given that the RF sheath physics is localized, this two-step coupling is straightforward. Recently, there have been steps initiating the coupling of Stix and RustBCA as reported in [77] to get quantitative values for the C-Mod power phasing study. The erosion and impurity flux values shown in Chapter 4 only serve as an approximation of how deleterious sheath rectification can be. An impurity generation code like RustBCA would serve to fully capture the physics that is neglected at lower incident energies in the empirical expressions of sputtering yield curves used in Chapter 4's analysis.

The predictive far-field sheath study done for SPARC showed the importance of the magnetic field angle into the wall for sheath formation. At the moment, there is no BC representation of the sheath for angles smaller than the minimum angle of formation ($< 1°$). Codes like Stix, Petra-M, and VSim are forced to neglect portions of the boundary where this constraint is violated. Even though there is no computational model for this limiting case, there still physically exists a sheath for these small angles [20] and therefore there is a need to include representation of it within these kinds of simulations. This grazing angle is not limited to just the 2D poloidal cross-section, in the near-field frame of reference the RF antenna limiter surfaces facing the plasma also tend to be nearly parallel to the background field. Recently there has been work by J. Myra and H. Kohno 2023 to produce an expression that is able to account for these grazing angles [93]. This new approach results in the problem becoming less localized by taking a surface integration of the sheath admittance allowing regions of tangency to be smoothed out by neighboring values and is a current area of research [93].

Lastly, again due to the magnetic field dependence on rectification strength from the predictive SPARC simulations, the extension of looking at far-field sheaths in a different reference frame is of particular interest. As discussed in Chapter 5, there are experimental measurements of non-magnetically connected far-field sheaths done on C-Mod for a limiter farther away in the torus from the antenna done by R. Ochoukov et. al [38] that is an entirely different perspective than the 2D poloidal cross-section. To simulate this kind of experiment, the top-down view similar to the C-Mod power phasing study should be taken in order to include the toroidal component of the magnetic field into the plasma facing component. This

is a critical next step to gauge the strength of far-field rectification in machines like SPARC. A primary motivator for this was the effect seen in the SPARC simulations where increasing the b_n by a few percent caused rectification to increase non-negligibly. The setup for this type of simulation is already included in Stix and just requires a new mesh to include more of a toroidal component of the magnetic field as well as a limiter bump.

Appendix A

How to run Stix

A.1 How to Install

The Github repository for the Stix code can be found at:
https://github.com/mfem/mfem/tree/dh-sheath-bc-dev/miniapps/plasma.
Stix is operational but is under active development and therefore is subject to change in the "dh-sheath-bc-dev" branch. In order to run Stix, one first needs to install MFEM, instructions for which can be found at: https://mfem.org/building/. Additionally, the following libraries need to be installed: MUMPS, SuperLU, MINRES, HYPRE, METIS, SCOTCH and have access to using MPI. The paths to these libraries should be defined within the MFEM config file. With all the supporting libraries setup, one can run the command **make stix2d_dh** to make the Stix code.

A.2 How to Visualize Stix Data

At this time, the best way to visualize data from Stix is to use the software: VisIt [94] https://visit-dav.github.io/visit-website/. Besides the GUI interface of VisIt, one can use a python script through the library *visit* to perform the same functions. A detailed tutorial on the various python-visit functions can be found at http://www.princeton.edu/~efeibush/viscourse/VisItPythonManual.pdf. There are a wide variety of operations and plots one can do on the MFEM data, all of which can be found on VisIt's documentation.

To visualize the 2D color filled plots from Stix using the VisIt GUI, open the written data file of type titled *STIX2D-AMR-Parallel_000001.mfem_root*. Under **plots** select **pseudocolor** and select which variable to visualize then click **draw**. With a pseudocolor field plotted, one can perform various actions. The two most common are finding data at

a particular point or taking a 1D lineout of the data. To extract data from one point, first click **controls** from the top menu bar and select **query**. Under the queries options select **pick**. One can choose which variable to get data from, **default** is set to whatever variable is plotted in the pseudocolor plot. Next select **pick using coordinate to determine node**, this takes data from the closest node to the user specified (x,y,z) point. Type in the (x,y,z) point with no commas into the coordinate bar and select query.

To get a 1D lineout plot of a field, follow the same step of **control** → **query** but select **lineout** under the queries options. Same as the method to extract data using a specific data point, specify which variable to plot or keep as default. Type the start point and end point in terms of (x,y,z) with no commas and select query. Lastly to save the position and data points from the lineout, make sure the active window on the top left of the menu bar is set to the lineout plot, usually it is window 2 if there aren't any other plots open. Next in the top menu select **file** → **set save options**. One can either save the lineout as the plot from Visit as png or select data type to **curve** to get the corresponding data then select **save**.

A.3 Meshes

Stix uses meshes generated in the software "GMSH". The inputted mesh is assumed to be in 2D Cartesian coordinates of x and y with the third z direction is extruded within the Stix code. At the moment, Stix only supports using quadrilateral elements rather than the traditional triangular elements. As such, the proper 2D unstructured meshing algorithm needs to be set for quad elements, examples of which include Blossom and Frontal-Delaunay. Complicated geometric meshes can be constructed efficiently using the python library called *gmsh*.

A.4 Command Line Options

Command line flags:

-m : string

Mesh file to use

-f : double

Wave's frequency in Hertz

-s : integer

Solver to use

Options: 1 - GMRES, 2 - FGMRES, 3 - MINRES, 4 - SuperLU, 5 - STRUMPACK, 6 - Real MUMPS, 7 - Complex MUMPS

-o : integer

Finite element order (polynomial degree), default is set to 1.

-k-vec : list of either 3 doubles or 6 doubles (if complex).

Phase shift vector across periodic directions. For complex phase shifts input 3 real phase shifts followed by 3 imaginary phase shifts. Default is set to 0 in all 3 directions.

-q : list of integers

Charges of the various species (in units of electron charge) that does not include the minority ion species for ICRF (separate flag, see below). Currently only set up to be either D-D or D-T majority plasma. Default is set to single species deuterium plasma.

For specifying density, there are 2 options. Both options require the user to chose a plasma profile specified in the cold_plasma_dielectric_coefs.cpp script. See section A.5 for full description of available profiles.

1. Have the density profile defined everywhere in the domain

   -dp : integer

   Specifies which plasma profile to use

   -dpp : list of doubles

   Arguments needed for the specified plasma profile

or

2. Have the specified density profiles defined for various distinct interior surfaces of the mesh. Currently the codes supports having up to 3 different density profile regions. Each distinct region is labeled: vac, sol, or core with each region needing 3 flags: dp-, dpp-, and dpa- followed by the region label. For example: -dpa-vac, -dp-vac, and -dpp-vac is for 1 region. Note one does not need to use all 3 regions. All 3 region identifiers use the following format:

-dpa-"..." : integer

Attribute number associated with interior surface

-dp-"..." : integer

Specifies which plasma profile to use

-dpp-"..." : list of doubles

Arguments needed for the specified plasma profile

Here "..." represents either vac, sol, or core.

For specifying background magnetic field, there are 2 options.

1. Use a specified profile found in the cold_plasma_dielectric_coefs.cpp script. See section A.5 for full description of available profiles.

   -bp : integer

   Specifies which magnetic field profile to use

   -bpp : list of doubles

   Arguments needed for the specified magnetic field profile

or

2. Use an EQDSK (equilibrium magnetic field profile)

   -bp : 5

   -bpp : 0

   -eqdsk : string

   Name of equilibrium file

There are two ways to specify an antenna current source:

1. Using a volumetric current source, code supports three types of shapes: rod, rectangular, and curved

   i. Rod

   -rod : list of 9 doubles

   In the order of: 3D Vector Amplitude (Real x,y,z, Imag x,y,z), 2D Position, Radius

ii. Rectangular

-slab : list of 10 doubles

In the order of: 3D Vector Amplitude (Real x,y,z, Imag x,y,z), 2D Position, 2D Size

-slab-prof : integer

0 (Constant) or 1 (Cos^2 function) current profile

iii. Curve

-curve : list of either 3 doubles (if 1 antenna, only real amplitude), 5 doubles (if 2 antennas, only real amplitude), 7 doubles (if 1 antenna, complex amplitude), or 9 doubles (if 2 antennas, both complex amplitude),

Curved antenna parameters, in the order of:

Number of antennas, real 2D vector amplitude of antenna 1: Re(θ,1), Re(ϕ,1), real 2D vector amplitude of antenna 2: Re(θ,2), Re(ϕ,2) (skip if only 1 antenna), imaginary 2D vector amplitude of antenna 1: Im(θ,1), Im(ϕ,1), imaginary 2D vector amplitude of antenna 2: Im(θ,2), Im(ϕ,2) (skip if only 1 antenna)

-vol-prof : integer

0 (Constant) or 1 (Cos^2 function) current profile

or

2. Setting a total current on a boundary surface, usually used for rectangular mesh cutoffs

-dbcs-msa : list of integers

List of boundary attributes to set the total current on

-ns : integer

Number of antenna sources

-sp : list of doubles

Strap parameters consisting of 4 (x, y) positions for each antenna current source

-sc : list of doubles

Values to use for total current consisting of real and imaginary values for each antenna current source

Optional boundary condition flags:
Note that any boundary surfaces that aren't specified to be a specific type of BC in the command line, are conducting wall BCs in Stix's finite-element formulation.

1. Neumann BC, code supports up to 2 different values, needs 2 flags for each BC, label is either 1 or 2

   -nbcs"..." : list of integers

   List of boundary attributes to use Neumann BC on

   -nbcv"..." : list of doubles

   Value to use in the format of: (v_x, v_y, v_z) or (Re(v_x) Re(v_y) Re(v_z) Im(v_x) Im(v_y) Im(v_z))

   Here "..." represents either 1 or 2

2. Dirichlet BC, code supports up to 2 different values, needs 2 flags for each BC, label is either 1 or 2

   -dbcs"..." : list of integers

   List of boundary attributes to use Dirichlet BC on

   -dbcv"..." : list of doubles

   Value to use in the format of: (v_x, v_y, v_z) or (Re(v_x) Re(v_y) Re(v_z) Im(v_x) Im(v_y) Im(v_z))

   Here "..." represents either 1 or 2

3. Sheath BC

   -sbcs : integer

   List of boundary attributes to use sheath BC on

Other optional flags:

-min : list of doubles

Used if there is a minority ion species in the order of: charge, mass (amu), concentration (n_{min}/n_e)

-logo : Boolean

Print logo and exit, default set to false

-mo : integer

Geometry order for cylindrically symmetric mesh, default set to 1

-mh : double

Thickness of extruded mesh in meters, for Cartesian coordinates only.

-cyl : Boolean

Defines whether code uses Cartesian (x, y, z) coordinates - false or Cylindrical (z, rho, phi) - true, default is false.

-mhc : double

Thickness of cylindrically extruded mesh in degrees, used with -cyl flag, default is set to 3 degrees

-per-y : Boolean

Specifies that the input mesh is periodic in the y-direction, default is false

-rs : integer

Number of times to refine the mesh uniformly in serial, default is set to 0

-pa or **-no-pa** : Boolean

Enable partial assembly (GPU), default is set to false.

-vis or **-no-vis** : Boolean

Enable or disable GLVis visualization, default is set to false.

-visit or **-no-visit** : Boolean

Enable or disable VisIt visualization, default is set to false.

-w : string

Used for when there exists an analytic solution to get the L2 norm of the computed solution. Default is set to zero. Options are:

'R' - Right Circularly Polarized, 'L' - Left Circularly Polarized, 'O' - Ordinary, 'X' - Extraordinary, 'J' - Current Slab (in conjunction with -slab), 'Z' - Zero

Similar to setting the density, a temperature profile (used for kinetic corrections to the Stix coefficients) can be set either by interior surface region or globally. The only difference between the density and temperature flags is that temperature only supports up to 2 regions: sol or core.

1. To have the temperature profile defined everywhere in the domain

   -tp : integer

   Specifies which plasma profile to use

   -tpp : list of doubles

   Arguments needed for the specified plasma profile

or

2. Have the specified density profiles defined for 2 distinct interior surfaces of the mesh.

   -tpa-"..." : integer

   Attribute number associated with interior surface

   -tp-"..." : integer

   Specifies which plasma profile to use

   -tpp-"..." : list of doubles

   Arguments needed for the specified plasma profile

   Here "..." represents either sol or core.

One can also specify an artificial collisional profile set on the electron terms of the Stix coefficients using either a parameterized profile using the 2 flags below or using the electron-ion thermal collisional frequency, ν_{ei}. Default is set to 0.

One must specify **-nuprof** to be = 1 (parameterized profile) or = 0 (ν_{ei})

1. Using a parameterized profile:

   -nuprof : 1

   -nep : integer

   Specifies which plasma profile to use

   -nepp : list of doubles

   Arguments needed for the specified plasma profile

2. Using $\nu_{ei} \propto \frac{n_e}{T_e^{3/2}}$:

   -nuprof : 0

There must be a non-zero temperature profile specified.

Similarity, the ion artificial collisional frequency can be specified using the 2 flags below. Default is set to 0.

-nip : integer

Specifies which plasma profile to use

-nipp : list of doubles

Arguments needed for the specified plasma profile

There are two options for AMR, there is global AMR and AMR focused on the either the cut-offs or resonances of the Stix coefficients, i.e. P = 0 or S = 0 (user specified).

1. Global AMR:

   -maxit : integer

   Max number of iterations in the main AMR loop

2. AMR on either S = 0 or P = 0 Stix coefficients:

   -amr-stix or **-no-amr-stix** : Boolean

   Initial AMR to capture either Stix S or P coefficient when it crosses 0, default is set to true.

   -amr-coef : integer, either 0 or 1

   Choose which Stix coefficient to refine: 0 - S, 1 - P. Default set to S.

   -iatol : double

   Initial AMR tolerance, default is set to 10^{-5}.

   -iamit : double

   Initial AMR maximum number of iterations, default is set to 10.

   -iamdof : double

   Initial AMR maximum number of DoFs, default is set to 10^5.

A.5 Parameterized Plasma and Magnetic Field Profiles

A.5.1 Plasma Profiles

These parameterizations can be used for defining density, bulk electron temperature, and artificial collisional profiles. They are coefficient objects are and created following

```
PlasmaProfile CoefficientNameHere(Type type,
                                  const Vector & params,
                                  CoordSystem sys,
                                  G_EQDSK_Data *eqdsk)
```

Here **type** refers to the which plasma parameterization to use indicated by the integer in front on the names in the list below, **params** is a list of doubles that represents the corresponding arguments needed to set up the parameterization (case specific), **sys** is either set to PlasmaProfile::POLOIDAL or PlasmaProfile::CARTESIAN_3D to indicate whether the extrusion is a wedge or straight, and lastly **eqdsk** is the equilibrium background magnetic field (EQDSK) which can be NULL if the magnetic field is parameterized through a profile that is described in the next subsection. There are currently 15 options available as shown in the **PlasmaProfile** class in *cold_plasma_dielectric_coefs.cpp* file. Ut should be noted that all the arguments are in SI units. The options are:

0 - CONSTANT: 1 argument

- The constant value of parameter

1 - GRADIENT: 7 arguments

- The value of the parameter at one point
- The location of this point (3 values: x, y, z)
- The gradient of the parameter at this point (3 values: x, y, z)

2 - TANH: 9 arguments

- The value of the parameter when tanh equals zero
- The value of the parameter when tanh equals one
- The skin depth, defined as the distance, in the direction of the steepest gradient, between locations where tanh equals zero and where tanh equals one-half
- The location of a point where tanh equals zero (3 values: x, y, z)
- The unit vector in the direction of the steepest gradient away from the location described by the previous parameter (3 values: $\hat{x}, \hat{y}, \hat{z}$)

3 - ELLIPTIC_COS: 7 arguments

- The value of the parameter when cos equals minus one
- The value of the parameter when cos equals one

- The radius of the ellipse in the x direction
- The radius of the ellipse in the y direction
- The center of the ellipse

4 - PARABOLIC: 4 arguments

Follows profile of: $p_{max} e^{\left(\frac{-\rho}{p_{min}}\right)^2}$

- The maximum value: p_{max}
- The value of: p_{min}
- The central location: $\vec{x}_0 = (x_0, y_0, z_0)$

5 - PEDESTAL: 7 arguments

Follows profile of: $(p_{max} - p_{min}) \cosh\left[\left(\frac{\rho}{\lambda_n}\right)^{\nu}\right]^{-1} + p_{min}$

- The value of at the bottom of the pedestal: p_{min}
- The value of at the top of the pedestal: p_{max}
- The damping length: λ_n
- The strength of the decline: ν
- The location of the pedestal: $\vec{x}_0 = (x_0, y_0, z_0)$

6 - NUABSORB: 3 arguments

Follows a profile of: $\nu = \nu_0 e^{-(x-shift)/decay}$

- The coefficient: ν_0
- The decay rate: $decay$
- The shift: $shift$

7 - NUE: 3 arguments

Follows a profile of: $\nu = \nu_0 e^{-(x-shift)/decay}$ + additional tailored correction for cut-off (C-Mod related)

- The coefficient: ν_0
- The decay rate: $decay$
- The shift: $shift$

8 - NUI: 3 arguments

Follows a profile of: $\nu = \nu_0 e^{-(x-rad\_res\_loc)^2/width}$

- The location of the resonance: rad_res_loc
- The coefficient: ν_0
- The width of Gaussian profile: $width$

The next profiles are device specific to the simulations done in Chapter 4 and 5.

9 - CMODDEN: 1 argument

- This case is specific to the top-down view of C-Mod and therefore the argument isn't used, parameterized is done without any user definition. Gives back density plot shown in Fig. 4.2.

10 - POLOIDAL_H_MODE_DEN: 1 argument

- This case is specific to the (R,Z) poloidal cross-section and therefore the argument isn't used, parameterized is done without any user definition. Corresponds to an H-mode electron density profile.

11 - POLOIDAL_H_MODE_TEMP: 1 argument

- This case is specific to the (R,Z) poloidal cross-section and therefore the argument isn't used, parameterized is done without any user definition. Corresponds to an H-mode electron temperature profile.

12 - POLOIDAL_CORE: 1 argument

Parameterizes the core of a poloidal cross-section

- This case is specific to the (R,Z) poloidal cross-section and therefore the argument isn't used, parameterized is done without any user definition. Corresponds to an H-mode electron density core profile.

13 - POLOIDAL_SOL: 5 arguments

Parameterizes the scrape-off layer of a poloidal cross-section

- The floor value to use
- The density at the LCFS
- The decay length between the LCFS and outer limiter in meters
- The decay length between the outer limiter and Faraday screens

- The decay length between the Faraday screen and antenna straps

14 - POLOIDAL_MIN_TEMP: 2 arguments

Parameterizes the minority ion heating tail in the core of the poloidal cross-section

- The concentration of the minority species
- The mass of the minority species

A.5.2 Background Magnetic Field Profiles

There are 6 options to choose for the magnetic field parameterization profiles in Stix. They are set up very similar to the plasma profile parameters. The options are:

0 - CONSTANT: 3 arguments

- The constant values of magnetic field: (B_x, B_y, B_z)

1 - B_P1: 7 arguments

- Absolute value of the poloidal magnetic field
- The radius of the ellipse in the x direction
- The radius of the ellipse in the y direction
- The magnetic axis: $\vec{x}_0 = (x_0, y_0, z_0)$
- The toroidal magnetic field

2 - B_P2: 4 arguments

- The poloidal magnetic field value
- The magnetic axis: $\vec{x}_0 = (x_0, y_0, z_0)$

3 - B_P_KOHNO: 8 arguments

- The minor radius: r_{min}
- The major radius: r_{maj}
- The safety factor on magnetic axis: q_0
- The edge safety factor: q_a
- The magnetic field axis: $\vec{x}_0 = (x_0, y_0, z_0)$
- The toroidal magnetic field: b_{z0}

4 - B_EQDSK_TOPDOWN: 4 arguments

Option to use for EQDSK file in the top-down reference frame

- The center "x" position: u_0
- The center "y" position: v_0
- The center "z" position: z_0
- The angle of rotation of the plane: θ

5 - B_EQDSK_POLOIDAL: 1 arguments

Option to use for EQDSK file in the poloidal reference frame

This case is specific to the (R,Z) poloidal cross-section and therefore the argument isn't used, parameterized is done without any user definition.

A.6 Example Case

An example of a simple 1D case of x = 0 m to x = 0.24 m with a volumetric current source placed in the middle of the domain (x = 0.12 m). Mesh can be found on the GitHub branch consisting of 2400 elements in $\hat{x}$ and 4 elements in $\hat{y}$.

```
mpirun -np 32 ./stix2d_dh -m periodic-slab-t4.msh -f 80e6 -s 7 -dp 0
-dpp 2e20 -maxit 1 -tp 0 -tpp 10 -per-y -k-vec '0 0 0' -slab '0 1e4 0
0.12 0.005 0.01 0.01' -slab-prof 0 -no-vis -nuprof 1 -bp 0 -bpp '0 0 5.4'
-nep 0 -nepp 0 -mh 0.01
```

Will give back a solution like this:

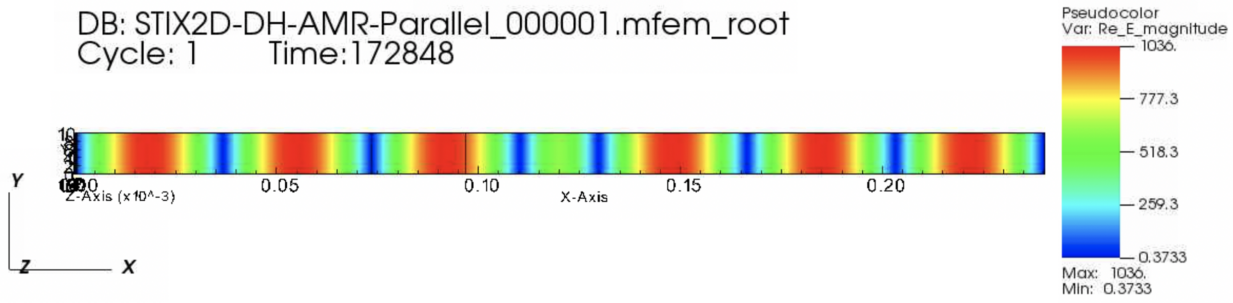

Figure A.1: The magnitude of the real electric field from the above example command line.

Appendix B

Adding Kinetic Effects to the Cold Plasma Dielectric

In this appendix the derivation of the lower order kinetic effects of the hot plasma dielectric are shown for the S, D, and P cold plasma Stix coefficients. Replacing the cold plasma Stix coefficients with these new expressions resolves the wave-particle singularity in cold plasma dielectric, i.e. for when $\omega = \Omega_i$, critical for poloidal cross-sectional modeling. For this derivation, only the 0th, 1st, and 2nd order corrections are considered due to the composition of the plasma described in Chapter 5.

First starting with the hot plasma dielectric given by [41]

$$\bar{\bar{\varepsilon}} = 1 + \sum_j \bar{\bar{\chi}}_j, \quad \bar{\bar{\chi}}_j = \left(\frac{\omega_{p,j}^2}{\omega} \sum_{n=-\infty}^{\infty} e^{-\lambda} \bar{\bar{\mathbf{Y}}}_n \right)_j \tag{B.1}$$

where

$$\bar{\bar{\mathbf{Y}}}_n = \begin{pmatrix} \frac{n^2 I_n}{\lambda} A_n & -in\left(I_n - I_n'\right) A_n & \frac{k_\perp}{\Omega} \frac{n I_n}{\lambda} B_n \\ in\left(I_n - I_n'\right) A_n & \left(\frac{n^2}{\lambda} I_n + 2\lambda I_n - 2\lambda I_n' \right) A_n & \frac{ik_\perp}{\Omega}\left(I_n - I_n'\right) B_n \\ \frac{k_\perp}{\Omega} \frac{n I_n}{\lambda} B_n & -\frac{ik_\perp}{\Omega}\left(I_n - I_n'\right) B_n & \frac{2(\omega - n\Omega)}{k_\parallel v_{th,\perp}^2} I_n B_n \end{pmatrix} \tag{B.2}$$

and

$$A_n = \frac{Z\left(\zeta_n\right)}{k_\parallel v_{th}}, \quad B_n = -\frac{Z'\left(\zeta_n\right)}{2k_\parallel}, \quad \lambda = \frac{k_\perp^2 v_{th}^2}{2\Omega^2}, \quad \zeta_n = \frac{\omega - n\Omega}{k_\parallel v_{th}} \tag{B.3}$$

Here $I_n = I_n(\lambda)$ is the modified Bessel function, $I_n' = \frac{1}{2}(I_{n-1} + I_{n+1})$, v_{th} is the thermal speed

of the particle j taken to be $\sqrt{2T_e/m_j}$, and

$$Z(\zeta_n) = \frac{1}{\sqrt{\pi}} \int_{-\infty}^{\infty} dz \frac{e^{-z^2}}{z - \zeta_n}, \quad \mathrm{Im}\,\zeta > 0 \tag{B.4}$$

This $Z(\zeta_n)$ function is known as the plasma dispersion function and can be analytically continued for $\mathrm{Im}\,\zeta \leq 0$ giving

$$Z(\zeta_n) = \frac{1}{\sqrt{\pi}} \int_C dz \frac{e^{-z^2}}{z - \zeta_n} = i\sqrt{\pi} e^{-\zeta_n^2} - \sqrt{\pi} e^{-\zeta_n^2} \mathrm{erfi}(\zeta_n) \tag{B.5}$$

It should be noted that the n $= \pm 1, 2, 3 \cdots$ subscripts represent the harmonics of cyclotron frequency of the plasma species and the n $= 0$ represents the special case of Landau damping. Lastly, the expressions that contain $k_\perp$ are calculated using the cold plasma dispersion relation for a FW, Eq. 2.26.

B.0.1 The S Coefficient: ε_{xx}

Taking the cold plasma limit ($T \to 0$) of the ε_{xx} term in Eq. B.1 leads to the S Stix coefficient repeated here from Chapter 2 as

$$S = 1 - \frac{\omega_{p,e}^2}{\omega^2 - \Omega_e^2} - \frac{\omega_{p,i}^2}{\omega^2 - \Omega_i^2} \tag{B.6}$$

In the ICRF regime, the terms that have singularities are the ones corresponding to the ion response. For simplicity, the ion susceptibility, $\chi_{xx,i}$, will be used in the derivation. Using Eq. B.1 to B.3 gives

$$\chi_{xx,i} = \frac{\omega_{p,i}^2}{\omega} \sum_{n=-\infty}^{\infty} e^{-\lambda} \frac{n^2 I_n(\lambda)}{\lambda} \frac{Z(\zeta_n)}{k_\parallel v_{th,i}} \tag{B.7}$$

Splitting up the infinite sum in the above equation using the identity of $I_n = I_{-n}$ gives

$$\chi_{xx,i} = \frac{\omega_{p,i}^2}{\omega} \sum_{n=1}^{\infty} e^{-\lambda} \frac{n^2 I_n(\lambda)}{\lambda} \frac{1}{k_\parallel v_{th,i}} \left[Z(\zeta_n) + Z(\zeta_{-n}) \right] \tag{B.8}$$

The two harmonics of interest for most ICRF simulations are the first harmonic, n $= 1$, if there is a minority ion species and the second harmonic of the bulk ion population(s), n $= 2$. First looking at adding the kinetic effects for n $= 1$, $\chi_{xx,i,n=1}$ gives

$$\chi_{xx,i,n=1} = \frac{\omega_{p,i}^2}{\omega} e^{-\lambda} \frac{I_1(\lambda)}{\lambda} \frac{1}{k_\parallel v_{th,i}} \left[Z(\zeta_1) + Z(\zeta_{-1}) \right] \tag{B.9}$$

In the ICRF limit, λ is small, therefore making $\lambda << 1$ allows $I_n(\lambda)$ to be written as

$$I_n(\lambda) = \left(\frac{\lambda}{2}\right)^n \sum_{p=0}^{\infty} \frac{1}{(n+p)!p!} \left(\frac{\lambda}{2}\right)^{2p} \tag{B.10}$$

Therefore for n = 1, Eq. B.10 becomes $I_1(\lambda)/\lambda \sim \frac{1}{2}(1 + \lambda^2/8 + \cdots)$. Keeping the lowest order term and plugging back into Eq. B.9 gives

$$\chi_{xx,i,n=1} = \frac{\omega_{p,i}^2}{\omega} \frac{e^{-\lambda}}{2k_{\parallel} v_{th,i}} \left[Z\left(\zeta_1\right) + Z\left(\zeta_{-1}\right)\right] \tag{B.11}$$

The lowest order real-valued component of Eq. B.11 gives back the ion term of the Stix S-component in the cold plasma formulation which can be found using the asymptotic form of the Z function given as,

$$Z(\zeta_n) \approx i\sqrt{\pi} e^{-\zeta_n^2} - \frac{1}{\zeta_n} - \frac{1}{2\zeta_n^3} + \mathcal{O}\left(\zeta_n\right) \text{ for } \zeta_n >> 1 \tag{B.12}$$

Following the same steps above for the second harmonic, n = 2, the ion susceptibility is given as

$$\chi_{xx,i,n=2} = \frac{\omega_{p,i}^2}{\omega} \frac{\lambda e^{-\lambda}}{2k_{\parallel} v_{th,i}} \left[Z\left(\zeta_2\right) + Z\left(\zeta_{-2}\right)\right] \tag{B.13}$$

Using Eq. B.11 and Eq. B.13, and plugging back into Eq. B.1 and keeping the electron contribution in the cold plasma limit gives the thermally corrected S Stix coefficient as

$$\begin{aligned} \varepsilon_{xx} = 1 - \frac{\omega_{p,e}^2}{\omega^2 - \Omega_e^2} &+ \frac{\omega_{p,i}^2}{\omega} \frac{e^{-\lambda}}{2k_{\parallel} v_{th,i}} \left[Z\left(\zeta_1\right) + Z\left(\zeta_{-1}\right)\right] \\ &+ \frac{\omega_{p,i}^2}{\omega} \frac{\lambda e^{-\lambda}}{2k_{\parallel} v_{th,i}} \left[Z\left(\zeta_2\right) + Z\left(\zeta_{-2}\right)\right] \end{aligned} \tag{B.14}$$

B.0.2 The D Coefficient: $\varepsilon_{xy} = \varepsilon_{yx}$

Similar to the S Stix coefficient, the D Stix coefficient has a singularity in the ICRF limit on the ions, repeated here from Chapter 2

$$D = \frac{\Omega_e}{\omega} \frac{\omega_{p,e}^2}{\omega^2 - \Omega_e^2} + \frac{\Omega_i}{\omega} \frac{\omega_{p,i}^2}{\omega^2 - \Omega_i^2} \tag{B.15}$$

Using the same steps as adding the kinetic effects into the S coefficient, the thermal correction to the D coefficient is derived by using the xy component of the ion susceptibility, $\chi_{xy,i}$, given as

$$\chi_{xy,i} = -i\frac{\omega_{p,i}^2}{\omega}\sum_{n=-\infty}^{\infty} ne^{-\lambda}\left(I_n - I_n'\right)\frac{Z\left(\zeta_n\right)}{k_\parallel v_{th,i}} \tag{B.16}$$

Again, splitting up the infinite sum using the identity of $I_n = I_{-n}$ in Eq. B.16 as

$$\chi_{xy,i} = -i\frac{\omega_{p,i}^2}{\omega}\sum_{n=1}^{\infty} e^{-\lambda}\frac{n\left(I_n - I_n'\right)}{k_\parallel v_{th,i}}\left[Z\left(\zeta_n\right) - Z\left(\zeta_{-n}\right)\right] \tag{B.17}$$

Now taking n = 1, gives

$$\chi_{xy,i,n=1} = -i\frac{\omega_{p,i}^2}{\omega}e^{-\lambda}\frac{\left(I_1 - \frac{1}{2}I_0 - \frac{1}{2}I_2\right)}{k_\parallel v_{th,i}}\left[Z\left(\zeta_1\right) - Z\left(\zeta_{-1}\right)\right] \tag{B.18}$$

Again assuming $\lambda << 1$ and keeping the lowest order term of λ simplifies the above expression to

$$\chi_{xy,i,n=1} = -\frac{1}{2}\frac{\omega_{p,i}^2}{\omega}\frac{e^{-\lambda}}{k_\parallel v_{th,i}}\left[Z\left(\zeta_1\right) - Z\left(\zeta_{-1}\right)\right] \tag{B.19}$$

Similarly for n = 2 harmonic,

$$\chi_{xy,i,n=2} = -\frac{1}{2}\frac{\omega_{p,i}^2}{\omega}\frac{\lambda e^{-\lambda}}{k_\parallel v_{th,i}}\left[Z\left(\zeta_2\right) - Z\left(\zeta_{-2}\right)\right] \tag{B.20}$$

Plugging Eq. B.19 and Eq. B.20 into Eq. B.1 and keeping the electron term in the cold plasma limit gives the thermally corrected D Stix coefficient as

$$\begin{aligned}\varepsilon_{xy} = \varepsilon_{yx} = \frac{\Omega_e}{\omega}\frac{\omega_{p,e}^2}{\left(\omega^2 - \Omega_e^2\right)} &- \frac{\omega_{p,i}^2}{\omega}\frac{e^{-\lambda}}{2k_{||}v_{th,i}}\left[Z\left(\zeta_1\right) - Z\left(\zeta_{-1}\right)\right] \\ &- \frac{\omega_{p,i}^2}{\omega}\frac{\lambda e^{-\lambda}}{2k_\parallel v_{th,i}}\left[Z\left(\zeta_2\right) - Z\left(\zeta_{-2}\right)\right]\end{aligned} \tag{B.21}$$

B.0.3 The P Coefficient: ε_{zz}

While there may not be a singularity in cold plasma P coefficient, repeated here from Chapter 2

$$P = 1 - \frac{\omega_{p,e}^2}{\omega^2} - \frac{\omega_{p,i}^2}{\omega^2} \tag{B.22}$$

one can add a 0th order thermal correction to include electron Landau damping. Here the derivation will focus only on the electron term of ε_{zz} given as

$$\chi_{zz,e} = \frac{\omega_{p,e}^2}{\omega} \sum_{n=-\infty}^{\infty} -e^{-\lambda} \frac{2\left(\omega - n\Omega_e\right)}{k_{||} v_{th,e}^2} \frac{Z'\left(\zeta_n\right)}{2k_{||}} I_n \tag{B.23}$$

Taking n = 0 gives

$$\chi_{zz,e,n=0} = -\frac{\omega_{p,e}^2}{\omega} e^{-\lambda} \frac{\omega}{k_{||}^2 v_{th,e}^2} Z'\left(\zeta_0\right) I_0 \tag{B.24}$$

$I_0 e^{-\lambda} \sim 1$ therefore,

$$\chi_{zz,e,n=0} = -\frac{\omega_{p,e}^2}{\omega} \frac{\omega}{k_{||}^2 v_{th,e}^2} Z'\left(\zeta_0\right) \tag{B.25}$$

Plugging Eq. B.25 into Eq. B.1 and keeping the cold plasma ion terms gives the electron Landau thermal correction to the Stix P coefficient,

$$\varepsilon_{zz} = 1 - \frac{\omega_{p,e}^2}{k_{||}^2 v_{th,e}^2} Z'\left(\zeta_0\right) - \frac{\omega_{p,i}^2}{\omega^2} \tag{B.26}$$

Using the identity of $Z'\left(\zeta_n\right) = -2\left(1 + \zeta_n Z\left(\zeta_n\right)\right)$ [41] gives the final expression as

$$\varepsilon_{zz} = 1 + \frac{2\omega_{p,e}^2}{k_{||}^2 v_{th,e}^2} \left(1 + \zeta_0 Z\left(\zeta_0\right)\right) - \frac{\omega_{p,i}^2}{\omega^2} \tag{B.27}$$

Appendix C

Calculations of Sputtering Yields

The method for calculating sputtering yields used for the impurity flux and the erosion rates in Chapter 4 described in this appendix are taken from Yamamura et. al 1996 [14]. Yamamura et. al 1996 introduces a new empirical formulation based on previous experimental data bases of sputtering and simulations in the Monte Carlo ACAT code [14]. This empirical sputtering yield, shown in Eq. C.1, is dependent on the mass of the incident ion (M_1), the mass of the target (M_2), the charge of the incident ion (Z_1), the charge of the target (Z_2), sublimation energy of the target (U_s), fitted parameters (Q, W, and s), and lastly the energy of the incident ion (E) [14]. It should be noted that this expression is for 90° degree of incidence and is valid for all the possible ion–target combinations for any incident ion energy [14].

$$Y(E) = 0.042 \frac{Q\,(Z_2)\,\alpha^*\,(M_2/M_1)}{U_\mathrm{s}} \frac{S_\mathrm{n}(E)}{1 + \Gamma k_\mathrm{e} \epsilon^{0.3}} \times \left[1 - \sqrt{\frac{E_\mathrm{th}}{E}}\right]^s \tag{C.1}$$

where

$$S_\mathrm{n}(E) = \frac{84.78 Z_1 Z_2}{\left(Z_1^{2/3} + Z_2^{2/3}\right)^{1/2}} \frac{M_1}{M_1 + M_2} s_\mathrm{n}^\mathrm{TF}(\epsilon) \tag{C.2}$$

is the nuclear stopping cross section and

$$s_\mathrm{n}^\mathrm{TF}(\epsilon) = \frac{3.441\sqrt{\epsilon}\ln(\epsilon + 2.718)}{1 + 6.355\sqrt{\epsilon} + \epsilon(6.882\sqrt{\epsilon} - 1.708)} \tag{C.3}$$

is the reduced nuclear stopping power based on the Thomas–Fermi potential [14], [95]. Both $S_\mathrm{n}(E)$ and $s_\mathrm{n}^\mathrm{TF}(\epsilon)$ are functions of ϵ the reduced energy with units of eV defined as

$$\epsilon = \frac{0.03255}{Z_1 Z_2 \left\{Z_1^{2/3} + Z_2^{2/3}\right\}^{1/2}} \frac{M_2}{M_1 + M_2} E \tag{C.4}$$

Additionally, k_e represents the Lindhard electronic stopping coefficient defined as

$$k_e = 0.079 \frac{(M_1 + M_2)^{3/2}}{M_1^{3/2} M_2^{1/2}} \frac{Z_1^{2/3} Z_2^{1/2}}{\left(Z_1^{2/3} + Z_2^{2/3}\right)^{3/4}} \tag{C.5}$$

The other parameters in Eq. C.1 include Γ, α^* and the energy threshold E_{th} defined as

$$\Gamma = \frac{W(Z_2)}{1 + (M_1/7)^3} \tag{C.6}$$

$$\alpha^* = \begin{cases} 0.249\,(M_2/M_1)^{0.56} + 0.0035\,(M_2/M_1)^{1.5} & \text{for } M_1 \geq M_2 \\ 0.0875\,(M_2/M_1)^{-0.15} + 0.165\,(M_2/M_1) & \text{for } M_1 \leq M_2 \end{cases} \tag{C.7}$$

$$\frac{E_{\text{th}}}{U_{\text{s}}} = \begin{cases} \frac{6.7}{\gamma} & \text{for } M_1 \geq M_2 \\ \frac{1+5.7(M_1/M_2)}{\gamma} & \text{for } M_1 \leq M_2 \end{cases} \tag{C.8}$$

where

$$\gamma = \frac{4 M_1 M_2}{(M_1 + M_2)^2} \tag{C.9}$$

The last values to know are the fitting parameters W, Q, s and surface binding energy, U_s, taken to be the heat of sublimation of the target material given by Table C.1 taken from [14].

Element	U_s [eV]	Q	W	s
Boron	5.77	2.62	4.39	2.5
Molybdenum	6.82	0.85	2.39	2.8

Table C.1: The dimensionless fitted parameters (Q, W, s) and the sublimation energy, U_s, for the two target materials found in C-Mod taken from [14].

The following sputtering yield curves are found using Eq. C.1 for the most common impurities found in C-Mod impinging on either a boron or molybdenum target.

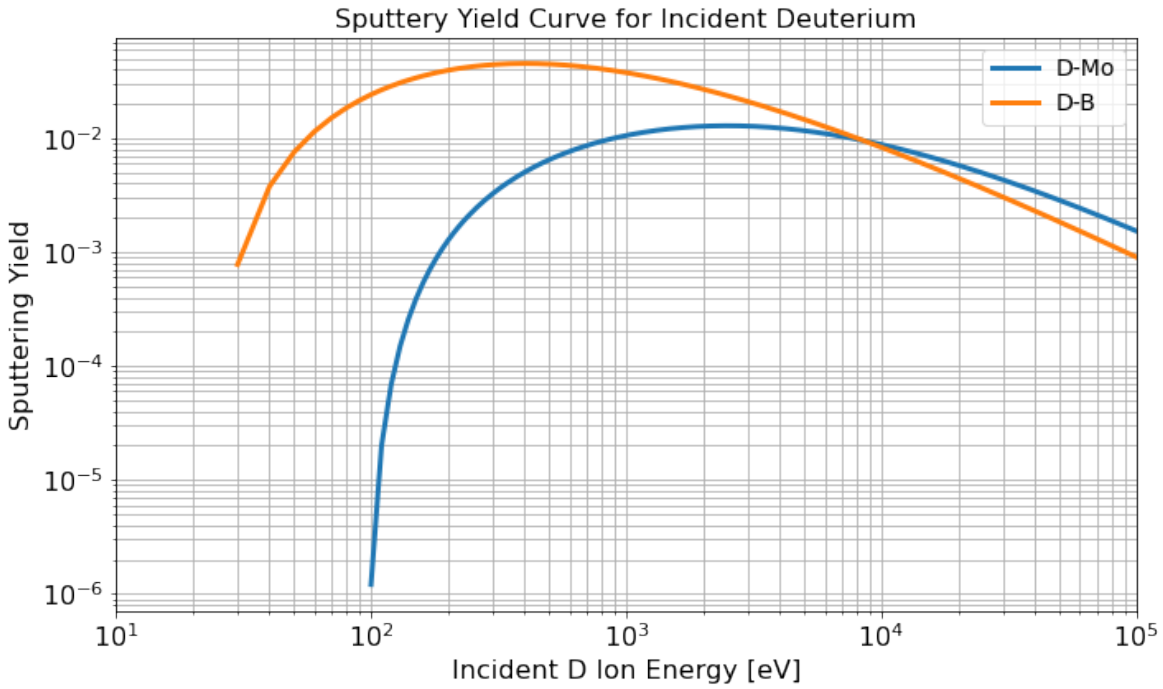

Figure C.1: The resulting sputter yield curve for an incident deuterium ion impinging on a boron (orange) and a molybdenum (blue) target calculated using Eq. C.1.

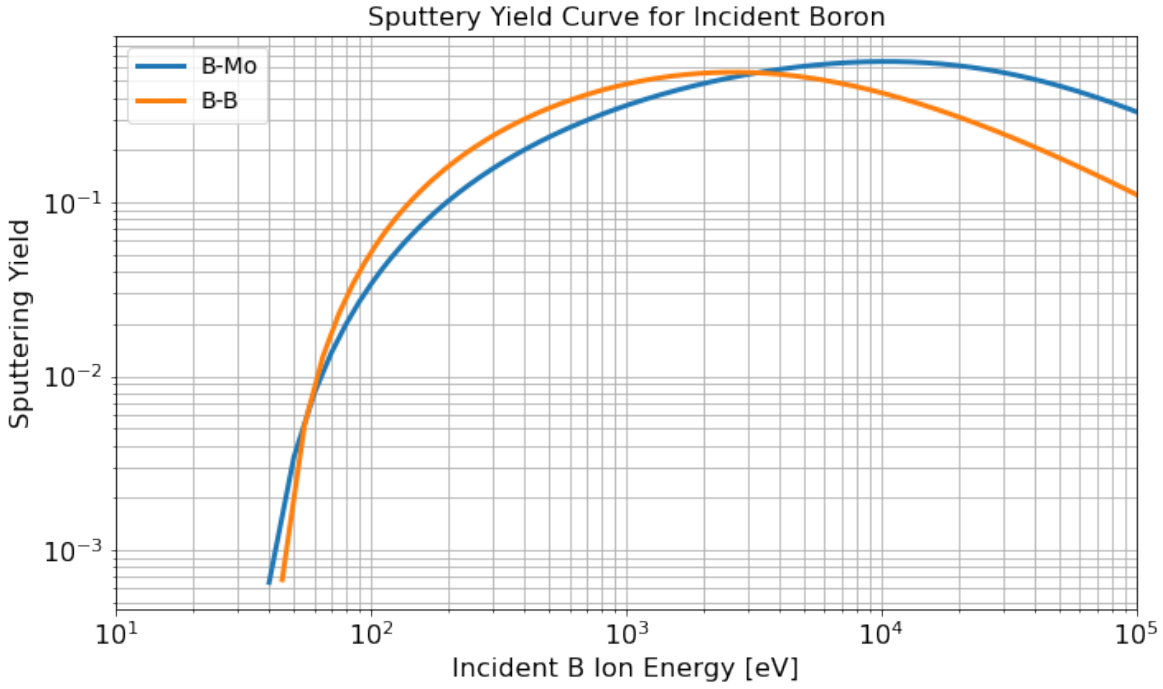

Figure C.2: The resulting sputter yield curve for an incident boron ion impinging on a boron (orange) and a molybdenum (blue) target calculated using Eq. C.1.

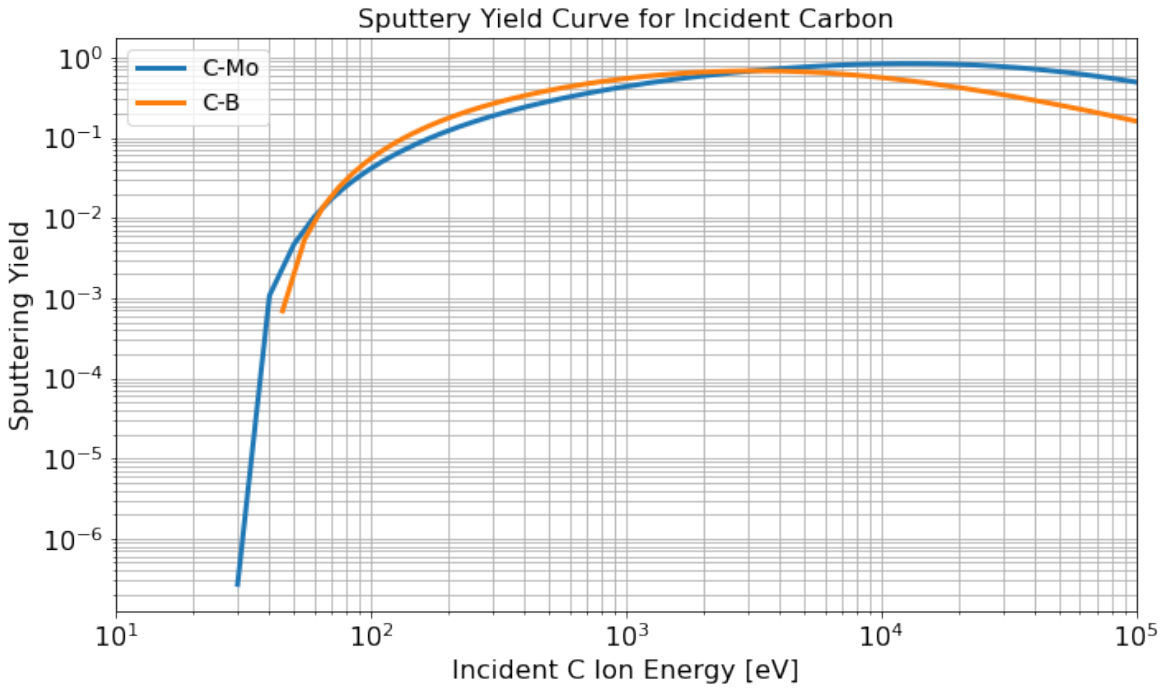

Figure C.3: The resulting sputter yield curve for an incident carbon ion impinging on a boron (orange) and a molybdenum (blue) target calculated using Eq. C.1.

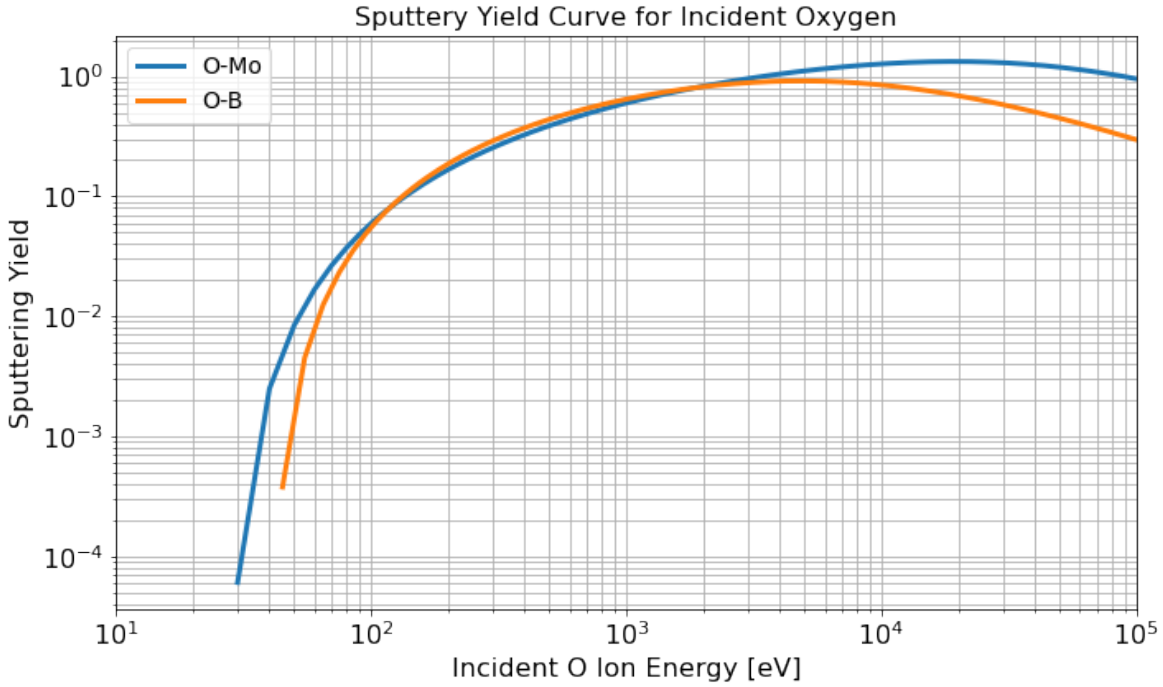

Figure C.4: The resulting sputter yield curve for an incident oxygen ion impinging on a boron (orange) and a molybdenum (blue) target calculated using Eq. C.1.

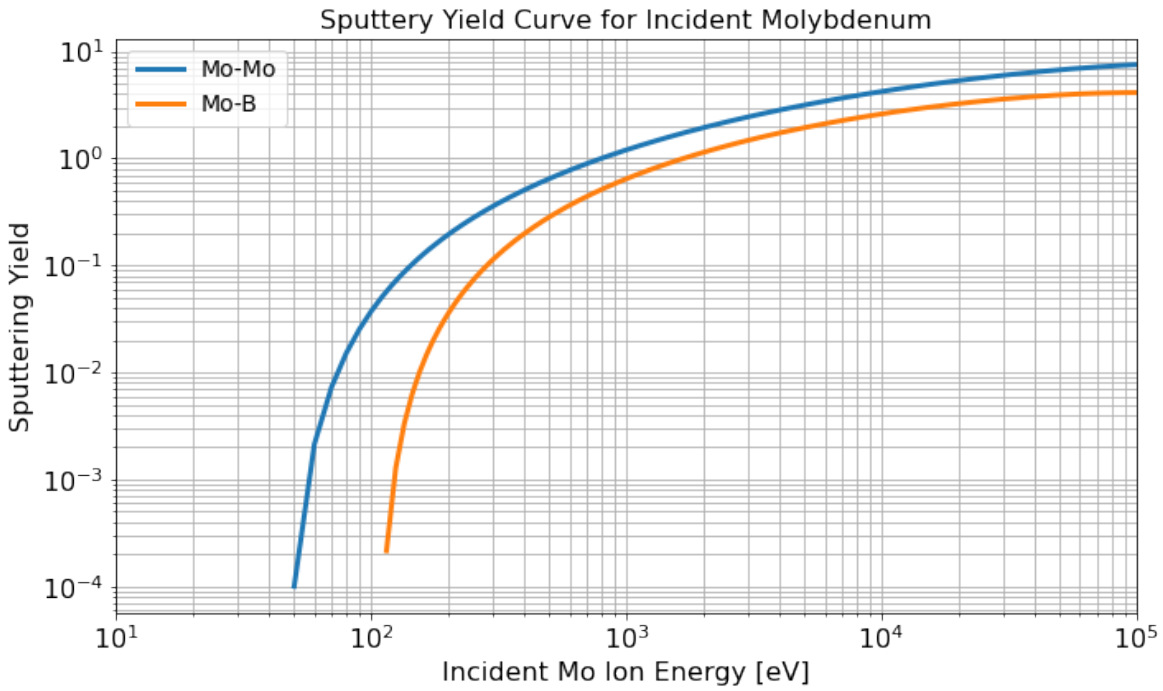

Figure C.5: The resulting sputter yield curve for an incident molybdenum ion impinging on a boron (orange) and a molybdenum (blue) target calculated using Eq. C.1.

References

[1] C. Migliore, M. Stowell, J. C. Wright, and P. T. Bonoli, "Development of impedance sheath boundary condition in Stix finite element RF code," *AIP Conference Proceedings*, vol. 2984, no. 1, p. 060 004, Aug. 2023, ISSN: 0094-243X. DOI: 10.1063/5.0162402. URL: https://doi.org/10.1063/5.0162402.

[2] C. Migliore, J. C. Wright, M. Stowell, and P. T. Bonoli, "Using the Stix finite element RF code to investigate operation optimization of the ICRF antenna on Alcator C-Mod," *Nuclear Fusion*, vol. 63, no. 10, p. 106 006, Aug. 2023, Publisher: IOP Publishing, ISSN: 0029-5515. DOI: 10.1088/1741-4326/acee11. URL: https://dx.doi.org/10.1088/1741-4326/acee11.

[3] IEA, *Electricity Information: Overview*, https://www.iea.org/reports/electricity-information-overview, 2021.

[4] *The Future of Nuclear Energy in a Carbon-Constrained World, An Interdisciplinary MIT Study*, 2018. URL: https://energy.mit.edu/wp-content/uploads/2018/09/The-Future-of-Nuclear-Energy-in-a-Carbon-Constrained-World.pdf.

[5] J. Freidberg, *Plasma Physics and Fusion Energy*. Cambridge University Press, 2007.

[6] Department of Energy, *DOE National Laboratory Makes History by Achieving Fusion Ignition*, Press Release, https://www.energy.gov/articles/doe-national-laboratory-makes-history-achieving-fusion-ignition, Dec. 2022. URL: https://www.energy.gov/articles/doe-national-laboratory-makes-history-achieving-fusion-ignition.

[7] S. Li, H. Jiang, Z. Ren, and C. Xu, "Optimal Tracking for a Divergent-Type Parabolic PDE System in Current Profile Control," *Abstract and Applied Analysis*, vol. 2014, X. Zhang, Ed., p. 940 965, Jun. 2014, Publisher: Hindawi Publishing Corporation, ISSN: 1085-3375. DOI: 10.1155/2014/940965. URL: https://doi.org/10.1155/2014/940965.

[8] J. Wesson, *Tokamaks 3rd Addition*. Oxford University Press, 2004, ISBN: 0 19 8509227.

[9] Z. S. Hartwig, R. F. Vieira, D. Dunn, *et al.*, "The SPARC Toroidal Field Model Coil Program," *IEEE Transactions on Applied Superconductivity*, vol. 34, no. 2, pp. 1–16, Mar. 2024, ISSN: 1558-2515. DOI: 10.1109/TASC.2023.3332613.

[10] C. Hopf, G. Starnella, N. den Harder, and U. Fantz, "Neutral beam injection for fusion reactors: Technological constraints versus functional requirements," *Nuclear Fusion*, vol. 61, no. 10, p. 106 032, Sep. 2021, Publisher: IOP Publishing, ISSN: 0029-5515. DOI: 10.1088/1741-4326/ac227a. URL: https://dx.doi.org/10.1088/1741-4326/ac227a.

[11] P. T. Bonoli, "Review of recent experimental and modeling progress in the lower hybrid range of frequencies at ITER relevant parameters," *Physics of Plasmas*, vol. 21, no. 6, p. 061 508, Jun. 2014, ISSN: 1070-664X. DOI: 10.1063/1.4884360. URL: https://doi.org/10.1063/1.4884360.

[12] S. J. Wukitch, B. Lipschultz, E. Marmar, Y. Lin, A. Parisot, M. Reinke, J. Rice, and J. Terry, "RF plasma edge interactions and their impact on ICRF antenna performance in Alcator C-Mod," *Plasma-Surface Interactions-17*, vol. 363-365, pp. 491–497, Jun. 2007, ISSN: 0022-3115. DOI: 10.1016/j.jnucmat.2007.01.273. URL: https://www.sciencedirect.com/science/article/pii/S0022311507000955.

[13] V. Bobkov, F. Braun, R. Dux, *et al.*, "Assessment of compatibility of ICRF antenna operation with full W wall in ASDEX Upgrade," *Nuclear Fusion*, vol. 50, no. 3, p. 035 004, Feb. 2010, ISSN: 0029-5515. DOI: 10.1088/0029-5515/50/3/035004. URL: https://dx.doi.org/10.1088/0029-5515/50/3/035004.

[14] Y. Yamamura and H. Tawara, "Energy dependece of ion-induced sputtering yields from monatomic solids at normal incidence," *Atomic Data and Nuclear Data Tables*, vol. 62, no. 2, pp. 149–253, Mar. 1996, ISSN: 0092-640X. DOI: 10.1006/adnd.1996.0005. URL: https://www.sciencedirect.com/science/article/pii/S0092640X96900054.

[15] P. Stangeby, *The Plasma Boundary of Magnetic Fusion Devices* (Plasma Physics Series). Institute of Physics Publishing, 2000.

[16] J. R. Myra and D. A. D'Ippolito, "Radio frequency sheaths in an oblique magnetic field," *Physics of Plasmas*, vol. 22, no. 6, p. 062 507, Jun. 2015, ISSN: 1070-664X. DOI: 10.1063/1.4922848. URL: https://doi.org/10.1063/1.4922848.

[17] L. Colas, L. Costanzo, C. Desgranges, S. Brémond, J. Bucalossi, G. Agarici, V. Basiuk, B. Beaumont, A. Bécoulet, and F. Nguyen, "Hot spot phenomena on Tore Supra ICRF antennas investigated by optical diagnostics," *Nuclear Fusion*, vol. 43, no. 1, p. 1, Dec. 2002, ISSN: 0029-5515. DOI: 10.1088/0029-5515/43/1/301. URL: https://dx.doi.org/10.1088/0029-5515/43/1/301.

[18] G. Schilling, S. J. Wukitch, R. L. Boivin, *et al.*, *Analysis of 4-strap ICRF Antenna Performance in Alcator C-Mod*, PPPL Reports, Jul. 2003.

[19] P. Jacquet, F. Marcotte, L. Colas, *et al.*, "Characterisation of local ICRF heat loads on the JET ILW," *Proceedings of the 20th International Conference on Plasma-Surface Interactions in Controlled Fusion Devices*, vol. 438, S379–S383, Jul. 2013, ISSN: 0022-3115. DOI: 10.1016/j.jnucmat.2013.01.075. URL: https://www.sciencedirect.com/science/article/pii/S0022311513000834.

[20] J. R. Myra, "A tutorial on radio frequency sheath physics for magnetically confined fusion devices," *Journal of Plasma Physics*, vol. 87, no. 5, 905 870 504–undefined, 2021, ISSN: 1469-7807. DOI: 10.1017/S0022377821000878. URL: https://www.cambridge.org/core/article/tutorial-on-radio-frequency-sheath-physics-for-magnetically-confined-fusion-devices/37BDBCF6273303327AD6EC2DD4E80533.

[21] V. Bobkov, D. Aguiam, R. Bilato, *et al.*, "Impact of ICRF on the scrape-off layer and on plasma wall interactions: From present experiments to fusion reactor," *Nuclear Materials and Energy*, vol. 18, pp. 131–140, Jan. 2019, ISSN: 2352-1791. DOI: 10.1016/j.nme.2018.11.017. URL: https://www.sciencedirect.com/science/article/pii/S2352179118301091.

[22] M. Bécoulet, L. Colas, S. Pécoul, J. Gunn, Ph. Ghendrih, A. Bécoulet, and S. Heuraux, "Edge plasma density convection during ion cyclotron resonance heating on Tore Supra," *Physics of Plasmas*, vol. 9, no. 6, pp. 2619–2632, May 2002, ISSN: 1070-664X. DOI: 10.1063/1.1472501. URL: https://doi.org/10.1063/1.1472501.

[23] M. J. Martin, W. Gekelman, B. Van Compernolle, P. Pribyl, and T. Carter, "Experimental Observation of Convective Cell Formation due to a Fast Wave Antenna in the Large Plasma Device," *Physical Review Letters*, vol. 119, no. 20, p. 205 002, Nov. 2017, Publisher: American Physical Society. DOI: 10.1103/PhysRevLett.119.205002. URL: https://link.aps.org/doi/10.1103/PhysRevLett.119.205002.

[24] W. Zhang, Y. Feng, J.-M. Noterdaeme, *et al.*, "Modelling of the ICRF induced E×B convection in the scrape-off-layer of ASDEX Upgrade," *Plasma Physics and Controlled Fusion*, vol. 58, no. 9, p. 095 005, Aug. 2016, Publisher: IOP Publishing, ISSN: 0741-3335. DOI: 10.1088/0741-3335/58/9/095005. URL: https://dx.doi.org/10.1088/0741-3335/58/9/095005.

[25] D. A. D'Ippolito, J. R. Myra, E. F. Jaeger, and L. A. Berry, "Far-field sheaths due to fast waves incident on material boundaries," *Physics of Plasmas*, vol. 15, no. 10,

p. 102 501, Oct. 2008, ISSN: 1070-664X. DOI: 10.1063/1.2990025. URL: https://doi.org/10.1063/1.2990025.

[26] F. Perkins, "Radiofrequency sheaths and impurity generation by ICRF antennas," *Nuclear Fusion*, vol. 29, no. 4, p. 583, Apr. 1989, ISSN: 0029-5515. DOI: 10.1088/0029-5515/29/4/004. URL: https://dx.doi.org/10.1088/0029-5515/29/4/004.

[27] M. Bureš, J. Jacquinot, D. Start, and M. Brambilla, "Role of the antenna screen angle during ICRF heating in JET," *Nuclear Fusion*, vol. 30, no. 2, p. 251, Feb. 1990, ISSN: 0029-5515. DOI: 10.1088/0029-5515/30/2/005. URL: https://dx.doi.org/10.1088/0029-5515/30/2/005.

[28] M. Bureš, J.J. Jacquinot, M.F. Stamp, D.D.R. Summers, D.F.H. Start, T. Wade, D.A. D'Ippolito, and J.R. Myra, "Assessment of beryllium Faraday screens on the JET ICRF antennas," *Nuclear Fusion*, vol. 32, no. 7, p. 1139, Jul. 1992, ISSN: 0029-5515. DOI: 10.1088/0029-5515/32/7/I05. URL: https://dx.doi.org/10.1088/0029-5515/32/7/I05.

[29] G. Bal, B.V. Compernolle, P. Pribyl, M.J. Martin, J. Larson, and T.A. Carter, "Reduction in RF sheath rectification with insulating antenna enclosure walls," *Nuclear Fusion*, vol. 62, no. 8, p. 086 043, Jul. 2022, Publisher: IOP Publishing, ISSN: 0029-5515. DOI: 10.1088/1741-4326/ac7814. URL: https://dx.doi.org/10.1088/1741-4326/ac7814.

[30] A. Messiaen and V. Maquet, "Coaxial and surface mode excitation by an ICRF antenna in large machines like DEMO and ITER," *Nuclear Fusion*, vol. 60, no. 7, p. 076 014, Jun. 2020, Publisher: IOP Publishing, ISSN: 0029-5515. DOI: 10.1088/1741-4326/ab8d05. URL: https://dx.doi.org/10.1088/1741-4326/ab8d05.

[31] A. Messiaen, V. Maquet, and J. Ongena, "Ion cyclotron resonance heating fast and slow wave excitation and power deposition in edge plasmas with application to ITER," *Plasma Physics and Controlled Fusion*, vol. 63, no. 4, p. 045 021, Mar. 2021, Publisher: IOP Publishing, ISSN: 0741-3335. DOI: 10.1088/1361-6587/abdf2b. URL: https://dx.doi.org/10.1088/1361-6587/abdf2b.

[32] V. Bobkov, R. Bilato, L. Colas, *et al.*, "Characterization of 3-strap antennas in ASDEX Upgrade," *EPJ Web Conf.*, vol. 157, 2017. DOI: 10.1051/epjconf/201715703005. URL: https://doi.org/10.1051/epjconf/201715703005.

[33] R. Diab, Y. Lin, S.J. Wukitch, A. Kuang, E. Marmar, and J.L. Terry, *Characterization of RF-enhanced potentials with varying antenna power ratio on Alcator C-Mod*, 64th Annual Meeting of the APS Division of Plasma Physics, Spokane, Washington, Oct. 2022.

[34] S.J. Wukitch, Y. Lin, J.L. Terry, *et al.*, *Towards ICRF Anetnnas Compatible with High Performance Plasmas: Characterization and Mitigation of ICRF Antenna–Plasma Edge Interaction*, 22nd Top. Conf. on Radiofrequency Power in Plasmas, Aix en Provence, France, Jun. 2017.

[35] V. Bobkov, F. Braun, R. Dux, *et al.*, "First results with 3-strap ICRF antennas in ASDEX Upgrade," *Nuclear Fusion*, vol. 56, no. 8, p. 084 001, Jul. 2016, Publisher: IOP Publishing, ISSN: 0029-5515. DOI: 10.1088/0029-5515/56/8/084001. URL: https://dx.doi.org/10.1088/0029-5515/56/8/084001.

[36] V. Bobkov, M. Usoltceva, H. Faugel, *et al.*, "Development of pre-conceptual ITER-type ICRF antenna design for DEMO," *Nuclear Fusion*, vol. 61, no. 4, p. 046 039, Mar. 2021, Publisher: IOP Publishing, ISSN: 0029-5515. DOI: 10.1088/1741-4326/abe7d0. URL: https://dx.doi.org/10.1088/1741-4326/abe7d0.

[37] R. J. Perkins, J. C. Hosea, G. J. Kramer, *et al.*, "High-Harmonic Fast-Wave Power Flow along Magnetic Field Lines in the Scrape-Off Layer of NSTX," *Physical Review Letters*, vol. 109, no. 4, p. 045 001, Jul. 2012, Publisher: American Physical Society. DOI: 10.1103/PhysRevLett.109.045001. URL: https://link.aps.org/doi/10.1103/PhysRevLett.109.045001.

[38] R. Ochoukov, D.G. Whyte, D. Brunner, D.A. D'Ippolito, B. LaBombard, B. Lipschultz, J.R. Myra, J.L. Terry, and S.J. Wukitch, "ICRF-enhanced plasma potentials in the SOL of Alcator C-Mod," *Plasma Physics and Controlled Fusion*, vol. 56, no. 015004, 2014.

[39] R. Perkins, J. Hosea, M. Jaworski, R. Bell, N. Bertelli, G. Kramer, L. Roquemore, G. Taylor, and J. Wilson, "The role of rectified currents in far-field RF sheaths and in SOL losses of HHFW power on NSTX," *Proceedings of the 22nd International Conference on Plasma Surface Interactions 2016, 22nd PSI*, vol. 12, pp. 283–288, Aug. 2017, ISSN: 2352-1791. DOI: 10.1016/j.nme.2017.04.013. URL: https://www.sciencedirect.com/science/article/pii/S2352179116302137.

[40] S. Wukitch, B. LaBombard, Y. Lin, B. Lipschultz, E. Marmar, M. Reinke, and D. Whyte, "ICRF specific impurity sources and plasma sheaths in Alcator C-Mod," *Proceedings of the 18th International Conference on Plasma-Surface Interactions in Controlled Fusion Device*, vol. 390-391, pp. 951–954, Jun. 2009, ISSN: 0022-3115. DOI: 10.1016/j.jnucmat.2009.01.245. URL: https://www.sciencedirect.com/science/article/pii/S0022311509002712.

[41] T. Stix, *Waves In Plasmas* (2nd Edition). Springer, New York, 1992.

[42] J. R. Myra, "Physics-based parametrization of the surface impedance for radio frequency sheaths," *Physics of Plasmas*, vol. 24, no. 7, p. 072 507, Jul. 2017, ISSN: 1070-664X. DOI: 10.1063/1.4990373. URL: https://doi.org/10.1063/1.4990373.

[43] *MFEM (available at: Http://mfem.org)*.

[44] C. J. Beers, D. L. Green, C. Lau, J. R. Myra, J. Rapp, T. R. Younkin, and S. J. Zinkle, "RF sheath induced sputtering on Proto-MPEX. I. Sheath equivalent dielectric layer for modeling the RF sheath," *Physics of Plasmas*, vol. 28, no. 9, p. 093 503, Sep. 2021, ISSN: 1070-664X. DOI: 10.1063/5.0054074. URL: https://doi.org/10.1063/5.0054074.

[45] J. Jacquot, D. Milanesio, L. Colas, Y. Corre, M. Goniche, J. Gunn, S. Heuraux, and M. Kubič, "Radio-frequency sheaths physics: Experimental characterization on Tore Supra and related self-consistent modeling," *Physics of Plasmas*, vol. 21, no. 6, p. 061 509, Jun. 2014, ISSN: 1070-664X. DOI: 10.1063/1.4884778. URL: https://doi.org/10.1063/1.4884778.

[46] L. Lu, L. Colas, J. Jacquot, B. Després, S. Heuraux, E. Faudot, D. Van Eester, K. Crombé, A. Krivska, and J.-M. Noterdaeme, "Modelling of radio frequency sheath and fast wave coupling on the realistic ion cyclotron resonant antenna surroundings and the outer wall," *Plasma Physics and Controlled Fusion*, vol. 60, no. 035003, Jan. 2018. DOI: 10.1088/1361-6587/aaa030.

[47] H. Kohno and J. Myra, "A finite element procedure for radio-frequency sheath–plasma interactions based on a sheath impedance model," *Computer Physics Communications*, vol. 220, pp. 129–142, Nov. 2017, ISSN: 0010-4655. DOI: 10.1016/j.cpc.2017.06.025. URL: https://www.sciencedirect.com/science/article/pii/S0010465517302072.

[48] S. Shiraiwa, J. C. Wright, P. T. Bonoli, T. Kolev, and M. Stowell, "RF wave simulation for cold edge plasmas using the MFEM library," *EPJ Web of Conferences*, vol. 157, no. 03048, 2017. DOI: 10.1051/epjconf/201715703048. URL: https://doi.org/10.1051/epjconf/201715703048.

[49] S. Shiraiwa, N. Bertelli, W. Tierens, R. Bilato, J. Hillairet, J. R. Myra, H. Kohno, M. Poulos, and M. Ono, "Magnetic potential based formulation for linear and nonlinear 3D RF sheath simulation," *Nuclear Fusion*, vol. 63, no. 026024, Jan. 2023. DOI: 10.1088/1741-4326/aca6f9.

[50] J. D. Lore, R. Barnett, D. Green, M. Stowell, and M. Kobayashi, "Development of a far-SOL unstructured-mesh fluid-plasma transport solver for RF antenna simulations," *Proceedings of the 28th IAEA Fusion Energy Conference*, Apr. 2021. URL: https://

nucleus.%20iaea.org/sites/fusionportal/Shared%20Documents/%20FEC%202020/fec2020-preprints/preprint0637.pdf.

[51] C. H. Marchi and A. F. C. Silva, "Unidimensional numerical solution error estimation for convergent apparent order," *Numerical Heat Transfer, Part B: Fundamentals*, vol. 42, no. 2, pp. 167–188, Aug. 2002, Publisher: Taylor & Francis, ISSN: 1040-7790. DOI: 10.1080/10407790190053888. URL: https://doi.org/10.1080/10407790190053888.

[52] M. Poulos, "Analysis of nonlinear features associated with radio-frequency sheaths," *Physics of Plasmas*, vol. 29, no. 10, p. 102 104, Oct. 2022, ISSN: 1070-664X. DOI: 10.1063/5.0108481. URL: https://doi.org/10.1063/5.0108481.

[53] H. Kohno and J. R. Myra, "Radio-frequency wave interactions with a plasma sheath in oblique-angle magnetic fields using a sheath impedance model," *Physics of Plasmas*, vol. 26, no. 2, p. 022 507, Feb. 2019, ISSN: 1070-664X. DOI: 10.1063/1.5054920. URL: https://doi.org/10.1063/1.5054920.

[54] H. Kohno, J. R. Myra, and D. A. D'Ippolito, "Numerical analysis of radio-frequency sheath-plasma interactions in the ion cyclotron range of frequencies," *Physics of Plasmas*, vol. 19, no. 1, p. 012 508, Jan. 2012, ISSN: 1070-664X. DOI: 10.1063/1.3677262. URL: https://doi.org/10.1063/1.3677262.

[55] A. Sidi, "Vector extrapolation methods with applications to solution of large systems of equations and to PageRank computations," *Computers & Mathematics with Applications*, vol. 56, no. 1, pp. 1–24, Jul. 2008, ISSN: 0898-1221. DOI: 10.1016/j.camwa.2007.11.027. URL: https://www.sciencedirect.com/science/article/pii/S0898122107008188.

[56] D. A. Smith, W. F. Ford, and A. Sidi, "Extrapolation Methods for Vector Sequences," *SIAM Review*, vol. 29, no. 2, pp. 199–233, 1987. DOI: 10.1137/1029042.

[57] Y. Lin, S. J. Wukitch, P. T. Bonoli, A. Seltzman, and J. C. Wright, "Ion cyclotron range of frequency heating for SPARC," *AIP Conference Proceedings*, vol. 2254, no. 1, p. 030 003, Sep. 2020, ISSN: 0094-243X. DOI: 10.1063/5.0013980. URL: https://doi.org/10.1063/5.0013980.

[58] V. Lancellotti, D. Milanesio, R. Maggiora, G. Vecchi, and V. Kyrytsya, "TOPICA: An accurate and efficient numerical tool for analysis and design of ICRF antennas," *Nuclear Fusion*, vol. 46, no. 7, S476, Jun. 2006, ISSN: 0029-5515. DOI: 10.1088/0029-5515/46/7/S10. URL: https://dx.doi.org/10.1088/0029-5515/46/7/S10.

[59] J. Jacquot, V. Bobkov, L. Colas, S. Heuraux, A. Křivská, L. Lu, J.-M. Noterdaeme, Tore Supra Team, and ASDEX Upgrade Team, "Full wave propagation modelling in view to integrated ICRH wave coupling/RF sheaths modelling," *AIP Conference Proceedings*, vol. 1689, no. 1, p. 050 008, Dec. 2015, ISSN: 0094-243X. DOI: 10.1063/1.4936496. URL: https://doi.org/10.1063/1.4936496.

[60] W. Tierens, D. Milanesio, G. Urbanczyk, W. Helou, V. Bobkov, J.-M. Noterdaeme, L. Colas, R. Maggiora, The ASDEX Upgrade Team, and The EUROfusion MST1 Team, "Validation of the ICRF antenna coupling code RAPLICASOL against TOPICA and experiments," *Nuclear Fusion*, vol. 59, no. 4, p. 046 001, Jan. 2019, Publisher: IOP Publishing, ISSN: 0029-5515. DOI: 10.1088/1741-4326/aaf455. URL: https://dx.doi.org/10.1088/1741-4326/aaf455.

[61] T. Jenkins and D. Smithe, "Time-Domain Modeling of RF Antennas and Plasma-Surface Interactions," *EPJ Web Conf.*, vol. 157, 2017. DOI: 10.1051/epjconf/201715703021. URL: https://doi.org/10.1051/epjconf/201715703021.

[62] A. Kumar, A. Diaw, C. A. Johnson, *et al.*, "Development of an integrated modeling framework for plasma-material interaction and its application on tungsten erosion and transport from the RF antenna structures in the WEST tokamak," 65th Annual Meeting of the APS Division of Plasma Physics, Nov. 2023.

[63] T. Jenkins, D. Smithe, A. Yue, D. Curreli, M. Rezazadeh, M. Brookman, and M. Garrett, "Time-domain modeling of RF sheath potentials for impurity production estimates in SPARC," 65th Annual Meeting of the APS Division of Plasma Physics, Nov. 2023.

[64] B. Lipschultz, Y. Lin, M. L. Reinke, *et al.*, "Operation of Alcator C-Mod with high-Z plasma facing components and implicationsa)," *Physics of Plasmas*, vol. 13, no. 5, p. 056 117, May 2006, ISSN: 1070-664X. DOI: 10.1063/1.2180767. URL: https://doi.org/10.1063/1.2180767.

[65] H. Kohno, J. R. Myra, and D. A. D'Ippolito, "Numerical investigation of fast-wave propagation and radio-frequency sheath interaction with a shaped tokamak wall," *Physics of Plasmas*, vol. 22, no. 7, p. 072 504, Jul. 2015, ISSN: 1070-664X. DOI: 10.1063/1.4926449. URL: https://doi.org/10.1063/1.4926449.

[66] A. Parisot, S. J. Wukitch, P. Bonoli, J. W. Hughes, B. LaBombard, Y. Lin, R. Parker, M. Porkolab, and A. K. Ram, "ICRF loading studies on Alcator C-Mod," *Plasma Physics and Controlled Fusion*, vol. 46, no. 11, p. 1781, Sep. 2004, ISSN: 0741-3335.

DOI: 10.1088/0741-3335/46/11/007. URL: https://dx.doi.org/10.1088/0741-3335/46/11/007.

[67] L. Lao, H. St. John, R. Stambaugh, A. Kellman, and W. Pfeiffer, "Reconstruction of current profile parameters and plasma shapes in tokamaks," *Nuclear Fusion*, vol. 25, no. 11, p. 1611, Nov. 1985, ISSN: 0029-5515. DOI: 10.1088/0029-5515/25/11/007. URL: https://dx.doi.org/10.1088/0029-5515/25/11/007.

[68] V. Bobkov, R. Bilato, F. Calarco, *et al.*, "Multi-strap in-port ICRF antenna modeling and development in support of ITER and EU-DEMO," *AIP Conference Proceedings*, vol. 2984, no. 1, p. 060 010, Aug. 2023, ISSN: 0094-243X. DOI: 10.1063/5.0163035. URL: https://doi.org/10.1063/5.0163035.

[69] D. A. D'Ippolito, J. R. Myra, J. Jacquinot, and M. Bures, "Radio-frequency-sheath-driven edge plasma convection and interaction with the H mode," *Physics of Fluids B: Plasma Physics*, vol. 5, no. 10, pp. 3603–3617, Oct. 1993, ISSN: 0899-8221. DOI: 10.1063/1.860832. URL: https://doi.org/10.1063/1.860832.

[70] V. Bobkov, D. Aguiam, R. Bilato, *et al.*, "Making ICRF power compatible with a high-Z wall in ASDEX Upgrade," *Plasma Physics and Controlled Fusion*, vol. 59, no. 1, p. 014 022, Oct. 2016, Publisher: IOP Publishing, ISSN: 0741-3335. DOI: 10.1088/0741-3335/59/1/014022. URL: https://dx.doi.org/10.1088/0741-3335/59/1/014022.

[71] S. J. Wukitch, M. L. Garrett, R. Ochoukov, *et al.*, "Characterization and performance of a field aligned ion cyclotron range of frequency antenna in Alcator C-Moda)," *Physics of Plasmas*, vol. 20, no. 5, p. 056 117, May 2013, ISSN: 1070-664X. DOI: 10.1063/1.4803882. URL: https://doi.org/10.1063/1.4803882.

[72] R. Diab, S. A. B. Ahmed, Y. Lin, and J. L. Terry, "The role of RF-Induced E×B flows in the mitigation of Scrape-Off-Layer convective transport during Ion Cyclotron Resonance Heating," *Nuclear Fusion*, 2024, ISSN: 0029-5515. URL: http://iopscience.iop.org/article/10.1088/1741-4326/ad26a9.

[73] Y. Li, M. Li, M. Wang, *et al.*, "Experimental investigation on effect of ion cyclotron resonance heating on density fluctuation in SOL at EAST," *Nuclear Engineering and Technology*, vol. 54, no. 1, pp. 207–219, Jan. 2022, ISSN: 1738-5733. DOI: 10.1016/j.net.2021.07.030. URL: https://www.sciencedirect.com/science/article/pii/S1738573321004538.

[74] B. W. Eckstein, J. Bohdansky, and J. Roth, "Physical Sputtering," *Suppl. Nucl. Fusion*, vol. 1, no. 51, 1991.

[75] J. Drobny and D. Curreli, "RustBCA: A High-Performance Binary-Collision-Approximation Code for Ion-Material Interactions," *Journal of Open Source Software*, vol. 6, p. 3298, Aug. 2021. DOI: 10.21105/joss.03298.

[76] J. Drobny and D. Curreli, "Enabling attractive-repulsive potentials in binary-collision-approximation monte-carlo codes for ion-surface interactions," *Materials Research Express*, vol. 10, no. 12, p. 126 513, Dec. 2023, Publisher: IOP Publishing, ISSN: 2053-1591. DOI: 10.1088/2053-1591/ad1262. URL: https://dx.doi.org/10.1088/2053-1591/ad1262.

[77] A. A. Gonzalez Galvan, D. Curreli, C. Migliore, P. Bonoli, and J. Wright, *Numerical simulations of wall impurity emission from the RF limiters of the Alcator C-Mod ICRH antennas using the hPIC2 and RustBCA codes*, 65th Annual Meeting of the APS Division of Plasma Physics, Denver, CO, Oct. 2023.

[78] M.J. May, M. Finkenthal, S.P. Regan, *et al.*, "The measurement of the intrinsic impurities of molybdenum and carbon in the Alcator C-Mod tokamak plasma using low resolution spectroscopy," *Nuclear Fusion*, vol. 37, no. 6, p. 881, Jun. 1997, ISSN: 0029-5515. DOI: 10.1088/0029-5515/37/6/I13. URL: https://dx.doi.org/10.1088/0029-5515/37/6/I13.

[79] P. Rodriguez-Fernandez, A. Creely, M. Greenwald, *et al.*, "Overview of the SPARC physics basis towards the exploration of burning-plasma regimes in high-field, compact tokamaks," *Nuclear Fusion*, vol. 62, no. 4, p. 042 003, Mar. 2022, Publisher: IOP Publishing, ISSN: 0029-5515. DOI: 10.1088/1741-4326/ac1654. URL: https://dx.doi.org/10.1088/1741-4326/ac1654.

[80] P. Rodriguez-Fernandez, N. Howard, and J. Candy, "Nonlinear gyrokinetic predictions of SPARC burning plasma profiles enabled by surrogate modeling," *Nuclear Fusion*, vol. 62, no. 7, p. 076 036, May 2022, Publisher: IOP Publishing, ISSN: 0029-5515. DOI: 10.1088/1741-4326/ac64b2. URL: https://dx.doi.org/10.1088/1741-4326/ac64b2.

[81] D. A. D'Ippolito, J. Myra, R. Ochoukov, and D. Whyte, "Modeling far-field radio-frequency sheaths in Alcator C-Mod," *Plasma Physics and Controlled Fusion*, vol. 55, no. 8, p. 085 001, May 2013, Publisher: IOP Publishing, ISSN: 0741-3335. DOI: 10.1088/0741-3335/55/8/085001. URL: https://dx.doi.org/10.1088/0741-3335/55/8/085001.

[82] N. Smick, B. LaBombard, and C. Pitcher, "Plasma profiles and flows in the high-field side scrape-off layer in Alcator C-Mod," *PSI-16*, vol. 337-339, pp. 281–285, Mar. 2005, ISSN: 0022-3115. DOI: 10.1016/j.jnucmat.2004.09.035. URL: https://www.sciencedirect.com/science/article/pii/S0022311504008979.

[83] A. Q. Kuang, S. Ballinger, D. Brunner, *et al.*, "Divertor heat flux challenge and mitigation in SPARC," *Journal of Plasma Physics*, vol. 86, no. 5, p. 865 860 505, 2020, Edition: 2020/09/29 Publisher: Cambridge University Press, ISSN: 0022-3778. DOI: 10.1017/S0022377820001117. URL: https://www.cambridge.org/core/product/A25A8CFADBBA33AD9AAC18F24E40A18E.

[84] M. Brambilla, "Numerical simulation of ion cyclotron waves in tokamak plasmas," *Plasma Physics and Controlled Fusion*, vol. 41, no. 1, p. 1, Jan. 1999, ISSN: 0741-3335. DOI: 10.1088/0741-3335/41/1/002. URL: https://dx.doi.org/10.1088/0741-3335/41/1/002.

[85] G. Wallace, C. Migliore, J. Wright, M. Brookman, and M. Garrett, "Retiring risk for ion cyclotron range of frequency heating in SPARC through modeling," 65th Annual Meeting of the APS Division of Plasma Physics, Nov. 2023.

[86] M. Porkolab, "Plasma heating by fast magnetosonic waves in Tokamaks," *AIP Conference Proceedings*, vol. 314, no. 1, pp. 99–127, Aug. 1994, ISSN: 0094-243X. DOI: 10.1063/1.46754. URL: https://doi.org/10.1063/1.46754.

[87] E. A. Berro and G. J. Morales, "Excitation of the lower-hybrid resonance at the plasma edge by ICRF couplers," *IEEE Transactions on Plasma Science*, vol. 18, no. 1, pp. 142–148, Feb. 1990, ISSN: 1939-9375. DOI: 10.1109/27.45517.

[88] M. Usoltceva, R. Ochoukov, W. Tierens, A. Kostic, K. Crombé, S. Heuraux, and J.-M. Noterdaeme, "Simulation of the ion cyclotron range of frequencies slow wave and the lower hybrid resonance in 3D in RAPLICASOL," *Plasma Physics and Controlled Fusion*, vol. 61, no. 11, p. 115 011, Oct. 2019, Publisher: IOP Publishing, ISSN: 0741-3335. DOI: 10.1088/1361-6587/ab476d. URL: https://dx.doi.org/10.1088/1361-6587/ab476d.

[89] M. J. Alava and J. A. Heikkinen, "Mode conversion in the vicinity of a fast wave antenna in ICRF-heating," *Plasma Physics and Controlled Fusion*, vol. 34, no. 6, p. 957, Jun. 1992, ISSN: 0741-3335. DOI: 10.1088/0741-3335/34/6/006. URL: https://dx.doi.org/10.1088/0741-3335/34/6/006.

[90] M. Brambilla, "A note on the toroidal plasma dispersion function," *Physics Letters A*, vol. 188, no. 4, pp. 376–383, May 1994, ISSN: 0375-9601. DOI: 10.1016/0375-9601(94)90479-0. URL: https://www.sciencedirect.com/science/article/pii/0375960194904790.

[91] D. Gambier and A. Samain, "Variational theory of ion cyclotron resonance heating in tokamak plasmas," *Nuclear Fusion*, vol. 25, no. 3, p. 283, Mar. 1985, ISSN: 0029-5515. DOI: 10.1088/0029-5515/25/3/005. URL: https://dx.doi.org/10.1088/0029-5515/25/3/005.

[92] L. Meredith, M. Rezazadeh, M. Huq, J. Drobny, V. Srinivasaragavan, O. Sahni, and D. Curreli, "hPIC2: A hardware-accelerated, hybrid particle-in-cell code for dynamic plasma-material interactions," *Computer Physics Communications*, vol. 283, p. 108 569, Feb. 2023, ISSN: 0010-4655. DOI: 10.1016/j.cpc.2022.108569. URL: https://www.sciencedirect.com/science/article/pii/S0010465522002880.

[93] J. R. Myra and H. Kohno, "Validity condition for the local sheath impedance boundary condition and a nonlocal generalization," *AIP Conference Proceedings*, vol. 2984, no. 1, p. 060 002, Aug. 2023, ISSN: 0094-243X. DOI: 10.1063/5.0163291. URL: https://doi.org/10.1063/5.0163291.

[94] H. Childs, E. Brugger, B. Whitlock, *et al.*, "High Performance Visualization–Enabling Extreme-Scale Scientific Insight," 2012. DOI: 10.1201/b12985. URL: https://visit.llnl.gov.

[95] N. Matsunami, Y. Yamamura, Y. Itikawa, N. Itoh, Y. Kazumata, S. Miyagawa, K. Morita, R. Shimizu, and H. Tawara, "Energy dependence of the ion-induced sputtering yields of monatomic solids," *Atomic Data and Nuclear Data Tables*, vol. 31, no. 1, pp. 1–80, Jul. 1984, ISSN: 0092-640X. DOI: 10.1016/0092-640X(84)90016-0. URL: https://www.sciencedirect.com/science/article/pii/0092640X84900160.